

© 2014 A. S. M. Jonayat

TRANSIENT THERMO-FLUID MODEL OF MENISCUS BEHAVIOR AND SLAG
CONSUMPTION IN STEEL CONTINUOUS CASTING

BY

A. S. M. JONAYAT

THESIS

Submitted in partial fulfillment of the requirements
for the degree of Master of Science in Mechanical Engineering
in the Graduate College of the
University of Illinois at Urbana-Champaign, 2014

Urbana, Illinois

Adviser:

Professor Brian G. Thomas

ABSTRACT

The behavior of the slag layer between the oscillating mold wall, the slag rim, the slag/liquid steel interface, and the solidifying steel shell, are of immense importance for the surface quality of continuous-cast steel. A computational model of the meniscus region has been developed, that includes transient heat transfer, multi-phase fluid flow, solidification of the slag, and movement of the mold during an oscillation cycle. First, the model is applied to a lab experiment done with a “mold simulator” to verify the transient temperature-field predictions. Next, the model is verified by matching with available literature and plant measurements of slag consumption. A reasonable agreement has been observed for both temperature and flow-field. The predictions show that transient temperature behavior depends on the location of the thermocouple during the oscillation relative to the meniscus. Finally, the model is applied to conduct a parametric study on the effect of casting speed, stroke, frequency, and modification ratio on slag consumption. Slag consumption per unit strand area increase with increase of stroke and modification ratio, and decreases with increase of casting speed while the relation with frequency is not straightforward. The match between model predictions and literature trends suggests that this methodology can be used for further investigations.

ACKNOWLEDGEMENT

My sincere gratitude to my adviser, Professor Brain G. Thomas, for his continuous support, expertise, guidance and encouragement during this work. I would like to acknowledge the work of previous student Robert McDavid and visiting scholar Claudio Ojeda for early works on this topic. The financial support for this project is provided by the members of Continuous Casting Consortium at University of Illinois at Urbana-Champaign (UIUC), for which I am ever grateful. My gratitude to Professor Surya Pratap Vanka for introducing me to the vast array of numerical methods and algorithms in Computational Fluid Dynamics.

I would also like to thank my colleagues at Metals Processing Simulation Laboratory Kai Jin, Lance Hibbeler, Seong-Mook Cho, Bryan Petrus and Rui Liu for their suggestions and insights which have helped me in many occasions. I thank all of my lab mates – Younghui Li, Kun Xu, Ramnik Singh, Mathew Zappulla, Aravind Murli, Prathiba Duvvuri and Hyunjin Yang for making my time in this lab memorable. Finally, I thank my family for the continuing support in my endeavor for higher studies.

TABLE OF CONTENTS

LIST OF FIGURES	vii
LIST OF TABLES	x
LIST OF SYMBOLS	xi
CHAPTER 1: INTRODUCTION	1
1.1 Continuous Casting Process of Steel:	1
1.2 Functions of slag and its consumption:	2
1.3 Scope of this work:	3
1.4 Figures:	4
CHAPTER 2: LITERATURE REVIEW	5
CHAPTER 3: COMPUTATIONAL MODEL DEVELOPMENT	10
3.1 Governing Equations:	10
3.2 Model Domains:	13
3.3 Boundary Conditions:	14
3.4 Powder and Slag Properties:	17
3.4.1 Slag Viscosity:	19
3.4.2 Slag Thermal Conductivity:	20

3.4.3 Slag Specific Heat and Density:	21
3.5 Other Material Properties:	21
3.6 Solution Procedure:	22
3.7 Figures:	25
3.8 Tables:	30
CHAPTER 4: VALIDATION CASES	33
4.1 Commercial Caster (Shin) Case:	33
4.2 Experimental Simulator (Badri) Case:	34
4.3 Flow Field Results:	34
4.4 Slag Consumption Results:	36
4.5 Temperature Results:	37
4.6 Phase Lag Results:	39
4.7 Heat Flux Results:	40
4.8 Figures:	47
CHAPTER 5: PARAMETRIC STUDIES	70
5.1 Simplified Model Development:	70
5.2 Simplified Model Validation:	71

5.3 Casting Conditions for Parametric Studies:	71
5.4 Results:	72
5.4.1 Casting Speed (v_c):	72
5.4.2 Stroke (s):	72
5.4.3 Frequency (f):	72
5.4.4 Modification Ratio (α_m):	73
5.4.5 Positive Strip Time (PST, t_p):	73
5.4.6 Negative Strip Time (NST, t_n):	74
5.5 Figures:	75
5.6 Tables:	80
CHAPTER 6: CONCLUSIONS	82
REFERENCES	84
APPENDIX A	97
APPENDIX B	99
APPENDIX C	114

LIST OF FIGURES

Figure 1.1: (a) Transient phenomena in a caster (b) Meniscus region.....	4
Figure 3.1: Schematic of model domain and boundaries (not drawn to scale).....	25
Figure 3.2: Temperature dependent slag viscosity predicted by Riboud model for different %Al ₂ O ₃ pickup Vs. measured values	26
Figure 3.3: Temperature dependent viscosity model during solidification and melting	27
Figure 3.4: Temperature dependent thermal conductivity model for slag melting and solidifying.....	28
Figure 3.5: Temperature dependent specific heat of slag	29
Figure 4.1: Badri experiment thermocouple locations (left) and mold dimensions (right)	47
Figure 4.2: Displacement, Velocity and NST time over one oscillation cycle (0.77-1.12 s) for Shin case.....	48
Figure 4.3: Meniscus region events over one oscillation cycle (0.77-1.12 s) for Shin Case.....	49
Figure 4.4: Predicted slag pressure at 0.4 mm from hot face and 0.5 mm above shell tip (Shin case: 0.77-1.12 s).....	50
Figure 4.5: Predicted instantaneous and mean slag consumption for Shin case (0.77-1.12 s).....	51
Figure 4.6: Liquid slag thickness predicted by model based on 1101°C and 800°C constant temperature line (Shin Case: 0.77-1.12 s).....	52

Figure 4.7: Transient velocity in the slag gap (Shin Case: 0.77-1.12 s).....	53
Figure 4.8: Temperature predictions at TC (hot) locations over simulation time (Badri case: fixed in lab frame of reference).....	54
Figure 4.9: Measured temperatures in Trial 32 reported by Badri ^[97]	55
Figure 4.10: Model averaged thermocouple predictions Vs. measured values by Badri averaged over six oscillation cycles (error bars indicate the range)	56
Figure 4.11: Thermocouple prediction by model Vs. measured temperatures by Badri (Thermocouples fixed in mold)	57
Figure 4.12: Displacement, Velocity and NST time over one oscillation cycle for Badri experiment.....	58
Figure 4.13: Badri ^[97] thermocouple measurements for Trial 31	59
Figure 4.14: Comparison between temperature and heat flux predictions at TC3 (hot) location for reference frames fixed in the lab (Eulerian) and mold (Lagrangian) (Badri case)	60
Figure 4.15: Temperature and heat flux predictions at TC3-TC5 (hot) locations using lab reference frame (Badri case).....	61
Figure 4.16: Temperature and heat flux predictions at TC2-TC6 (hot) locations using lab reference frame (Shin case: 0.77-1.12 s)	62

Figure 4.17: Temperature and heat flux predictions at TC3-TC6 (hot) locations using mold reference frame (Badri case).....	63
Figure 4.18: Temperature and heat flux predictions at TC2-TC6 (hot) location using mold reference frame (Shin case: 0.77-1.12 s)	64
Figure 4.19: Temperature and heat flux predictions at TC3-4 (hot) locations using mold reference frame (Shin case: 0.43-0.77 s)	65
Figure 4.20: Overflow event in Shin Case (0.59 s).....	66
Figure 4.21: Heat flux predictions at the region 45 mm below meniscus (Badri case).....	67
Figure 4.22: Predicted transient heat flux profile over an oscillation cycle (Badri case).....	68
Figure 4.23: Predicted transient heat flux profile over an oscillation cycle (Shin case: 0.43-0.77 s).....	69
Figure 5.1: Predicated transient slag consumption for slag consumption validation cases	75
Figure 5.2: Predicted effect of changing casting speed, stroke and modification ratio on slag consumption	76
Figure 5.3: Predicted effect of changing frequency on slag consumption.....	77
Figure 5.4: Predicted and measured ^[76] slag consumption Vs. Positive Strip Time.....	78
Figure 5.5: Predicted and measured ^[76] slag consumption Vs. Negative Strip Time	79

LIST OF TABLES

Table 3.1: Variables used in model.....	30
Table 3.2: Mold slag composition	31
Table 3.3: Properties of liquid steel and Cu (mold).....	32
Table 5.1: Casting conditions, measured and predicted slag consumption for validation cases ...	80
Table 5.2: Casting conditions, measured and predicted slag consumption for parametric study cases	81

LIST OF SYMBOLS

a	Amplitude of mold oscillation
c_p	Specific heat
d_{ch}	Mold water channel depth
d_{eff}	Effective mold thickness
f	Frequency of mold oscillation
F_1	Blending function in k - ω SST model
F_σ	Surface tension force at the steel / slag interface
g	Gravity
h_c	Effective heat transfer coefficient from mold cold face
h_{mix}	Enthalpy of mixture
K	Thermal conductivity
K_{eff}	Effective thermal conductivity
K_{mix}	Mixture thermal conductivity
K_t	Turbulent thermal conductivity
k	Turbulent energy
k_c	Constant used in Shin's empirical equation for slag consumption
k_β	Constant used in Tsutsumi's empirical equation for slag consumption
l_{ch}	Mold water channel spacing
M_i	Molecular weight of i^{th} compound

n	Empirically chosen exponent to fit measured data for power-law for slag viscosity
$\hat{\mathbf{n}}$	Unit normal of the surface
$\hat{\mathbf{n}}_t$	Unit normal to interface at three-phase contact point
$\hat{\mathbf{n}}_{wall}$	Unit normal to wall at three-phase contact line point
p	Pressure
p_i	Constant pressure at inlet of model (slag top surface)
p_o	Constant pressure at outlet of model (slag outlet)
q_s	Surface heat flux
Q_{area}	Slag consumption per unit strand area
\mathbf{S}	Strain rate tensor
s	Stroke of mold oscillation
T	Temperature
T_a	Constant Temperature at the slag top surface
T_w	Average water temperature in water channels used in model
T_{Br}	Break temperature of slag
T_b	Backflow temperature in model
T_{cs}	Crystallization temperature of slag
T_{fsol}	Empirically chosen temperature to fit measured data for power-law for slag viscosity
T_g	Glass transition temperature of slag

T_o	Reference temperature of power-law for slag viscosity
T_s	Mold cold face temperature
T_{sc}	Cold shell surface temperature in model
T_{sh}	Temperature of liquid steel
T_{ref}	Arbitrary reference temperature for enthalpy calculation
t_p	Positive strip time
t_n	Negative strip time
t	Time
\mathbf{v}	Velocity vector
v_m	Mold velocity
v_c	Casting speed
w_{ch}	Mold water channel width
X_l	wt% of components in final molten slag
X_{lo}	wt% of components in molten slag
X_p	wt% of components in powder during casting
X_{rep}	wt% of components in slag reported by supplies
X_i	Molar fraction of i^{th} compound
x	Horizontal direction (from mold)
y	Vertical direction
z	Undiscretized horizontal direction (around perimeter)
x_{sol}	Width of solidification region in model
α_m	Modification ratio of mold oscillation

α_{Fe}	Volume fraction of steel
α_{sl}	Volume fraction of slag
α_T	Thermal diffusivity
β, β^*, γ	Constants in $k-\omega$ SST model
$\gamma_{Fe(l)-sl}$	Surface tension between liquid steel ($Fe(l)$) and slag (sl)
$\gamma_{Fe(l)-gas}$	Surface tension between liquid steel ($Fe(l)$) and inert gas (gas)
γ_{sl-gas}	Surface tension between slag (sl) and inert gas (gas)
ΔH	Enthalpy of transition of slag
θ_{eq}	Static Contact angle at rest/equilibrium between phases
θ_d	Dynamic contact angle between phases
κ	Local curvature of steel/slag interface
μ	Dynamic viscosity
μ_{mix}	Mixture dynamic viscosity
μ_o	Reference viscosity of power-law for slag viscosity
μ_t	Turbulent dynamic viscosity
ν	Kinematic viscosity
ν_t	Turbulent kinematic viscosity
ρ_{Fe}	Density of Steel
ρ_{mix}	Density of mixture
ρ_{sl}	Density of slag

σ_{sl-Fe}	Constant surface tension at interface between steel / slag
σ_k, σ_ω	Constants in $k-\omega$ SST model
Φ	Constant for taking into account the attraction between the phases for CaO-Al ₂ O ₃ -SiO ₂ system
ω	Specific dissipation rate

CHAPTER 1: INTRODUCTION

In continuous casting of steel, initial solidification in the mold near the meniscus is very important to ultimate quality of the steel. Defects^[1-2] arising near the meniscus remain at the surface of the eventual steel products, and are expensive or impossible to remove. To prevent oxidation of the molten steel by exposure to air, a layer of mold powder is maintained on the top surface by periodic additions of this carefully selected, proportioned, and mixed combination of metal oxide powders and graphite. This powder provides lubrication, maintains uniform heat transfer between the mold and steel shell, and removes inclusions that rise up from the molten steel.^[3]

1.1 Continuous Casting Process of Steel:

Figure 1.1(a) shows a schematic of the continuous casting process. Liquid steel flows from the tundish (not shown in figure) into the mold, through the submerged entry nozzle's (SEN) bifurcated ports that direct the flow of the molten liquid jets towards the narrow face mold walls and eventually upwards to the meniscus region at the top surface around the mold perimeter. Cooling water flows through the channels of the mold, and extracts heat, causing the superheated liquid steel to solidify against the mold walls as a shell or steel strand, which is pulled downward at the casting speed. To prevent sticking, the mold oscillates with a given frequency, stroke ($2 \times \text{Amplitude}$) and sometimes a modification ratio for non-sinusoidal oscillation.^[4] During the casting process, the mold powder gets heated, sinters, and melts to form a molten slag layer that floats on top of the molten steel.^[5] The shape of the interface between the slag and steel curves in the meniscus region, according to the surface tension, buoyancy, and momentum forces, and changes with time according to the mold oscillation and turbulent flow.^[6-7] The liquid slag is eventually consumed into the thin gap between the mold and the solidifying steel shell by the

downward movement of the strand. The amount of slag that has to be added to the mold surface over time is termed as slag consumption.

Figure 1.1(b) shows a close-up schematic of the phenomena near the meniscus at the mold hot face, where the molten slag transforms to solid slag as it cools due to heat removal into the water-cooled mold. As a result, the gap between the mold hot face and the steel shell contains slag in two phases – solid and liquid. A thicker layer of solid slag termed the “Slag Rim” solidifies against the mold hot face above the liquid slag layer.^[8] The slag rim sticks to the mold and oscillates with it. In addition to affecting the heat flux, the oscillating slag rim periodically pushes on the liquid or partially solidified meniscus^[9] which may form depressions on the steel shell surface called “Oscillation Marks (OM)”.^[3, 10] Downward movement of the OMs also consumes slag. The slag viscosity and other properties change greatly with temperature.^[11] Furthermore, the melting powder has different properties than the cooling liquid slag, even at the same temperature.^[12]

1.2 Functions of slag and its consumption:

The slag must fulfill many important functions, in addition to preventing air oxidation. If the slag layer in the gap is not thick enough, the steel shell may come into direct contact with the mold wall, which may cause sticking of the steel eventually leading to a catastrophic breakout,^[13] where molten steel escapes from a rupture in the shell below mold exit. If the inclusions that rise up are unable to be captured into the liquid slag layer, then many inclusions will end up in the final product. If heat flux variations near the meniscus are too severe, due to slag layer thickness variations, then cracks may form.^[14-16] Finally, if fluctuations of the liquid steel / slag interface are too severe, then liquid slag may become entrained into the solid or molten steel, leading to surface or internal defects respectively.^[17-18]

Slag consumption is affected by many casting parameters – casting speed, oscillation frequency, stroke and mode of oscillation (sinusoidal/non-sinusoidal).^[19] The material properties also affect slag consumption. To optimize slag behavior in the casting process, it is important to understand how these parameters affect meniscus behavior and slag consumption both qualitatively and quantitatively.

1.3 Scope of this work:

This paper presents a computational model of transient thermo-fluid flow of slag and steel in the meniscus region that can simulate the transient temperature distribution, fluid flow velocities, movement of the interface between the phases, formation of the solid and liquid slag layers, and slag consumption. The model is validated by experimental measurements of a caster simulator and applied in a parametric study of the effect of changing casting parameters on slag consumption.

1.4 Figures:

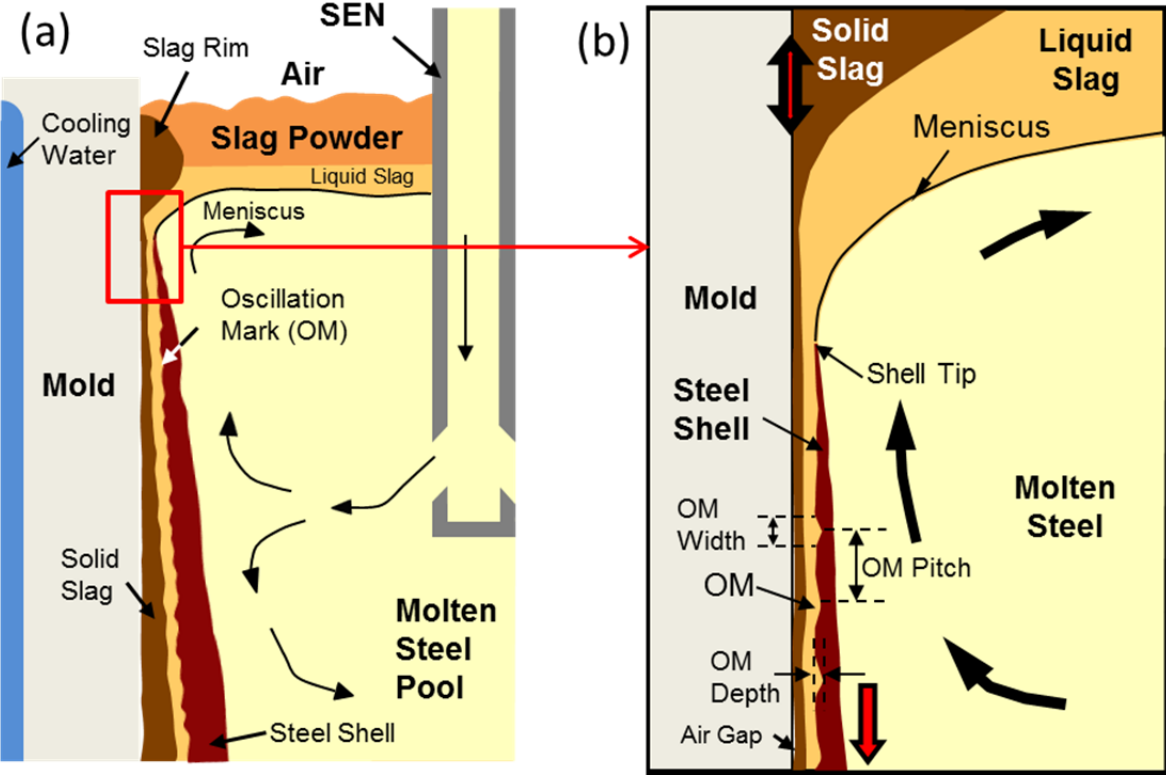


Figure 1.1: (a) Transient phenomena in a caster (b) Meniscus region.

CHAPTER 2: LITERATURE REVIEW

To gain insight into the slag layers and phenomena in the meniscus region, computational models have evolved over many years. Early modelers^[5, 20-21] including Nakano et al.^[5] analyzed slag melting as one-dimensional (1D) heat transfer in the slag layers above the molten steel. Thermal properties were varied with slag form (powdered, sintered or molten) according to a packing factor, that was related to the sintering rate with a modified Jander's^[22] equation. This model matched steady-state temperature measurements in the powder and the measured slag thickness, but, the liquid conductivity had to be increased 4 times (without oscillation) or 6 times (with oscillation) to account for the un-modeled convection in the liquid slag. This work shows the importance of temperature-dependent properties, mold oscillation, and convection effects on the slag heat transfer.

Many numerical and semi-analytical models have focused on fluid flow and heat transfer in the gap between the steel shell and mold wall.^[10, 23-28] Many of these assume constant slag viscosity.^[23-26] Anzai et al.^[23] modeled isothermal slag flow in the mold-strand gap as drag flow between two fixed non-parallel surfaces and found pressure increased with increasing slag viscosity, which matched measurements. This model predicts that slag consumption increases when the mold moves downward during each oscillation cycle and reverses when the mold moves upward. A similar model by Takeuchi et al.^[10] included temperature dependent viscosity and found the same relation.

Several analytical models coupled lubrication theory with heat conduction to model solid, liquid slag layer thickness, and heat flux.^[29-31] Bland et al.^[29] had temperature-dependent slag viscosity of the form $\mu(T) = A_1 e^{-A_2 T}$ where μ , T are viscosity and temperature respectively and A_1 , A_2 are

constants. The predicted slag consumption was in the lower end of plant observations. Bland's model was improved by Fowkes et al.^[30] by dividing the slag layer above and below the tip of the solidifying steel shell. Fowkes explained slag flow with a pumping mechanism with slag consumption occurring during the "negative strip time, when the downward velocity of the mold wall exceeds the casting speed. Hill et al.^[31] improved the Fowkes predicted solid and liquid slag thickness, oscillation mark shape and concluded that oscillation mark depth is depends on slag viscosity, casting speed and oscillation stroke. The predicted oscillation mark thickness in this study was similar to plant measurements^[32-33] but slag consumption was not predicted. Steinruck et al.^[34] modeled oscillation mark formation by modeling slag flow, heat transfer and solidification of strand shell simultaneously. His model predicted that slag consumption (kg/m^2) decreases with casting speed with fixed stroke and matched experimental values reasonably well. However, he found the relation with consumption and oscillation frequency and stroke to be non-monotonic, but these predictions were not validated quantitatively.

Meng et al.^[35] coupled a gap lubrication model of the interfacial gap with a 1D transient model of the solidifying steel shell and a 2-D steady-state model of heat conduction in the mold. This software, named "CON1D," can accurately predict shell thickness, liquid / solid slag-layer thickness, slag, shell, and mold temperatures, heat flux, and other casting variables when calibrated correctly with plant measurements. Based on the input total slag consumption, the slag velocity model includes solid slag, liquid slag and slag dragged downward in OMs. Heat transfer across the interfacial gap is modeled as radiation and conduction including the effects of air-gap formation, contact resistance, and liquid slag viscosity with temperature-dependent exponential function. This model has been used by many researchers for process analysis,^[36-39] problem solving,^[1, 40-41] and control^[42] of continuous casting, while others^[39, 43] have input CON1D results

as initial conditions into advanced models to save computation. Details of CON1D are available elsewhere.^[41, 44-45]

Many researchers have measured slag consumption,^[19, 46-50] OM depth,^[10, 19, 50] and hook depth,^[51-52] as related to casting conditions and slag viscosity. Extensive plant measurements on a conventional slab caster at POSCO by Shin et al.^[19] related slag consumption, OM and hook depth to casting speed, oscillation frequency and slag properties such as surface tension, density and viscosity. Total slag consumption was divided into three components – solid and liquid layer (lubrication) and OM consumption similar to CON1D formulation and with an empirical model to predict each part. The empirical equation, matches well with plant measurements, but requires a fitting constant to include the important effect of powder properties. It also matches the trends of casting condition effects on slag consumption of other studies.^[47, 50, 53] This model of steady-state slag consumption is a useful tool to validate computational models. The measured trends are discussed in further detail later.

McDavid et al.^[54] developed a 3D coupled heat-transfer and fluid-flow finite element model to analyze the top surface slag layers. This model used different temperature-dependent viscosity, thermal conductivity and specific heat functions for regions of melting powder or solidifying liquid slag. The slag/steel interface shape and slag consumption were fixed to match plant measurements, and shear stress distribution along the interface was applied from a separate 3D model of molten steel flow. The predicted slag layer thickness profiles matched with plant measurements, and revealed a large flow recirculation in the liquid slag. Zhao et al.^[55] confirmed this single long thin recirculation for most conditions, and also showed that many small natural convection cells can form, but only for very small steel surface velocities. Modeled steel and slag

velocities diminish towards the meniscus around the mold perimeter, as flow of slag is due to consumption.^[56-57]

Ojeda et al.^[58-59] worked on a transient thermal – flow model of the meniscus region during an oscillation cycle, including the top slag layer, the slag rim, slag / steel interface, and the gap between the mold wall and the top ~70 mm of the steel shell. Temperature-dependent slag properties were used following McDavid et al.^[54] The predicted flow behavior in the meniscus region during an oscillation cycle agreed well with works by Sengupta et al.^[60] and the predicted slag consumption matched with plant measurements.^[23] However, the fixed gap size needed by the model was not explained, and it has not been applied in parametric studies.

Recently, a complex model by Lopez et al.,^[61-62] couples together heat transfer and flow in the molten steel and slag layers, mold wall, and solidifying steel shell. This 2-D model of half of a caster extends ~1.5m from top of the non-moving mold. Utilizing a very fine adaptive mesh, this model uses the VOF method^[63] to track the slag / steel interface and the enthalpy-porosity technique^[64] to model the steel solidification. The slag viscosity is temperature dependent, but the conductivity is constant, and the slag / mold interface oscillates. The predicted transient flow field agreed qualitatively with Ojeda et al.,^[59] the heat flux behavior agreed qualitatively with Badri et al.^[65-66] at 45 mm below the meniscus, and the trend of decreasing slag consumption with increasing casting speed agreed with Shin et al.^[67] The flow rate of slag powder into the top of the domain was a fixed boundary condition, but the effect of this input condition on the ability of the model to predict slag consumption was not reported. Finally, the reported simulation time of 120 hrs per case on a dual-core pc may limit its use for extensive parametric study.

Previous work has shed light on methods to model thermo-fluid behavior in the meniscus region and slag consumption. No model yet can accurately predict slag consumption for arbitrary plant conditions. The current work presents an efficient model of transient thermal-flow in the meniscus region during oscillation that is validated with both lab and plant measurements, and is applied in a parametric study to predict slag consumption.

CHAPTER 3: COMPUTATIONAL MODEL DEVELOPMENT

3.1 Governing Equations:

A two-dimensional two-phase (slag and steel) thermo-fluid model has been developed to predict transient fluid-flow and temperature in the region near the mold hot face and meniscus of a continuous slab caster, including the oscillating solid mold. A single set of momentum, continuity and energy equations are solved on a fixed grid using the volume-of-fluid method^[63] (VOF) to determine the slag and steel phase regions in the fluid domain.

The two incompressible fluid phases are identified by a single phase fraction marker function, represented by the volume fraction of steel, α_{Fe} , which is advected by the flow according to the following conservation equation,

$$\frac{\partial \alpha_{Fe}}{\partial t} + \mathbf{v} \cdot \nabla \alpha_{Fe} = 0 \quad (3.1)$$

where \mathbf{v} is the vector of velocity components. The volume fraction of slag (α_{sl}) is calculated from total mass conservation:

$$\alpha_{Fe} + \alpha_{sl} = 1 \quad (3.2)$$

Material properties in each point in the domain are represented using mixture equations of α_{sl} and α_{Fe} , such as Eqn. 3.3 for density of the fluid (ρ_{mix}).

$$\rho_{mix} = \alpha_{Fe} \rho_{Fe} + (1 - \alpha_{Fe}) \rho_{sl} \quad (3.3)$$

where (ρ_{sl}) and (ρ_{Fe}) are constant densities of slag and steel. Continuity is satisfied by the following equation:

$$\frac{\partial \rho_{mix}}{\partial t} + \nabla \cdot (\rho_{mix} \mathbf{v}) = 0 \quad (3.4)$$

For momentum conservation, a single set of Navier-Stokes equations given by Eqn. 3.5 is solved.

$$\rho_{mix} \frac{\partial \mathbf{v}}{\partial t} + \rho_{mix} \mathbf{v} \cdot \nabla \mathbf{v} = -\nabla p + \nabla \cdot \left[\mu_{mix} (\nabla \mathbf{v} + \nabla^T \mathbf{v}) \right] + \rho_{mix} \mathbf{g} + \mathbf{F}_\sigma \quad (3.5)$$

where \mathbf{F}_σ is the force source term due to surface tension given by the following equation, which is modeled using the CSF model of Brackbill et al.^[68]

$$\mathbf{F}_\sigma = \sigma_{sl-Fe} \frac{\rho_{mix} \kappa \nabla \alpha_{sl}}{\frac{1}{2}(\rho_{sl} + \rho_{Fe})} \quad (3.6)$$

Here, σ_{sl-Fe} is the constant surface tension of the interface between the slag and steel (N/m), and κ is the local curvature of this interface, found from -

$$\kappa = \nabla \cdot \hat{\mathbf{n}} \quad (3.7)$$

where $\hat{\mathbf{n}}$ is the unit normal ($\hat{\mathbf{n}} = \mathbf{n} / |\mathbf{n}|$) of the surface, found from the phase fraction marker field, $\mathbf{n} = \nabla \alpha_{sl}$. At the wall boundary, $\hat{\mathbf{n}}$ is found from -

$$\hat{\mathbf{n}} = \hat{\mathbf{n}}_{wall} \cos \theta_{eq} + \hat{\mathbf{n}}_t \sin \theta_{eq} \quad (3.8)$$

where $\hat{\mathbf{n}}_t$ is normal to the interface where it contacts the wall and $\hat{\mathbf{n}}_{wall}$ is normal to the wall. The angle, θ_{eq} , is the static contact angle when the fluid is at rest. The angle may change (dynamic contact angle, θ_d) with interface motion. Without measurements to establish a constitutive law for θ_d , θ_{eq} is used in practice.^[69]

Temperature in both the fluid (slag-steel) and solid (mold) regions of the domain is found by first solving the following enthalpy formulation of the energy equation.

$$\frac{\partial}{\partial t}(\rho_{mix}h_{mix}) + \nabla \cdot (\rho_{mix} \mathbf{v}h_{mix}) = \nabla \cdot (K_{eff} \nabla T) \quad (3.9)$$

where temperature T is found from the enthalpy of the mixture, h_{mix} , via

$$h_{mix} = \int_{T_{ref}}^T (c_p)_{mix} dT \quad (3.10)$$

where C_p is specific heat, and T_{ref} is an arbitrary reference temperature. For the VOF model, h_{mix} is a mass average weighted over the phase fractions of the slag and steel,

$$h_{mix} = \frac{(\alpha\rho h)_{sl} + (\alpha\rho h)_{Fe}}{(\alpha\rho)_{sl} + (\alpha\rho)_{Fe}} \quad (3.11)$$

Thermal conductivity of the fluid, K_{eff} is the sum of the mixture conductivity (K_{mix}) and the conductivity due to turbulence (K_t). For turbulence closure, Menter's^[70-71] $k-\omega$ SST model is used. Following the $k-\omega$ SST formulation, two more transport equations are solved for turbulent energy (k) and specific dissipation rate (ω),

$$\begin{aligned} \frac{\partial}{\partial t}(\rho_{mix}k) + \nabla \cdot (\rho_{mix}k\mathbf{v}) &= \nabla \cdot [(\mu_{mix} + \sigma_k\mu_t)\nabla k] - \beta^* \rho_{mix} \omega k + \tilde{P}_k \\ \frac{\partial}{\partial t}(\rho_{mix}\omega) + \nabla \cdot (\rho_{mix}\omega\mathbf{v}) &= \nabla \cdot [(\mu_{mix} + \sigma_\omega\mu_t)\nabla \omega] - \beta\rho_{mix}\omega^2 + \frac{\gamma}{\nu_t} \tilde{P}_k \\ &+ 2(1-F_1)\rho_{mix}\sigma_{\omega 2} \frac{1}{\omega} \frac{\partial k}{\partial x_j} \frac{\partial \omega}{\partial x_j} \end{aligned} \quad (3.12)$$

Where the production term, \tilde{P}_k , is

$$\tilde{P}_k = \min \left[\mu_t \frac{\partial v_i}{\partial x_j} \left(\frac{\partial v_i}{\partial x_j} + \frac{\partial v_j}{\partial x_i} \right); 10\beta^* \rho k \omega \right] \quad (3.13)$$

The other terms are given by -

$$F_1 = \tanh \left(\left[\min \left\{ \max \left(\frac{\sqrt{k}}{0.09\omega y}; \frac{500\nu}{y^2\omega} \right), \frac{4\rho_{mix}\sigma_{\omega 2}k}{CD_{k\omega}y^2} \right\} \right]^4 \right) \quad (3.14)$$

where,

$$CD_{k\omega} = \max \left(2\rho_{mix}\sigma_{\omega 2} \frac{1}{\omega} \frac{\partial k}{\partial x_j} \frac{\partial \omega}{\partial x_j}, 10^{-10} \right) \quad (3.15)$$

and

$$v_t = \frac{\mu_t}{\rho_{mix}} = \frac{a_1 k}{\max(a_1\omega; |\mathbf{S}|F_2)}; F_2 = \tanh \left(\left\{ \max \left(2 \frac{\sqrt{k}}{0.09\omega y}; \frac{500\nu}{y^2\omega} \right) \right\}^2 \right) \quad (3.16)$$

Here y is the distance to the closest wall node, \mathbf{S} is strain rate tensor and the constants ϕ ($\beta^*, \beta, \sigma_k, \sigma_\omega, \gamma$) are calculated based on Eqn. 3.17.

$$\phi = F_1\phi_1 + (1-F_1)\phi_2 \quad (3.17)$$

The constants are $-\sigma_{k1} = 0.85$, $\sigma_{k2} = 1.0$, $\sigma_{\omega 1} = 0.5$, $\sigma_{\omega 2} = 0.856$, $\beta_1 = 0.075$, $\beta_2 = 0.0828$
 $a_1 = 0.31$, $\beta^* = 0.09$, $\gamma_1 = \frac{5}{9}$, and $\gamma_2 = 0.44$.

F_1 is the blending function and $F_1 = 1$ in the near-wall region (activates $k-\omega$) and $F_1 = 0$ in the outer region (activates $k-\epsilon$).

3.2 Model Domains:

Figure 3.1 shows the two domains of this model: the fluid and the mold. The fluid domain contains powder, molten slag and molten steel in the meniscus region extending 100 mm (width) from the mold wall and a length from 100 mm below to 50 mm above the tip of the solidifying steel shell (length). Flow in this small region is relatively unaffected by molten steel flow^[54] and is mainly dominated by mold oscillation. The fluid domain also includes part of the interfacial gap between the steel shell and the mold wall, but it does not include the solidifying steel shell.

The thickness profiles of the slag layer gap and the shape of the steel shell are predefined by the domain shape, based on output from CON1D^[44] model simulations for the casting conditions of this problem. The input data for the CON1D simulations are included in APPENDIX A (Table A.1). The OM shape, assumed to be triangular in CON1D, is simplified to constant thickness over the length of the steel strand, to carry the same slag consumption. In the fluid domain, the Navier-Stokes equations, turbulence, VOF and energy equations are solved for the 2-D velocity, pressure, and temperature fields.

The second domain is solid and contains the top of the copper mold adjacent to the fluid domain. The 3D geometry of the real mold plate is accurately modeled using a 2D rectangular mold plate with effective thickness, d_{eff} , without the water channels, by applying an effective convection boundary condition.

The mold domain is slightly longer than the fluid domain on both ends, to cover the range of movement of the mold mesh. Only the energy equation is solved in this domain for the 2-D temperature field. The two domains are coupled by heat transfer across the vertically-moving coincident surfaces that connect them.

3.3 Boundary Conditions:

Slag Top Surface: This “pressure inlet”^[72] boundary is given a constant pressure, p_i , with velocity direction set to normal to the surface. The boundary temperature is set to a constant, T_a .

Slag outlet: This is another constant pressure boundary, where pressure is set to p_o (operating density^[72] is ρ_{sl}) and velocity direction is normal to the surface. Heat flux across the boundary is set to zero. To avoid convergence problems, fluid entering the domain was given a “backflow” temperature of T_b that varied linearly from the mold hot face to the steel shell surface.

Zero-Gradient wall: The vertical right side of the fluid domain is a zero-shear wall where normal (x-direction) velocities, tangential (y-direction) velocity gradients, and normal heat flux are all zero;

$$v_x = 0; \quad \frac{\partial v_y}{\partial x} = 0 \quad \text{and} \quad K_{eff} \frac{\partial T}{\partial x} = 0 \quad (3.18)$$

This condition is termed as “symmetry wall”.^[72]

Shell Cold Face: The steel side of the gap is a vertical “no-slip” wall that moves downward at a constant velocity, the casting speed ($v_x = 0, v_y = v_c$). It is given the fixed temperature profile ($T = T_{sc}$) predicted by the CON1D simulation.

Shell Hot Face: The shell contacting the liquid steel is modeled as a constant temperature ($T = T_{sh}$) stationary wall ($v_x = 0; v_y = 0$). The solidus temperature is used as T_{sh} and is calculated from the steel composition (APPENDIX A - Table A.2) using an analytical Clyne-Kurz style equation by Won^[73] in CON1D.

Steel Bottom Surface: This surface is modeled as a stationary wall ($v_x = 0; v_y = 0$) with zero heat flux ($q_s = 0$).

Mold Cold Face: The mold surface that approximates the cooling channels is a convection boundary that removes heat to the cooling water:

$$q_s = h_c(T_w - T_s) \quad (3.19)$$

Where, q_s is the cold-face heat flux, h_c is the effective convection heat-transfer coefficient, T_w is the average water temperature and T_s is the local mold surface temperature. The effect of the

water channel depth (d_{ch}), width (w_{ch}), and spacing (l_{ch}) is incorporated into h_c by treating the channels as heat-transfer fins using Eqns. 19-21 in CON1D^[35]. The equations for h_c also include an empirical heat transfer coefficient from the water-channel sides and root to the water^[74] and the thermal resistance of a scale layer (if present).

Mold top and bottom wall: The top and bottom surfaces of the mold are insulated surfaces ($q_s = 0$) because heat transfer from those surfaces is negligible^[44] and heat flow is mainly perpendicular to the mold hot face.

Mold Domain Velocity: The entire solid (mold) domain is prescribed a velocity according to the mold oscillation:

$$v_x = 0; v_y = v_m = 2\pi af \{1 - c \cos(2\pi ft)\} \cos\{2\pi ft - c \sin(2\pi ft)\} \quad (3.20)$$

where, constant, $c = 4\pi\alpha_m / (8 - \pi^2\alpha_m^2)$, amplitude, $a = s / 2$, $s =$ stroke, $f =$ frequency, and $t =$ time. The modification ratio, $\alpha_m = 4A_o f$, where A_o is the time difference between peaks of the displacement curves for non-sinusoidal oscillation and sinusoidal oscillation, where $\alpha_m = 0$; $v_m = 2\pi af \cos(2\pi ft)$. Displacement and velocity curves for a non-sinusoidal oscillation are shown in APPENDIX B (Figure B.1).

Interface (Coupled wall): The interface between the fluid and mold domains is coupled in both velocity and heat flux. This interface moves with the mold velocity ($v_x = 0$; $v_y = v_m$) and has a no-slip condition on the fluid side. The instantaneous heat flux between points on the mold and fluid domains that are currently adjacent is same at every time. Details of this method is available elsewhere.^[72]

Fluid Domain: A reference pressure of 1 atm is set at a point 5 mm below the slag top surface of the domain and 2 mm away from the zero gradient wall. To maintain the continuous supply of energy provided by the liquid steel, the temperature of the steel phase ($\alpha_{Fe} \geq 0.98$) of the entire fluid domain is kept constant at T_{sh} , which represents a small superheat temperature difference above the liquidus. The values of the different variables used in the boundary conditions are given in Table 3.1.

3.4 Powder and Slag Properties:

The mold powder and slag properties vary greatly with composition and temperature, and evolve during the process. The composition differs from that reported by the supplier because the reported F content must be converted to CaF_2 . In addition, the carbon added to slow the mold powder melting rate burns away completely during sintering, so is absent from the liquid slag.^[75] Finally, the molten slag accumulates alumina inclusions from the steel, which changes its composition during operation.

The compositions of the commercial mold powder and slag in the current work, slag P2 in Shin,^[19] are given in Table 3.2. Column 2 gives the reported composition^[19, 76] with components, X_{rep} . The reported F content is converted to CaF_2 (Eqn. 3.21), assuming that the required oxygen is provided by CaO according to the reaction: $2CaO + 4F \rightarrow 2CaF_2 + O_2$. This also requires a correction of CaO (Eqn. 3.22).

$$(CaF_2)_{cor} = \% (F)_{rep} \times \frac{M_{CaF_2}}{2 \times M_F} \quad (3.21)$$

$$(CaO)_{corr} = \% (CaO)_{rep} - \% (F)_{rep} \times \frac{M_{CaO}}{2 \times M_F} \quad (3.22)$$

Where, the molecular weights are, $M_{CaF_2} = 78.07$, $M_{CaO} = 56.08$, $M_F = 19$. To calculate the mold powder composition, X_p , the reported wt% of each component in the powder, $\%E_i$, including every oxide, $(CaF_2)_{corr}$, $(CaO)_{corr}$, and C-Total, is multiplied by the factor, F_p (Eqn. 3.23) and is shown in column 3 of Table 3.2.

$$F_p = \frac{100}{\sum \%E_i - \sum \%C_i} \quad (3.23)$$

where, $\%C_i = \text{wt\% of C-Free and CO}_2$.

To calculate the initial molten slag composition, X_{I_0} , the carbon is reduced to zero, and Eqn. 3.23 is applied to column 2 with $\%C_i = \text{C-Total, C-Free and CO}_2$ to give column 4, Table 3.2.

During operation, some of the alumina inclusions in the molten steel are “picked up” and absorbed into the liquid slag layer, which changes the slag composition and properties with time during operation. To calculate the molten slag composition during operation, (X_I) , The wt% of all elements (X_{I_0}) except alumina is multiplied by a factor, $F_{Al_2O_3}$, given by Eqn. 3.24.

$$F_{Al_2O_3} = \frac{100}{\sum G_i + \% (Al_2O_3)_{pickup}} \quad (3.24)$$

where, $\%G_i = \text{wt\% of all slag components including Al}_2\text{O}_3$. The wt% of Al_2O_3 increases by multiplying $F_{Al_2O_3}$ by the sum of the initial alumina in the slag and the alumina pickup. The final slag composition during operation is given in column 5, Table 3.2 for slag P2 assuming 6.94% Al_2O_3 pickup.

3.4.1 Slag Viscosity:

Several models have been developed to estimate molten slag viscosity based on its composition and temperature during cooling, based mainly on Arrhenius or Weymann relations.^[77-80] A widely used model, by Riboud^[77] based on 45 slags, gives slag viscosity as

$$\mu = AT \exp\left(\frac{B}{T}\right) \quad (3.25)$$

where, T is temperature in Kelvin and A, B are parameters defined as follows

$$\begin{aligned} \ln A = & -19.81 + 1.73(X_{CaO} + X_{MnO} + X_{MgO} + X_{FeO} + X_{B_2O_3}) + 5.82X_{CaF_2} \\ & + 7.02(X_{Na_2O} + X_{K_2O} + X_{Li_2O}) - 35.76X_{Al_2O_3} \end{aligned} \quad (3.26)$$

$$\begin{aligned} B = & 31140 - 23896(X_{CaO} + X_{MnO} + X_{MgO} + X_{FeO} + X_{B_2O_3}) - 46356X_{CaF_2} \\ & - 39519(X_{Na_2O} + X_{K_2O} + X_{Li_2O}) + 68833X_{Al_2O_3} \end{aligned} \quad (3.27)$$

Here, X_i is the molar fraction of the i^{th} compound.

Alumina content in the molten slag can increase as much as 30%^[55] during casting. The temperature-dependent viscosity of the Shin-P2 molten slag, based on 2.31%, 5.15%, and 6.94% Al_2O_3 pickup are calculated using the Riboud model and compared in Figure 3.2 along with the measured viscosity by Shin^[19]. The results show that the viscosity increases with increasing alumina pick-up, which agrees with the observations of many previous experimental studies.^[81-82] Considering a typical fraction of alumina inclusions absorbed from the steel into this slag, a ~7% pick-up is assumed for the current model simulations of the commercial process.

A limitation of the Riboud model is that it does not predict the abrupt increase in viscosity observed at some temperature during cooling,^[81] termed the break temperature (T_{Br}). The following power-law relation^[35] captures this phenomenon-

$$\mu = \mu_o \left(\frac{T_o - T_{fsol}}{T - T_{fsol}} \right)^n \quad (3.28)$$

where, T_{fsol} and n are chosen empirically to fit measured data and μ_o is the viscosity measured at the reference temperature, T_o chosen to be 1300°C. Here, Eqn. 3.28 was used with “ n ” and “ μ_o ” of 1.8 and 0.55 Pa·s respectively, selected for CON1D simulations to match the Riboud model near 1533°C to 1200°C. To avoid numerical difficulties in the current model with very high viscosity at lower temperatures, the viscosity below 627°C, was truncated to a constant (10⁵ Pa·s). The result is shown in Figure 3.3 for the Shin-P2 slag with 6.94% Al₂O₃ pick-up. This curve to model viscosity of the molten slag during cooling and solidification or crystallization was applied near the mold wall, as shown in the solidification zone in Figure 3.1, which has width x_{sol} , and includes the region above the slag rim.

In the top of the domain, where the mold powder sinters and melts, a different model was needed to characterize the slag viscosity. According to a previous review^[83] and the previous model of powder viscosity by McDavid,^[12] as temperature increases, the mold powder viscosity increases as it sinters to form a semi-solid which has more resistance to flow than the powder. As it melts more fully, this resistance decreases, so the viscosity decreases again. These phenomena are taken into account in the viscosity model for heating, sintering, and melting powder, shown in Figure 3.3.

3.4.2 Slag Thermal Conductivity:

Two different effective slag thermal conductivities are used during heating and cooling, as shown in Figure 3.4. The powder contains air which gives the mixture a low conductivity, ~ 0.3 W/m·K.^[84] As the powder heats, sinters, coalesces,^[5] and melts, the air disappears^[85] so its thermal conductivity gradually increases. Above the melting temperature, a constant effective thermal conductivity (3 W/m·K) is used in the current model of slag P2. This assumes that the decrease in phonon conductivity with increasing temperature is balanced by the increase in radiation^[86], which agrees with the model of McDavid^[54] and the measurement of constant conductivity in molten slag systems of Hasegawa^[87]. During cooling below the solidification temperature, Kishimoto's^[88] conduction measurements for solid slag similar to P2 are adopted, which show decreasing conductivity with decreasing temperature. The thermal conductivity of the Badri slag has similar trends, but was assumed to have lower conductivity, due to the increased oxidation, gas bubbles, and crystal defects, that likely accompany the less-well-controlled lab experiment.

3.4.3 Slag Specific Heat and Density:

The specific heat of slag in the current model is given in Figure 3.5. Measurements by Mills et al.^[11] show a sharp increase in effective c_p at the glass transition temperature, T_g , due to the enthalpy of transition (ΔH) between liquid slag and solid. Density of the slag is fixed at 2500 kg/m³.^[19]

3.5 Other Material Properties:

The surface tension of the interface between the molten steel and slag, $\gamma_{Fe(l)-sl}$, was calculated using Girifalco and Good's approach.^[89]

$$\gamma_{Fe(l)-sl} = \gamma_{Fe(l)-gas} + \gamma_{sl-gas} - 2\Phi(\gamma_{Fe(l)-gas} \times \gamma_{sl-gas})^{0.5} \quad (3.29)$$

where Φ represents attraction between the phases and for CaO-Al₂O₃-SiO₂ ternary system is given by;^[89]

$$\Phi = 0.003731 \times (\%Al_2O_3) + 0.005973 \times (\%SiO_2) + 0.005806 \times (\%CaO) \quad (3.30)$$

For the final molten slag composition in Table 3.2 column 5, Φ from Eqn. 3.30 is 0.4281. Extensive measurements of steel surface tension ($\gamma_{Fe(l)-gas}$)^[89-93] show the importance of sulfur content. For ~0.011%S, $\gamma_{Fe(l)-gas}$ is 1.6 N/m in Ar gas. Surface tension (γ_{sl-gas}) of the (Shin-P2) commercial slag was supplied^[19, 76] as 0.419 N/m. From Eqn. 3.29, the surface tension between liquid slag and steel is calculated to be 1.3 N/m.

Finally, the static contact angle (θ_{eq}) between liquid steel and liquid slag on solid steel was determined to be 160°, based on Ojeda,^[59] using Young's equation^[94] for this three phase system.

During casting sometimes air gaps forms between the mold hot face and solid slag layer. The thermal conductivity of the air in this air gap is significantly different than natural air. The presence of H₂ in the trapped air causes the thermal conductivity to vary greatly based on volume percentage of H₂. Nakato^[95] showed that conductivity of Nitrogen-Hydrogen mixture can vary from 0.03 to 0.17 W/m·K. In current model the conductivity of air gap is taken as 0.06 W/m·K. The liquid steel and copper (mold) properties are constant, given in Table 3.3.

3.6 Solution Procedure:

The coupled transient energy equation and incompressible Navier Stokes equations are discretized using the finite volume method (FVM) and solved on a fixed, structured grid with quadrilateral elements for temperature, pressure and velocity field using ANSYS FLUENT 13.0.

While velocities and turbulence quantities are saved in cell-centers, pressure is computed in the face center using PRESTO scheme which mimics the staggered arrangement. Spatial discretization used second order upwinding for advection terms and a second-order central difference scheme with a least-squares gradient method for the diffusion terms. First-order implicit scheme is used for transient solution. A pressure-based segregated algorithm, Pressure-Implicit with Splitting of Operators (PISO), is used for coupling pressure and velocity. The VOF equation is solved using explicit time discretization and a geometric reconstruction scheme for face fluxes in cells where the interface is located.

This coupled transient thermal-flow problem is solved in several steps. First, the CON1D model is run to estimate the size of the interfacial gap, shape of the solidified steel shell, temperature profile of the mold cold face, air gap thickness, cooling water temperature and convection heat transfer coefficient. The solution starts with an initial guess of the phase fraction field, based on for the slag / steel interface shape calculated with Bikerman's equation,^[96]

$$x = x_o - \sqrt{2b^2 - z^2} + \frac{b}{\sqrt{2}} \ln \frac{b\sqrt{2} + \sqrt{2b^2 - z^2}}{z} \quad (3.31)$$

where,

$$x_o = b - \frac{b}{\sqrt{2}} \ln(\sqrt{2} + 1) \text{ and } b^2 = \frac{2\gamma_{Fe(l)-sl}}{g(\rho_{Fe} - \rho_{sl})} \quad (3.32)$$

Here, x = horizontal distance from the wall where the phases meet, z = vertical distance from the free surface. Then, the guess is improved by solving the steady isothermal flow equations including the VOF model, Eqns. 3.1-8, assuming constant slag viscosity (0.1 Pa·s) and no mold or shell movement. Next, the initial temperature field is obtained by solving the energy equation system, Eqns. 3.9-11, based on the phase fraction field with no flow. Finally, the complete

transient coupled system of thermal-flow equations (Eqns. 3.1-3.17) are solved, with the mold domain moving according to the oscillation equation and the cold face of the steel shell moving downward at the casting speed. The solution is considered converged when results over successive oscillation cycles are the same, which usually takes only a few cycles.

For the Shin Case, with a fixed time step of 10^{-5} s and fine mesh (1,76,450 cells with 0.1×0.1 mm cells near the interface and mold hot face) the ~ 0.4 s simulation takes 24 hrs of computation on an Intel® Xeon® CPU with 6×2.6 GHz cores PC. The Badri Case needed only 99,064 cells, for the same 0.1×0.1 mm refinement. The parametric study cases used a simplified domain with coarser mesh (5340 cells) after mesh independence studies showed reasonable accuracy, which required only 2.5 hrs per 1 s run. In all cases, cells are smaller where the interface is expected to be located and in the gap where high temperature gradients and rapid changes in properties are expected.

3.7 Figures:

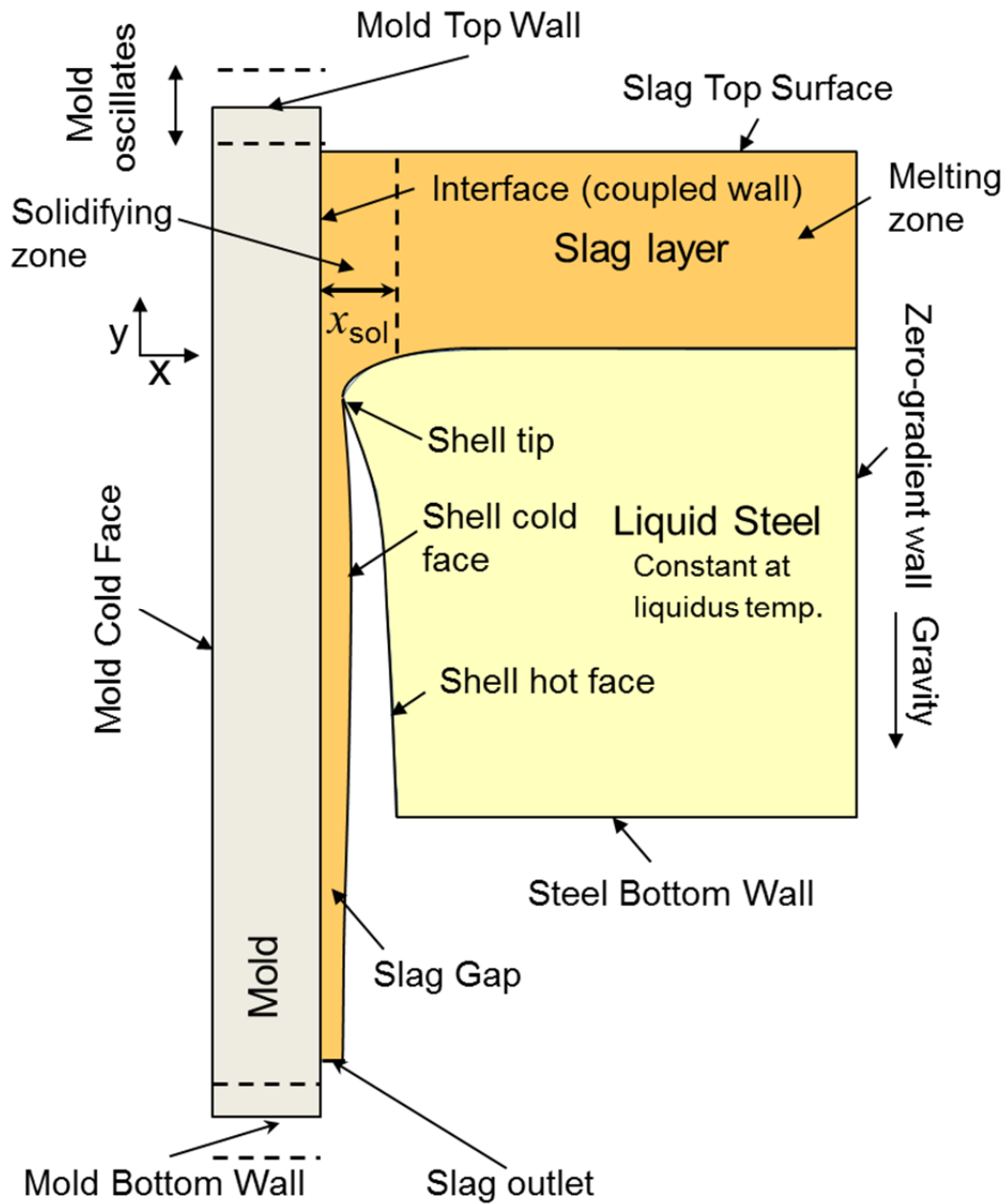


Figure 3.1: Schematic of model domain and boundaries (not drawn to scale).

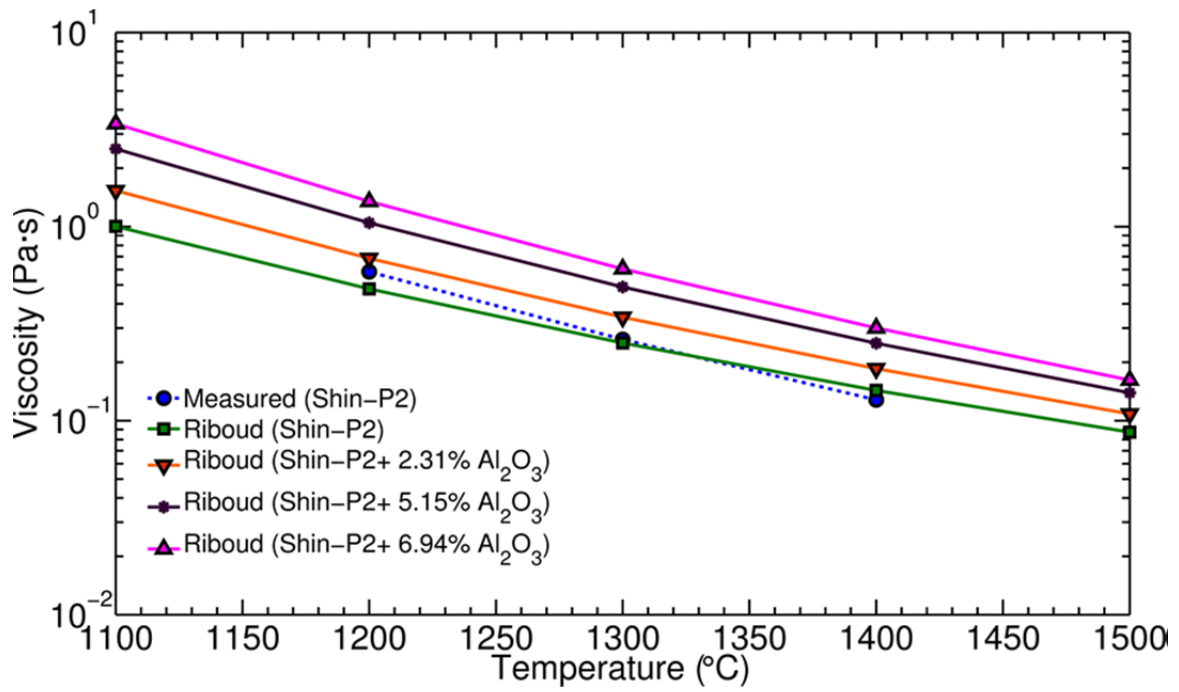


Figure 3.2: Temperature dependent slag viscosity predicted by Riboud model for different %Al₂O₃ pickup vs. measured values.

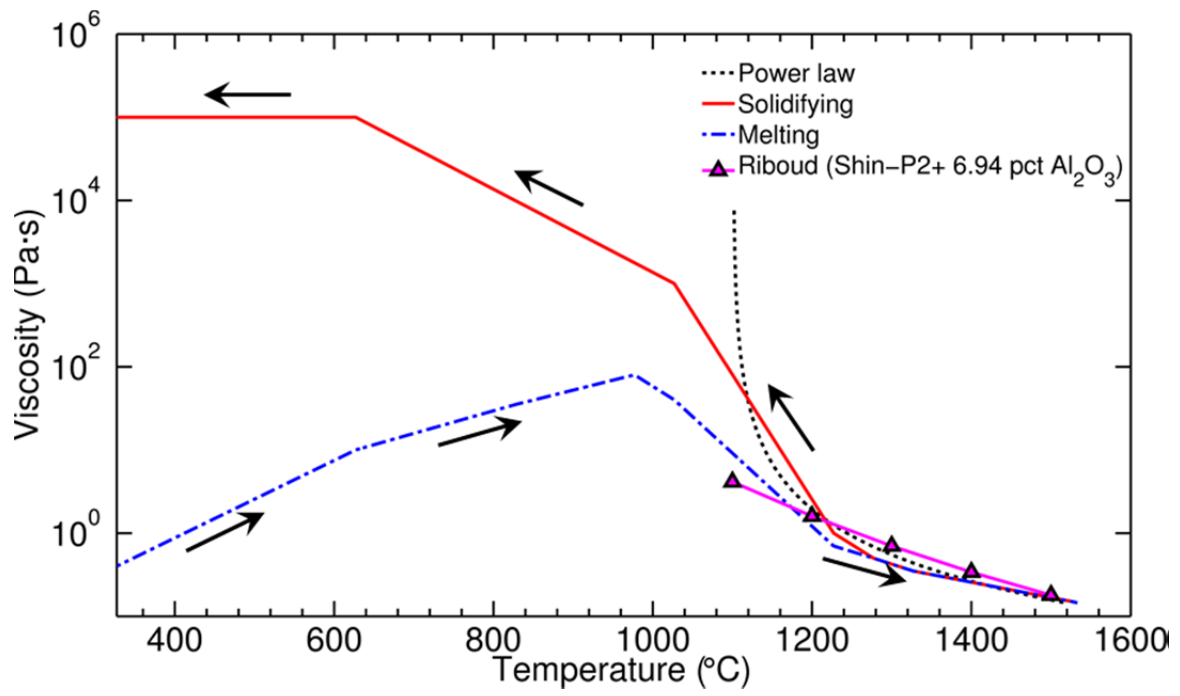


Figure 3.3: Temperature dependent viscosity model during solidification and melting.

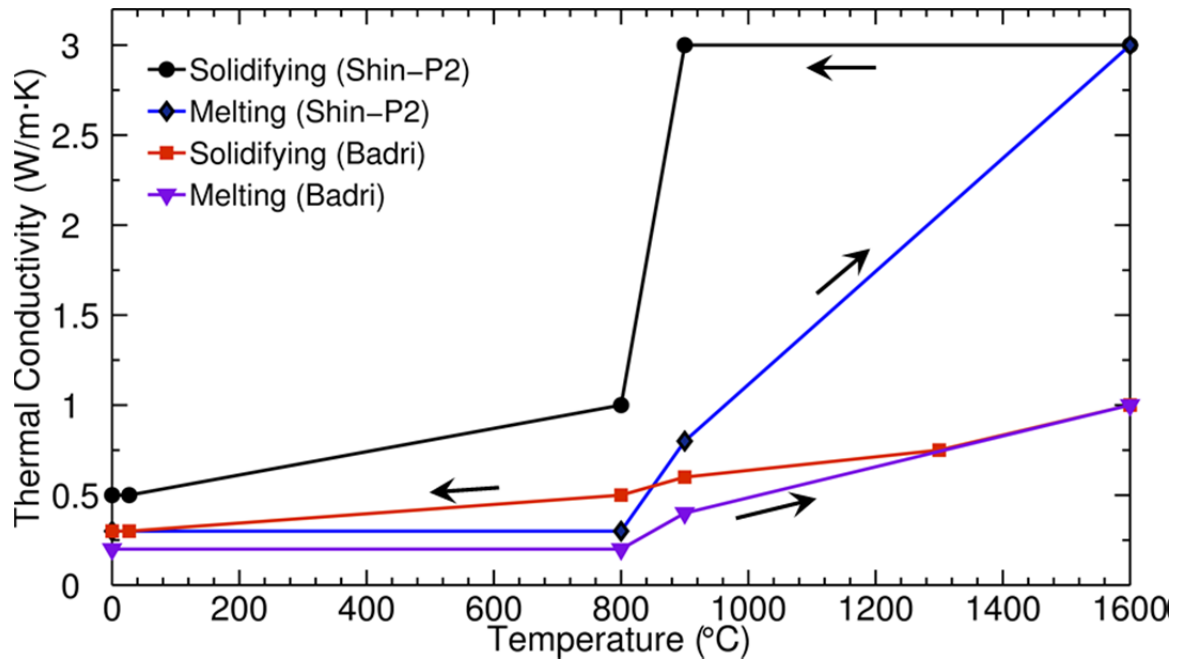


Figure 3.4: Temperature dependent thermal conductivity model for slag melting and solidifying.

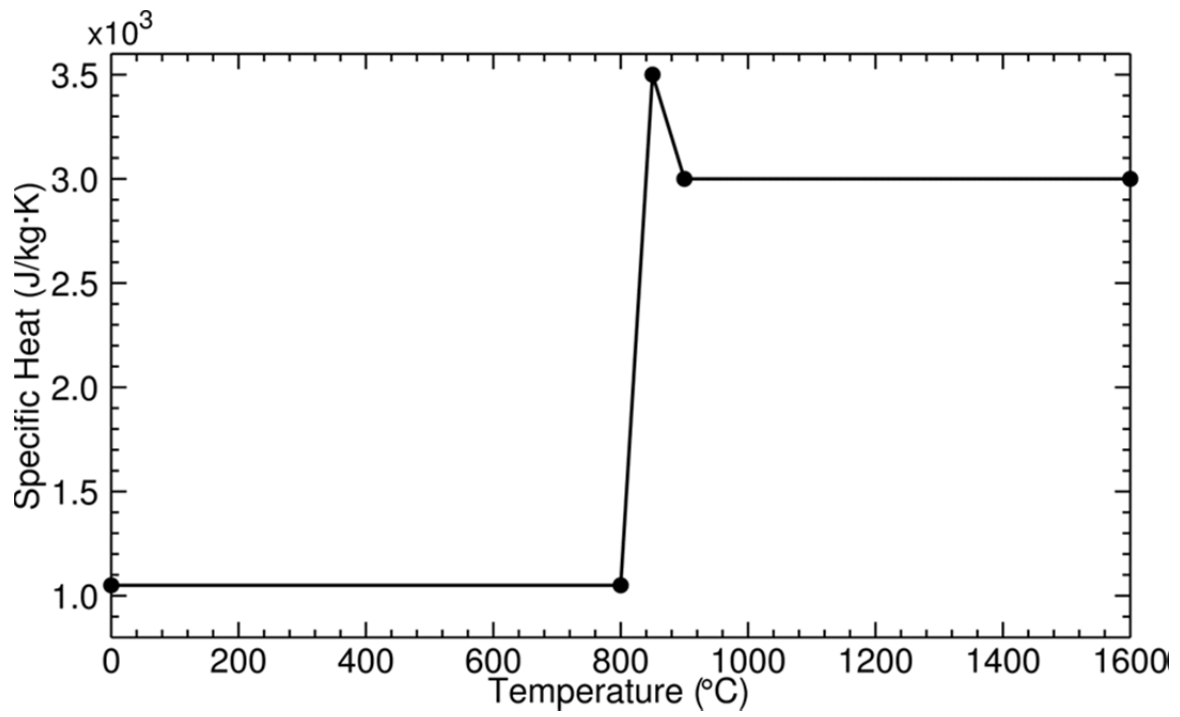


Figure 3.5: Temperature dependent specific heat of slag.

3.8 Tables:

Table 3.1: Variables used in model.

Variable	Shin Case	Badri Case
Mold Geometry		
d_{ch}	20 mm	13.65 mm
w_{ch}	5 mm	7.9 mm
l_{ch}	19 mm	15.8 mm
d_{eff}	20 mm	8.58 mm
Boundary Conditions		
p_i	1 atm	1 atm
p_0	1 atm	1 atm
h_c	45272 W/m ² ·K	16720 W/m ² ·K
T_a, T_w	40°C	37.85°C
T_r	27°C	37°C
T_b	223°C-1362°C	1127°C
T_{sc}	$f(y)$, 1532.9°C-1361.72°C	1518.7°C
T_{sh}	1532.9°C	1531.87°C
Casting Conditions		
v_c	0.02323 m/s (1.39 m/min)	0.0127 m/s (0.762 m/min)
s	5.89 mm	6.3 mm
f	2.9 Hz	1.3 Hz
α_m	0	0

Table 3.2: Mold slag composition.

Components	Reported By Suppliers, X_{rep} (wt%)	Powder Composition, X_p (wt%)	Initial Molten Slag Composition, X_{i0} (wt%)	Final Molten Slag Composition, X_1 (wt%) (~7% Al_2O_3 pickup)
SiO ₂	37.77	39.48	40.58	37.94
CaO	37.88	28.42	29.21	27.32
MgO	1.98	2.07	2.13	1.99
Al ₂ O ₃	4.99	5.22	5.36	11.5
TiO ₂	0.03	0.03	0.03	0.03
Fe ₂ O ₃	0.31	0.32	0.33	0.31
MnO ₂	0.04	0.04	0.04	0.04
P ₂ O ₅	0.01	0.01	0.01	0.01
Na ₂ O	3.75	3.92	4.03	3.77
K ₂ O	0.11	0.11	0.12	0.11
F	7.22	-	-	-
CaF ₂	-	15.47	15.9	14.87
B ₂ O ₃	1.2	1.25	1.29	1.21
Li ₂ O	0.9	0.94	0.97	0.9
C-Total	2.59	2.71	-	-
C-Free	1.62	-	-	-
CO ₂	3.24	-	-	-

Table 3.3: Properties of liquid steel and Cu (Mold).

Properties/Material	Steel	Cu (Mold)	Unit
Density	7000	8900	kg/m ³
Thermal Conductivity	30	350	W/m·K
Specific Heat	700	385	J/kg·K
Viscosity	0.0063	---	Pa·s

CHAPTER 4: VALIDATION CASES

The model is validated by simulating two cases where different experimental and plant measurements were available. First, a typical commercial parallel-walled slab caster is simulated, and the predicted slag consumption is compared with plant measurements by Shin^[67] to validate the flow field. Second, a steel continuous casting simulator by Badri^[65-66] is modeled, and the predicted temperatures in the mold wall are compared with thermocouple measurements in this experimental apparatus to validate the heat transfer model.

4.1 Commercial Caster (Shin) Case:

For simulating the commercial caster, where extensive, accurate slag consumption measurements were available, the casting conditions, mold geometry, and material properties described by Sengupta et al.^[60] and Shin et al.^[19] are used. The effective mold thickness is 20 mm for this commercial slab casting mold, with its 40 mm thick mold plates and 20 mm deep water channels. The composition for slag P2 is given in Table 3.2 column for an assumed 6.94% Al₂O₃ pickup and its temperature-dependent properties are given in Figures 3.3-5. Casting conditions and steel properties for this case are given in Table 3.1 and 3.3 respectively. From the shell tip to the fluid domain bottom (100 mm below), the slag gap thickness increases from 0.665 mm to 0.981 mm thick (APPENDIX B: Figure B.2) and the shell thickness increases from 0 to 4.13 mm. There is no air gap for this case. Further conditions needed as input to CON1D to determine the shell thickness, gap size, and thermal parameters for this typical commercial casting condition are given in APPENDIX A (Table A.1). The start time of the final thermal-flow stage in Fluent is 0.77 s (2.25cycles) before t=0 where converged results are presented for one oscillation cycle.

4.2 Experimental Simulator (Badri) Case:

Badri^[66] measured temperatures in a steel continuous-casting mold simulator with 6 pairs of thermocouples located 1.5 mm (termed “Hot”) and 5 mm (termed “Cold”) from the hot face of the mold, as shown in Figure 4.1. The effective mold thickness is 8.58 mm for the dimensions of this mold plate and its slots, which are shown in Figure 4.1. The current model predictions for this experiment are compared with the 12 temperature histories measured during the experiment and reported in Figure 176 in Badri^[97] for Trial 32. Further experimental details are given by Badri.^[65-66]

The 100 mm long slag gap for this case decreases in thickness from 0.9 mm to 0.04 mm from shell tip to 12 mm below it, then increases to 0.427 at domain exit (shown in APPENDIX B: Figure B.3). The shell thickness increases from 0 to 2.5 mm from shell tip to domain exit. The contact resistance and drop in heat transfer due to cracks and bubble formation during crystallization of the cooling slag is modeled as an air gap between the mold and slag layer. This air gap thickness increases from 0.05 to 0.21 mm at the meniscus to the bottom of the fluid domain exit (shown in APPENDIX B: Figure B.3). Further conditions input to CON1D to determine the shell thickness, gap size, and thermal parameters for this case are given in APPENDIX A (Table A.1). Converged results are presented for the 5th oscillation cycle.

4.3 Flow Field Results:

The flow field in the meniscus region during one oscillation cycle is dominated by the oscillating mold along with the solid slag rim and their effect on interface between liquid slag and steel. The Badri and Shin case show similar flow behavior.

Taking the Shin case as an example, Figure 4.2 shows the displacement, velocity of the mold and casting speed during one oscillation cycle. The time when the mold moves downward faster than the casting speed is termed Negative Strip Time (NST, t_n). The rest of the period is called Positive Strip Time (PST, t_p).

The velocity field variations and changing shape of the slag / steel interfacial meniscus ($\alpha_{Fe}=0.5$) for one oscillation cycle (0.77-1.12 s) are shown in Figure 4.3(a-f). Starting from zero displacement with the mold moving upward at maximum velocity, Figure 4.3(a) shows that the rising slag rim pulls the meniscus upwards. This meniscus bulging lags behind the slag rim and has less movement. This causes the gap between the slag rim and the meniscus (region 1) to expand. Some of this slag is drawn upward into region 1 from the gap between the mold and steel shell (region 2).

After passing its highest position, the downward-moving slag rim starts to squeeze region 1, as shown in Figure 4.3(b-c). Combined with drag from the downward-moving mold, slag starts to enter region 2 to be consumed into the gap, just before the start of NST at 0.11 s. Figure 4.3(c) at 0.14 s shows slag being pushed out of region 1 both far away (right), and down into region 2. This flow increases as the mold reaches its maximum downward velocity at ~ 0.17 s (Figure 4.3(d)). The increasing pressure can be seen in Figure 4.4 at a location 0.5 mm above the shell tip and 0.4 mm from the hot face. The maximum pressure is reached just after NST at 0.258 s, when the mold is at its lowest position with zero velocity (see Figure 4.2). At this time, the slag rim is pushed closest to the meniscus and region 1 is smallest. As the mold moves upward again, the slag “pumping” decreases and at 0.26 s (between Figure 4.3(e) and Figure 4.3(f)) the flow direction reverses again.

This sequence of flow variations is repeated for every oscillation cycle. This mechanism is consistent with that proposed in previous work^[58, 60]. The movement of the three-phase contact line (point in this 2D model) between the steel/slag interface and the wall matches closely with the mold wall oscillation. This agrees exactly with previous observations in lab experiments using mercury or water with silicon oil.^[6-7]

4.4 Slag Consumption Results:

The current model predicts the transient behavior of slag consumption during an oscillation cycle. Both cases show similar behavior which is explained here using the Shin case in Figure 4.5. The negative sign means slag is flowing downward (positive consumption). The oscillating slag consumption curve (Figure 4.5) closely follows the oscillating mold velocity, which agrees with Anzai.^[23] Slag consumption is positive only from 0.0846 to 0.2621 s, which overlaps NST. Slag is drawn upwards during the rest of the cycle. The result is an average consumption of 0.0051 kg/m·s or 0.220 kg/m². From Shin,^[67] the measured consumption calculated for this slag, assumed to include alumina pickup, ($k_c=14$) and casting conditions is 0.236 kg/m². This agrees with the prediction within 8%. The disagreement might be due to treating the oscillation marks as effective thickness^[44] over the whole gap. Slag properties might be another source of error, as viscosity affects the slag consumption greatly.^[98] Taking the errors into account, the model predictions of slag consumption agree well with measurements.

Consumption is found by integrating the velocity profile across the gap. Figure 4.6 shows the liquid and solid slag thickness across the gap grows slightly with distance down the mold, but varies very little during an oscillation cycle. Figure 4.7 shows the slag velocity profile across the gap, which oscillates with the mold over most of the gap, owing to the high viscosity of the solid slag near the wall. Slag is only consumed due to velocity variations in the thin liquid layer near

the shell. Velocity profiles at different distances down the mold are nearly the same, except near the domain outlet due to the thermal backflow boundary condition. These results suggest that consumption is controlled more by drag inside the gap than by pressure at the meniscus.

Increasing gap size was found to increase consumption somewhat. Gap size is determined by the CON1D model, based on the casting conditions and calibration with measurements. Consumption for the Badri Case is much larger than the Shin case and calculated to be 1.23 kg/m² (see APPENDIX C.1 for details), owing to the increased gap size, which is due to the decrease in casting speed and increase of stroke.

4.5 Temperature Results:

Transient temperature predictions are shown in Figure 4.8 at the 6 hot thermocouples locations for the Badri case. Here the locations are fixed in space in the laboratory (“Eulerian”) reference frame so do not oscillate with the mold. Predictions for each oscillation cycle are similar, indicating that the model has reached its intended pseudo-steady state. The temperatures measured by the 6 pairs of thermocouples by Badri^[97] are shown in Figure 4.9. Because the thermocouples oscillate with the mold in a moving (“Lagrangian”) reference frame, they are not expected to match with Figure 4.8. Time averaged temperatures calculated and measured over six oscillation cycles are compared in Figure 4.10 and a reasonable match is observed. Maximum temperature is found near the meniscus (TC4), especially in the measurements, and decreases more above the meniscus.

Figure 4.11 was constructed to predict the thermocouple results at TC3, TC4 and TC5 locations during a representative (5th) oscillation cycle, by oscillating the reporting locations appropriately with time. The corresponding mold velocity and displacement curves are shown in Figure 4.12.

Figure 4.11 also includes the measured transient temperatures over six different cycles by Badri et al.^[66]

To extract the measured temperatures into Figure 4.11 required making some uncertain decisions. The far-field free surface location was taken as the “meniscus” location, reported by Badri to specify the vertical locations of the thermocouples, and is 4.5 mm above the shell tip. This reference is taken because it is very likely that meniscus location measuring device used in this experiment, such as an eddy current sensor, measures the far-field interface between slag and steel. Time starts at the beginning of the 0.258 s NST (marked with an arrow in the shaded region) for the reported oscillation period of 0.77 s for this case.^[66] This was done for easy comparison with 0.175 s NST (0.83 s period) found in Figure 273 of Badri^[97] for this same case. Offsetting the time axis to properly align the heat flux and temperature curves was difficult.

In Figure 4.11 the measurements show great variations between oscillation cycles, which are not modeled. However, the average temperature variations over a single cycle match reasonably well. As expected, thermocouples closer to the meniscus show larger temperature variations during each cycle, which are also summarized in Figure 4.10. This is due to greater variations in heat flux. For example, the maximum amplitudes, which are predicted at TC4 of 1.37 °C (cold) and 3.22 °C (hot) compare well with the measured amplitudes of 1.35 °C and 3.04 °C. The amplitudes further below the meniscus, such as at TC5, are all clearly smaller.

During a single oscillation cycle, the predicted temperature increases to a maximum sometime during the NST, and then falls. This is consistent with many of the measurements, which show a mixture of trends. For example, at TC4, the measured temperature increases during NST for 3 of the cycles but decreases during the other 3. Measured temperatures from similar experiments

with ultra-low carbon steel by Badri (Trial 30, 31 and 35; Badri^[97]) show other trends. Figure 4.13 shows that temperature for TC3 in Trial 31^[97] consistently increases during NST.

4.6 Phase Lag Results:

Temperature measurements in transient conditions always experience phase lag,^[99-100] which increases with distance of the thermocouple from the surface where the varying heat flux is applied. Temperature, $T(x,t)$, near a surface subjected to a spatially-constant heat flux that oscillates in time as $q = q_o \cos \omega t$ is given by the following semi-infinite solution.^[99]

$$T = T_o + \frac{q_o}{k} \left(\frac{\alpha_T}{2\pi f} \right)^{0.5} \exp \left[-x \left(\frac{\pi f}{\alpha_T} \right)^{0.5} \right] \cos \left[2\pi f t - x \left(\frac{\pi f}{\alpha_T} \right)^{0.5} - \frac{\pi}{4} \right] \quad (4.1)$$

where, $\alpha_T = K / \rho c_p$. The surface temperature ($x=0$) lags by $\frac{\pi}{4}$ or 12.5% of the oscillation period. Thermocouple measurements, and their model predictions, should show longer phase lags, increasing with distance from the surface. For the 1.3 Hz (0.769 s time period) of the Badri case, the surface, hot, and cold thermocouples should experience lags relative to the heat flux of 0.098, 0.133, and 0.219 s respectively. For the 2.9 Hz (0.345 s time period) of the Shin case, these same three lags are 0.043, 0.068, and 0.126 s.

Although the meniscus region is a highly 2D heat flux region, it is useful to compare the current model results with the theoretical phase lags from the 1-D equation. The current model of the Badri Case predicts phase lags averaged over the six oscillation cycles of 0.038, 0.058, and 0.095 s for the surface, hot, and cold thermocouples at TC3 respectively. For the Shin Case, the predicted phase lags average 0.025, 0.046 s for the hot and cold TC3 respectively.

Although these time lags are shorter than the 1D solution, they show the expected trends for both cases. Specifically, time lags increase with distance from the hot face surface and decrease with increasing frequency from the Badri case to the Shin case. The lower magnitude in the model is likely due to the 2D heat flux experienced in the meniscus region.

From Badri's raw temperature measurements (Figure 4.9) the lags between the thermocouple measurements for hot and cold locations were observed to vary from 0.024 to 0.033 s except for the highest value of 0.083 s at TC1. Typical averaged model predictions are 0.031 and 0.037 s at TC2 and TC3 respectively, while at TC4, the thermocouple that travels below shell tip during oscillations, shows 0.065 s lag. The short lag in the model predictions can be seen in Figure 4.11 between hot and cold locations. These values match very well, considering the extensive variations observed in both the model and the measurements. The lags in both the experiment and the model are shorter than the analytical solution, which suggests that the 2D effects are real.

4.7 Heat Flux Results:

Figure 4.14 compares the Lagrangian and Eulerian predictions of temperature at TC 3 (Hot) and adjacent surface heat flux for the Badri Case. As discussed in the previous section, the phase lag is very short relative to the period of the cycle, so the temperature and heat flux rise and fall almost together. As the mold rises above the far-field interface level, the heat flux increases because of the upward bulging of the interface above the shell tip and the opposite occurs while the mold moves down, as illustrated in section 4.3. So, in Eulerian ref. frame, heat flux increases during upstroke and decreases during downstroke.

The temperature variations of the oscillating thermocouple (Lagrangian reference frame) are much smaller because the heat flux variations over the distances traveled almost match the mold

oscillation. However, as the Lagrangian TC moves down with the mold during NST, it is carried closer to the high heat-flux meniscus region and an increase is observed in temperature and heat flux. Badri et al.^[66] observed that heat flux calculated with a 1-D inverse model based on the TC3 temperature history increases during NST and reaches peak value at the end of it. To maintain the short phase lag between heat flux and temperature, the measured temperature curves for TC3 in Figure 4.9 should have been shifted slightly left in order to increase during NST (reconstructed figure of measured temperature, without the shift, during the oscillation cycles are shown in APPENDIX B: Figure B.4 that shows reported temperatures will decrease during NST which does not match with the heat flux behavior). This would also enable a close match with the current model predictions, as well as with the TC3 measurements of Trial 31^[97] (Figure 4.11). Furthermore, the Badri inverse model trend of increasing heat flux during NST for the TC3 history is close to that predicted by the current model (Figure 4.14), where the heat flux and temperature peaks at TC3 are both towards the end of NST (averaging $66\pm 5\%$ and $85\pm 3\%$ after start of NST respectively). Thus, the current model reasonably explains the experimental observations.

Figures 4.15 and 4.16 show the Eulerian predictions of temperatures at TC (hot) locations and heat flux for the Badri (fifth cycle) and Shin (third cycle) cases respectively, during one cycle. Near the meniscus and shell tip (TC3-4), amplitudes are highest. Farther from the shell tip (TC5-6) they are almost uniform in time. Temperatures near the meniscus fall during NST according to the drop in interface level, which follows the mold movement, as discussed previously. However, TC5-6 increase during NST for the Shin Case. This is due to overflow of molten steel over the shell tip that occurs during NST, which is not seen in the Badri case simulation.

In case of Lagrangian ref. frame, both temperature and heat flux prediction depend on where the thermocouple is located at that instant. Figure 4.17 shows the Lagrangian prediction for TC3-5 (Hot) for Bari case (fifth cycle). TC3 travels from 5.65 mm above the shell tip to 0.65 mm below shell tip. As a result, when it comes near the shell tip during NST and after it, the temperature although small in magnitude, an increase is observed. The highest heat flux corresponds to the minimum distance from the slag/steel interface. The air gap is constant in the range TC3 travels and does not have any effect on the heat flux variation.

For TC4 (Figure 4.17) which travels 0.35 mm to 6.65 mm below shell tip, a noticeable decrease is observed when it moves downward far from the shell tip. From 3.1 s to 3.27 s, the mold moves upwards and TC4 moves up from its zero displacement position. During this time the slag gap increases while the air gap is constant (0.05 mm). As a result a drop in heat flux is observed. At 3.27 s, TC4 reaches maximum upstroke and comes down after that time. Heat flux also decreases during this time. From 3.48 s to 3.64 s, there is sudden change in air gap size at 4 mm below the shell tip (air gap thickness increase linearly from 0.05 mm to 0.08 mm from 4 mm to 8.5 mm below meniscus). Although the liquid gap thickness also varies in this region (0.8 mm at 4 mm, 0.545 mm at 6.3 mm and 0.39 mm at 8.5 mm below meniscus), the increase of air gap determines the heat flux because of its low conductivity. After reaching the maximum down stroke at 3.64 s, the heat flux increases again as TC4 moves up. The heat flux prediction in TC4 shows the effect of having sudden change in air gap thickness in the gap. Similar effect will be observed if there are OMs which are filled with slag or has some air entrapped, because the effect of that is effectively same on the heat transfer, a sudden change in resistance to heat transfer^[101].

In Figure 4.17, TC5 shows an increased heat flux when it moves upwards towards the shell tip during the upward movement of the mold while traveling from 12.65 mm to 6.35 mm below the shell tip. TC5 also shows the effect of air gap on heat flux, except, there is no sudden change in air gap thickness. All though the slag gap size varies in this regions, based on the reasons mentioned before, as TC5 moves up the air gap size decrease and it experiences higher heat flux and heat flux decreases when it moves down to regions of higher air gap size.

TC3 (Figure 4.17) and thermocouples above it match the observed behavior by Badri where in each oscillation cycle the thermocouple in the meniscus experiences an increased heat flux during NST. As expected, TC4 has the highest heat flux during an oscillation because it oscillates near the shell tip where the three-phase contact point moves in a similar pattern as the thermocouple. For heat fluxes below the shell tip, the effect of air gap size is dominating in the case when there is no overflow. In case of overflow, different behavior may be observed in the heat flux curve which is discussed later. One point to note from the Lagrangian temperature and heat flux curves is that while the temperature fluctuations are between $\sim 1^\circ\text{C}$ to 3°C , there is a huge fluctuation in the heat flux curves around 0.5 MW/m^2 . So, in plant measurements when small fluctuations are observed in the temperature measurements, it can be interpreted as large variations in heat flux at that location.

Lagrangian model predictions for the Shin case are shown in Figure 4.18 (third cycle) and 4.19 (second cycle). Thermocouples above the shell tip (TC3) show similar behavior to ones located in similar locations in the Badri case. Although temperature magnitudes are higher for the Shin case the amplitudes are lower. Eqn. 4.1 supports this observation, which clearly shows a drop in the amplitude of the temperature predictions with increase of frequency. The maximum heat flux is observed almost at the end of NST. However, Shin case predicts overflows where the liquid

steel flows over the shell tip (Figure 4.20) and continues to flow in the shell cold face. The effect of the overflow is observed by TC4-TC6 locations. In reality, the overflow liquid will solidify and stick to the shell and the effect of that would only be observed in the thermocouple close to the shell tip (TC4).

Figure 4.19 reports temperature and heat flux for TC4 (Shin Case), located 2.5 mm below the shell tip, as a representative oscillation cycle (second cycle) where overflow is observed and shown in Figure 4.20. The interface between steel/slag is drawn based on $\alpha_{Fe}=0.2$ for illustrating the overflow. During the overflow, the mold carries TC4 downward to move in line with the overflow during the heat flux peak near the end of NST. This naturally produces a temperature increase at TC4, after the expected short phase lag. This matches with Badri's observation of increasing heat flux during NST at location TC3. In the actual experiment by Badri, overflow likely was triggered by the moving meniscus to occur during NST for many successive cycles, resulting in heat flux increasing to a maximum towards the end of NST, at the thermocouple adjacent to the overflow. However, as seen from Figure 4.11 and 4.13 many different variations were observed in the measured temperature curves, which suggest that the overflow likely occurs at different times in different experiments or at different oscillation cycles during the same experiment. Since the phenomena are highly transient, this is not surprising. Similar variations are observed in the simulations.

Far below the meniscus, heat flux generally decreases with distance down the mold, owing to increasing gap resistance, which causes heat flux to decrease during NST. So, heat flux decreases as thermocouples move down in downstroke during NST in these regions. In rare locations, an inversion can occur, where heat flux increases with distance, resulting in heat flux increasing very slightly during NST to peak when the mold is lowest, near the end of NST. This situation,

shown for the current model for Badri case in Figure 4.21 which reports transient heat flux predictions of 3 locations 43.5, 48.5, 53.5 mm below the meniscus (TC7, TC8 and TC9 respectively). In these locations both the Lagrangian and Eulerian curves show same trend of increasing during NST. As expected, the magnitude of variation of Eulerian is higher than Lagrangian predictions and in the both cases the magnitude of the heat flux is substantially small compared to the meniscus. Predictions by Lopez's^[61] model for location 45 mm below meniscus (Eulerian) matches this observation where a heat flux variation of ~ 0.1 MW/m² is reported by Lopez with increasing heat flux during NST.

Figure 4.22 shows the vertical heat flux profile at different times during the fifth oscillation cycle for the Badri Case. The peak heat flux location is almost constant at 8 mm below the meniscus (far-field steel/slag interface), where the gap resistance is smallest. Large local increases in air gap profile (below this location) and slag thickness (above this location) both cause increased gap resistance that causes the heat flux peak to manifest in this location. The variation of heat flux profile with time 0.5 (0.7 to 1.2) MW/m² corresponds to interface oscillation as discussed earlier in section 4.3. This compares reasonably with the large heat-flux range calculated in this region with a 2D inverse model^[102] with the thermocouple temperatures measured by Badri.^[66] In a Lagrangian reference frame, however, the current heat flux varies by only 0.05 (0.3 to 0.35) MW/m², as shown on Figure 4.17. The heat flux measured by Badri's 1-D inverse model in this region exhibits large low-frequency variations in addition to high-frequency variations^[97] due to oscillation of ~ 0.06 (0.19 to 0.25) MW/m². These variations agree well, and are greatly decreased with the Lagrangian frame.

Figure 4.23 shows the corresponding vertical heat flux profile for the Shin case. In this case, the peak heat flux is less variable during the oscillation cycle because there are no large changes in

air gap profile so gap resistance near the meniscus is more uniform. However, the heat flux peak moves spatially with the mold, according to the interface height variations that accompany the oscillation stroke. In addition, more temporal variation in heat flux is observed below the mold, which corresponds to variations in the gap thickness further down the mold. This heat flux profile and its variations generally match observations in real casters.^[10, 41, 43]

4.8 Figures:

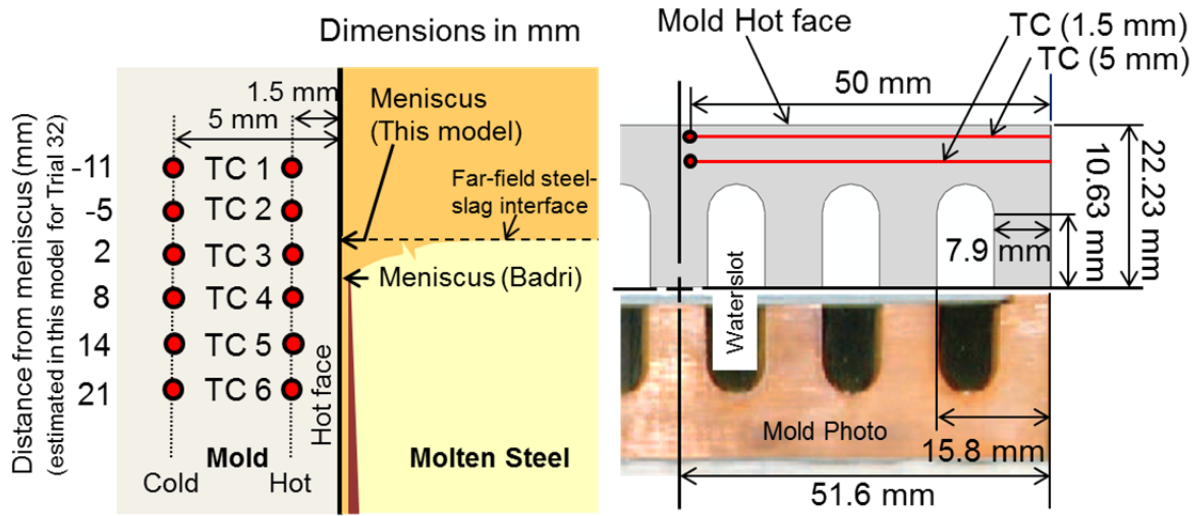


Figure 4.1: Badri experiment thermocouple locations (left) and mold dimensions (right).

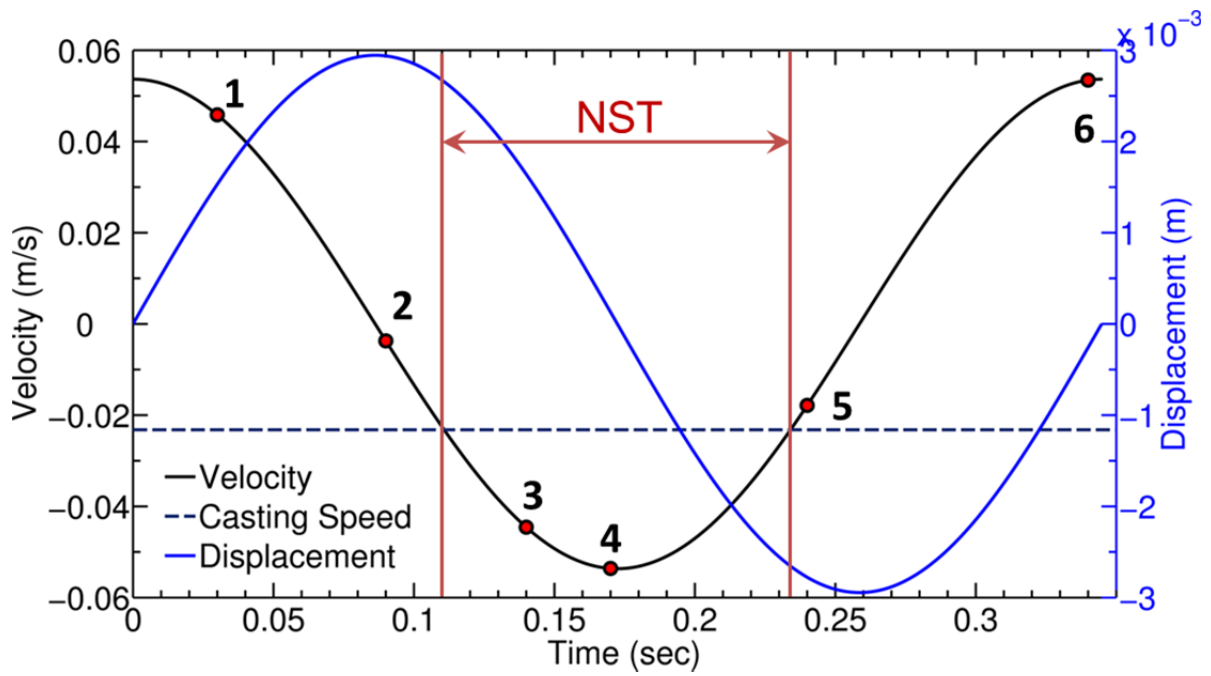


Figure 4.2: Displacement, Velocity and NST time over one oscillation (0.77-1.12 s) for Shin case.

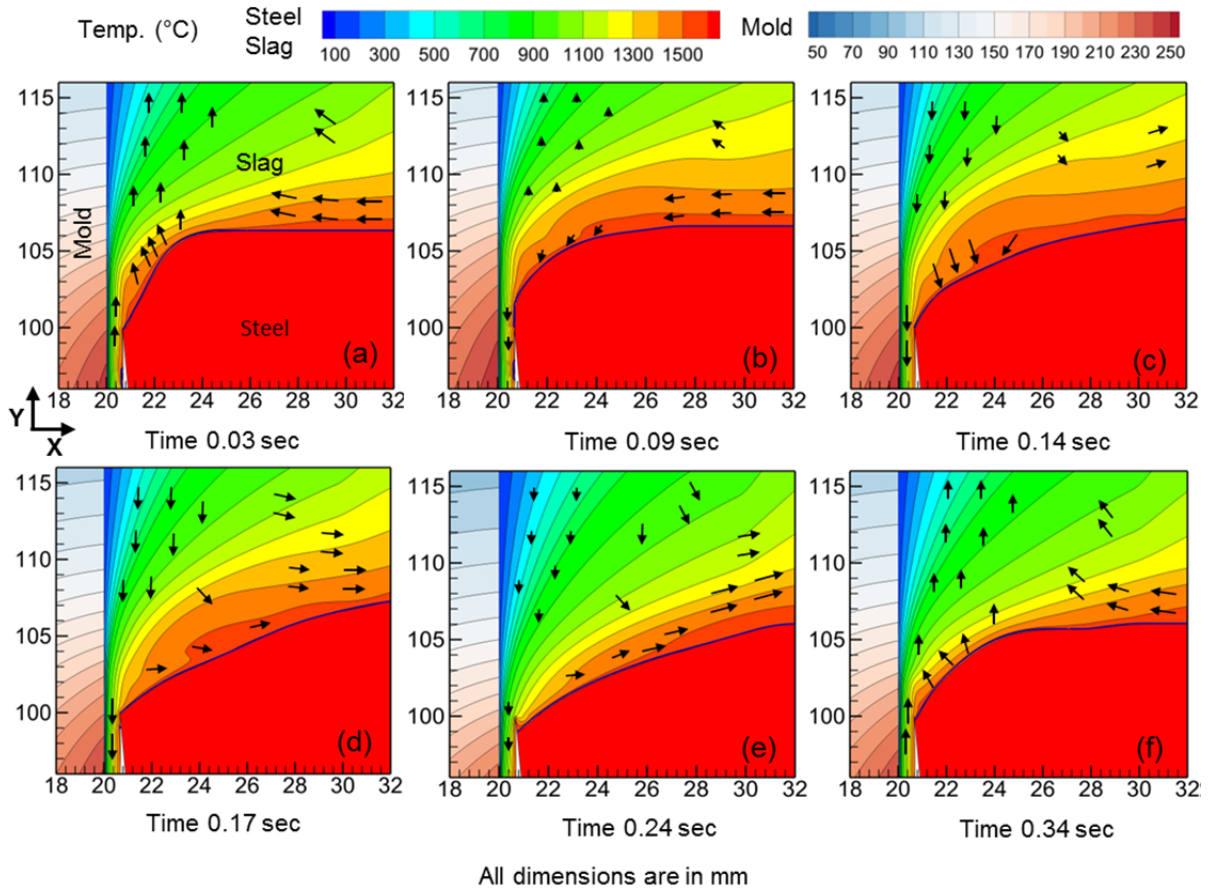


Figure 4.3: Meniscus region events over one oscillation (0.77-1.12 s) for Shin Case.

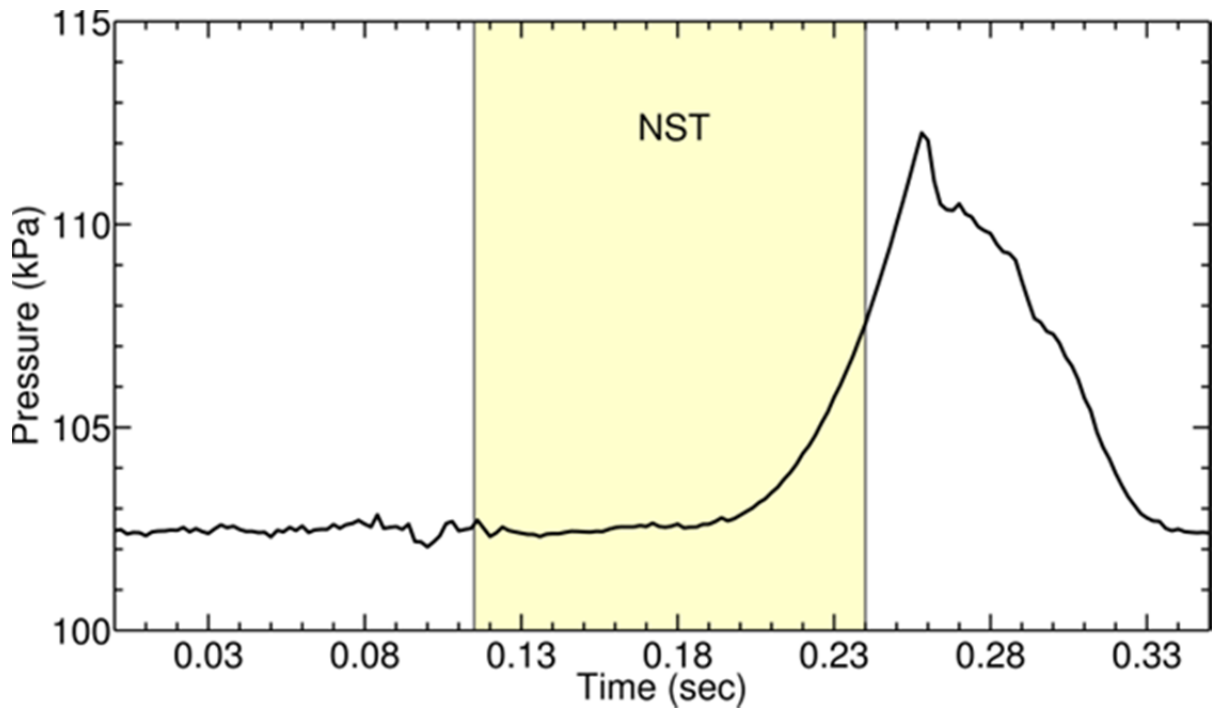


Figure 4.4: Predicted slag pressure at 0.4 mm from hot face and 0.5 mm above shell tip (Shin case: 0.77-1.12 s).

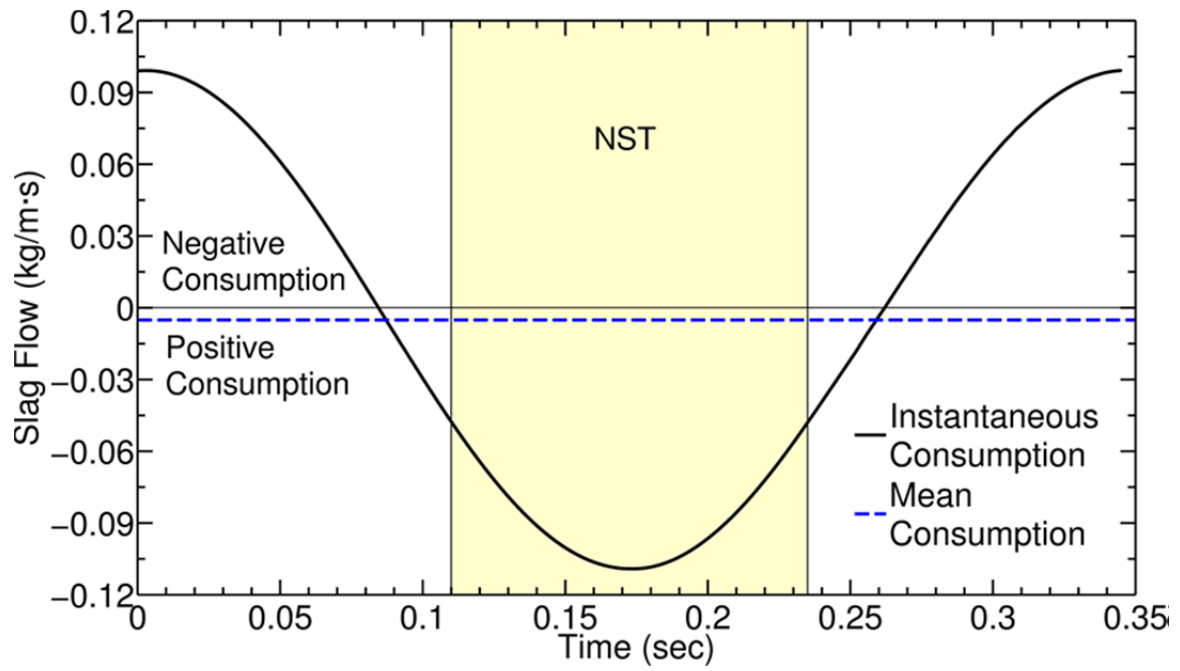


Figure 4.5: Predicted instantaneous and mean slag consumption for Shin case (0.77-1.12 s).

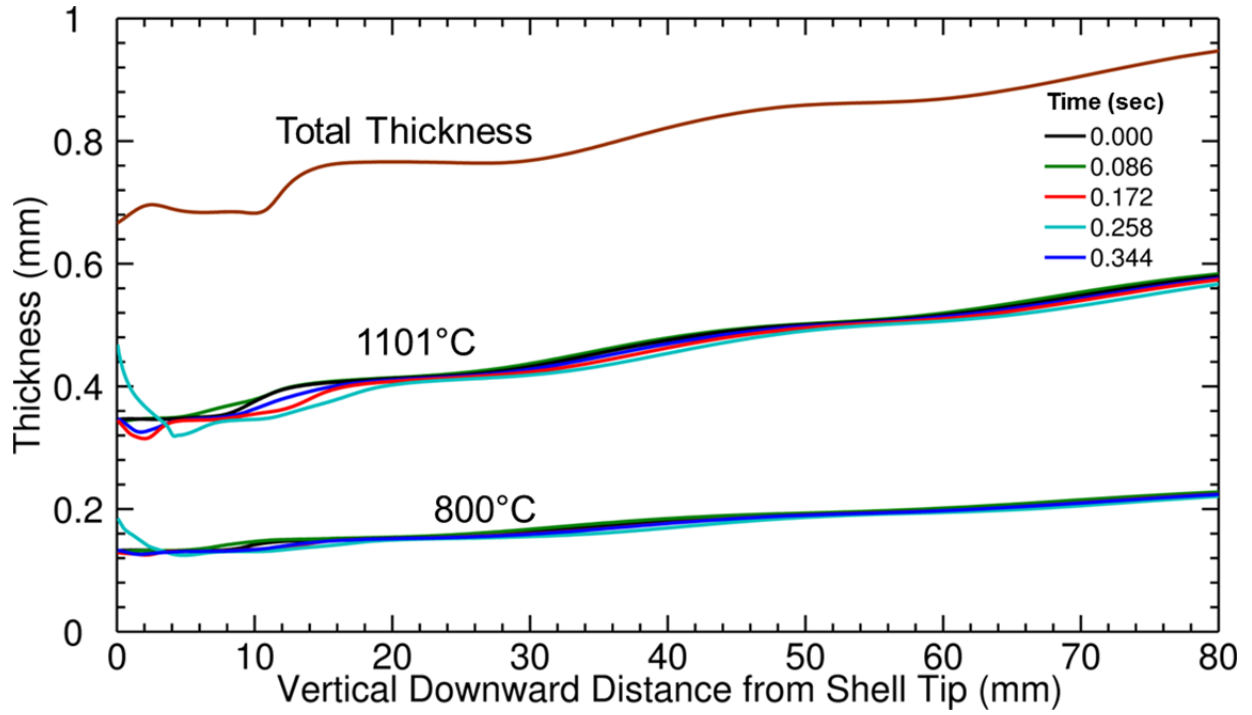


Figure 4.6: Liquid slag thickness predicted by model based on 1101°C and 800°C constant temperature line (Shin Case: 0.77-1.12 s).

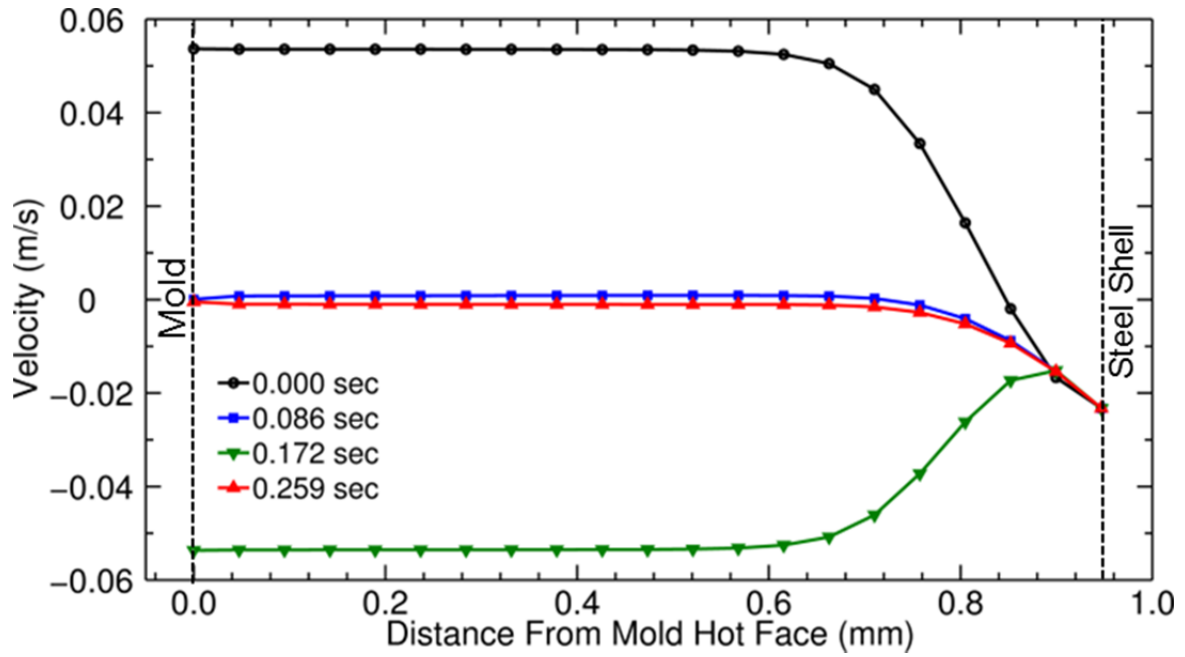


Figure 4.7: Transient velocity in the slag gap (Shin Case: 0.77-1.12 s).

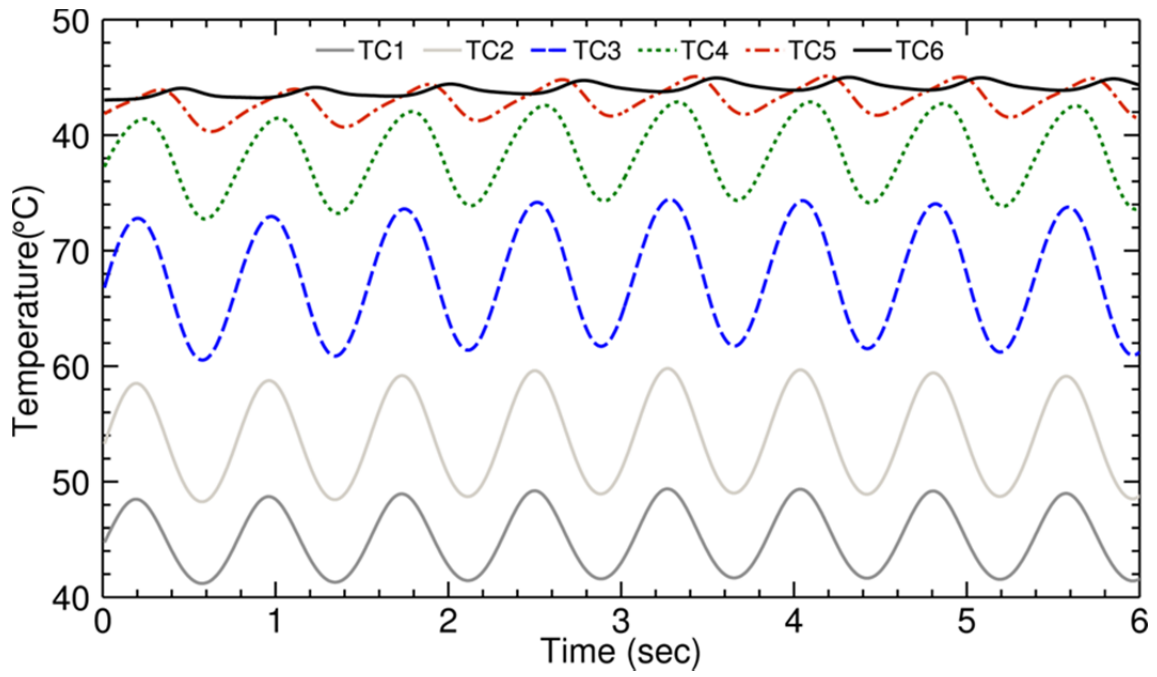


Figure 4.8: Temperature predictions at TC (hot) locations over simulation time (Badri case: fixed in lab frame of reference).

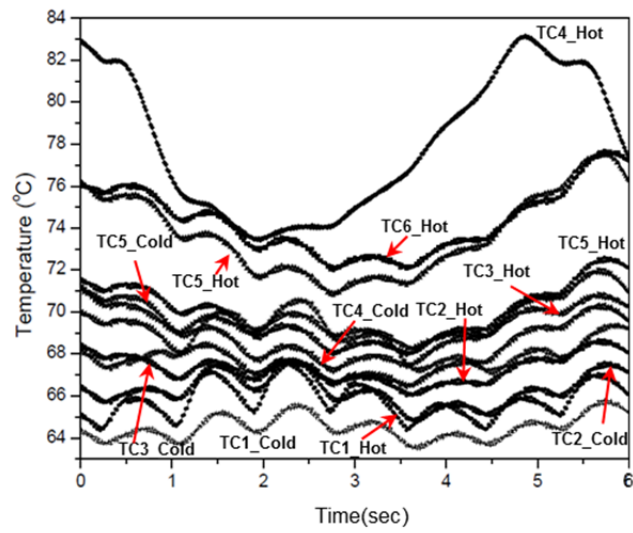


Figure 4.9: Measured temperatures in Trial 32 reported by Badri.^[97]

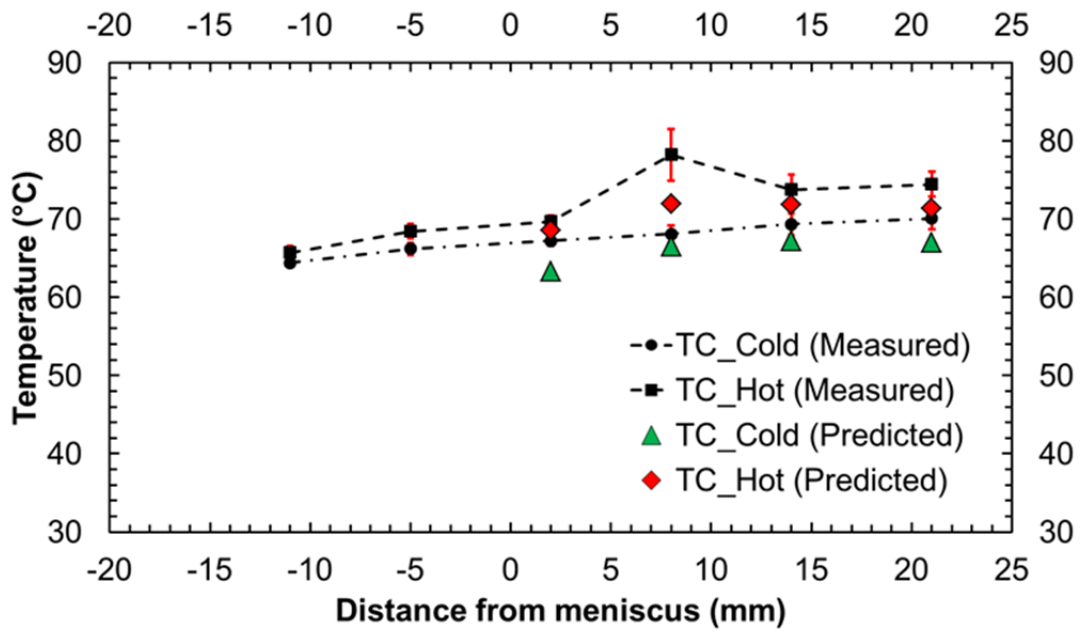


Figure 4.10: Model averaged thermocouple predictions Vs. measured values by Badri averaged over six oscillation cycles (error bars indicate the range).

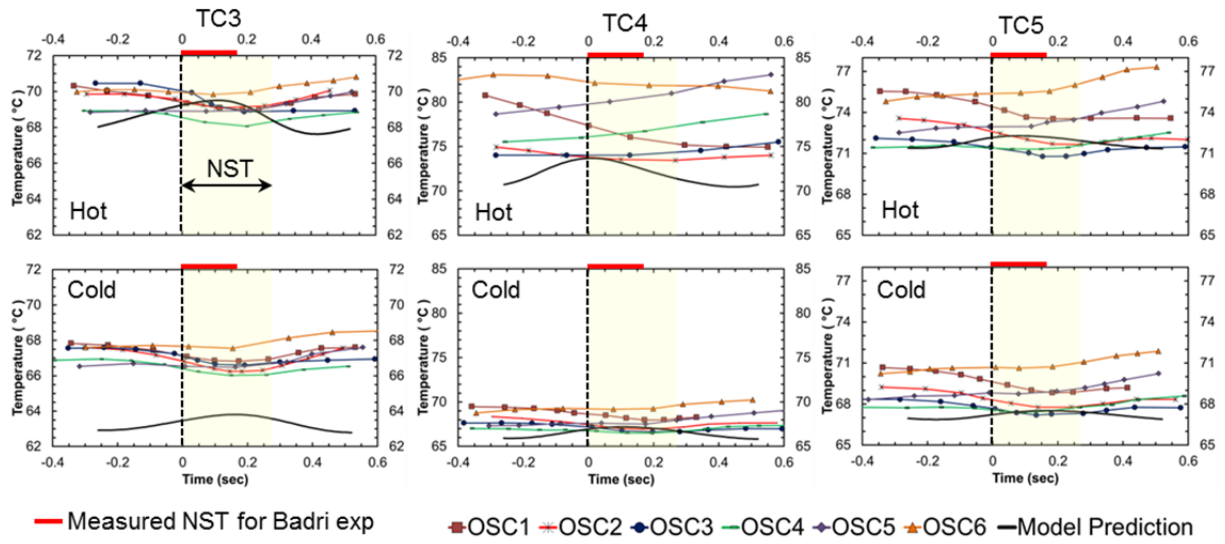


Figure 4.11: Thermocouple prediction by model Vs. measured temperatures by Badri (Thermocouples fixed in mold).

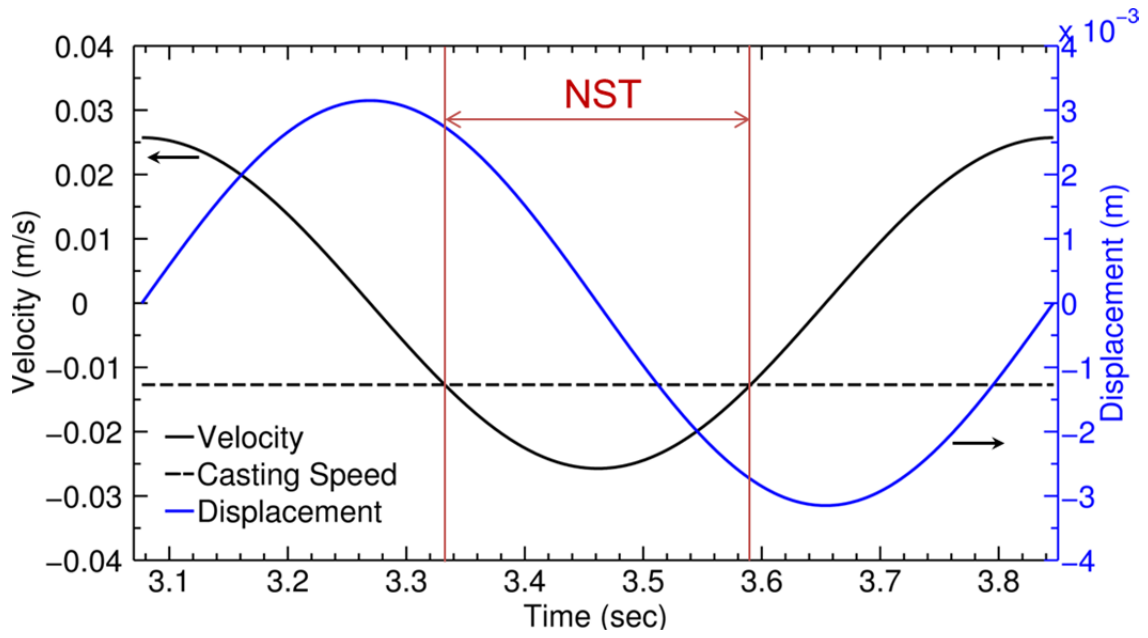


Figure 4.12: Displacement, Velocity and NST time over one oscillation cycle for Badri experiment.

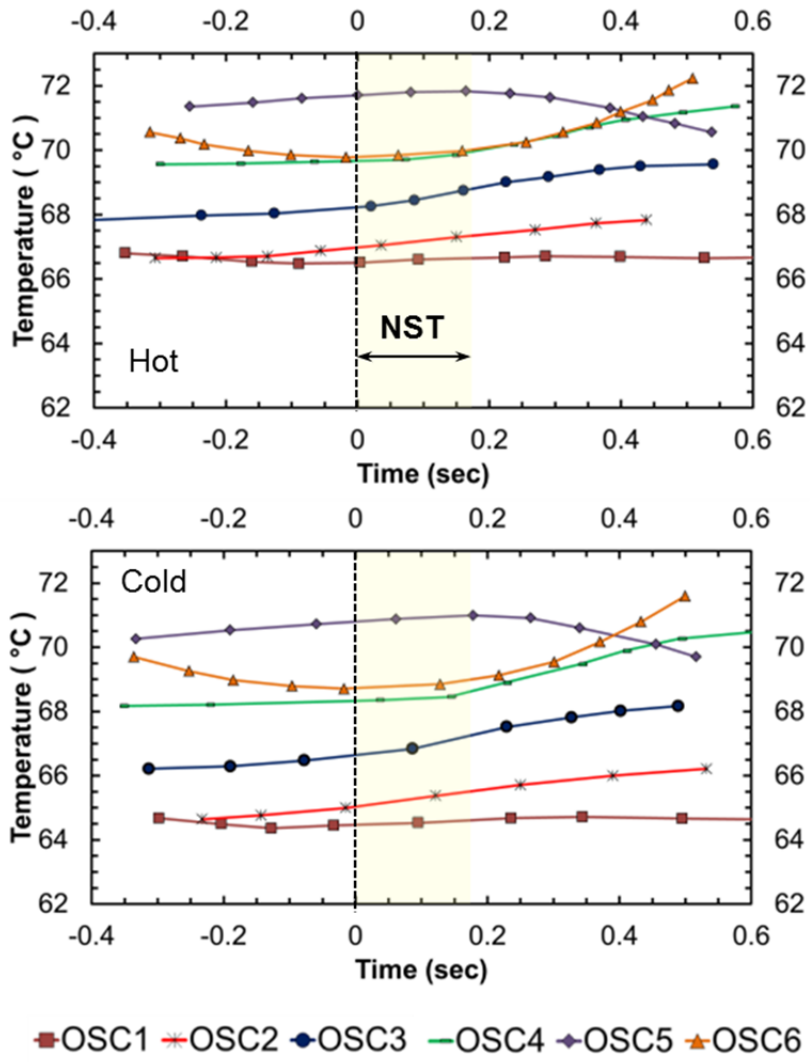


Figure 4.13: Badri^[97] thermocouple measurements for Trial 31.

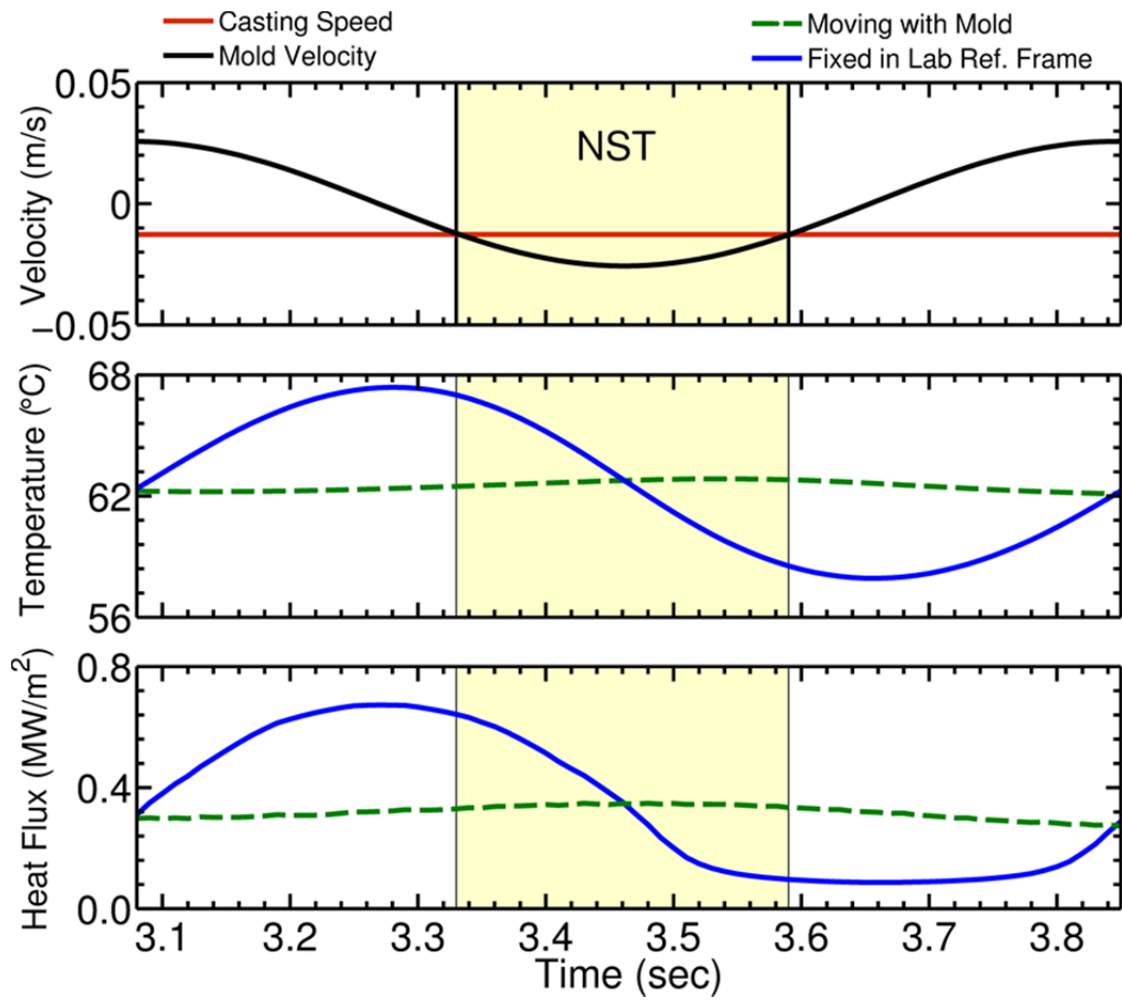


Figure 4.14: Comparison between temperature and heat flux predictions at TC3 (hot) location for reference frames fixed in the lab (Eulerian) and mold (Lagrangian) (Badri case).

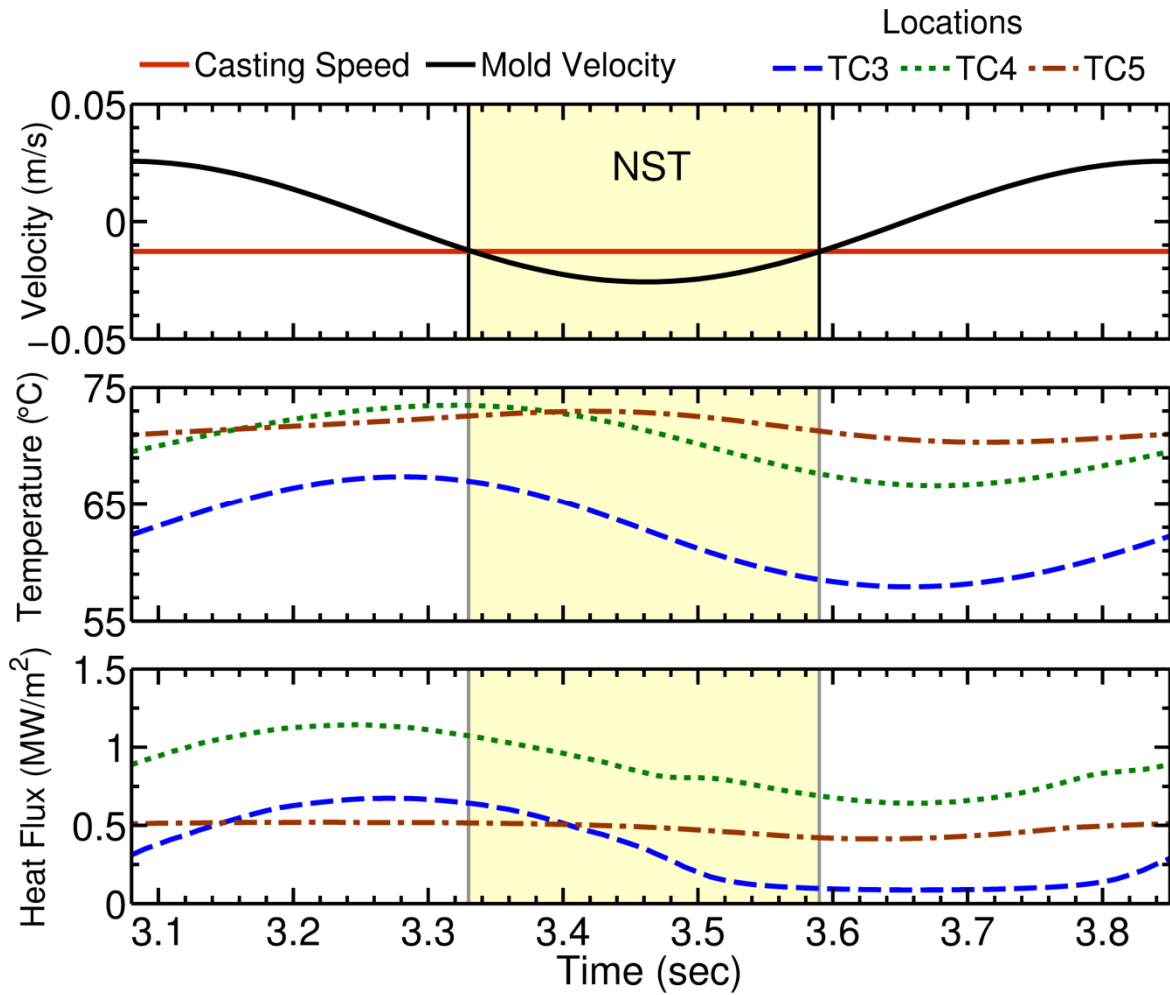


Figure 4.15: Temperature and heat flux predictions at TC3-TC5 (hot) locations using lab reference frame (Badri case).

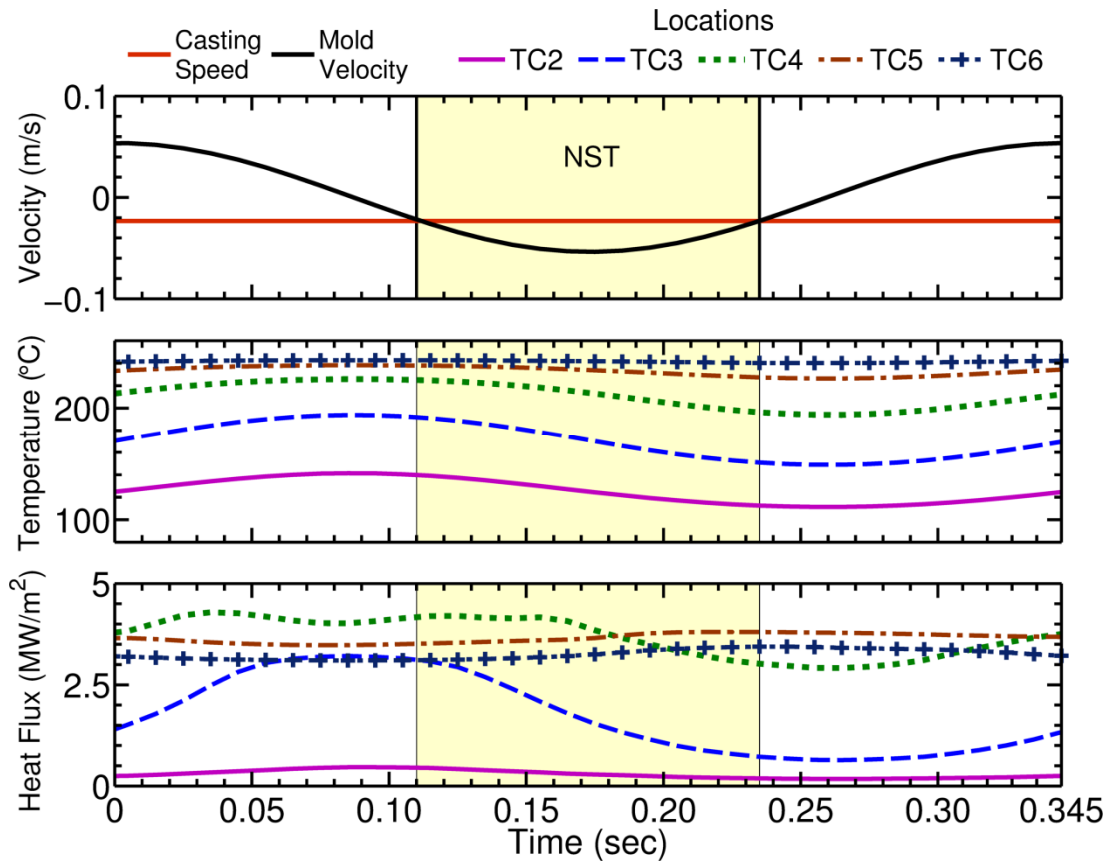


Figure 4.16: Temperature and heat flux predictions at TC2-TC6 (hot) locations using lab reference frame (Shin case: 0.77-1.12 s).

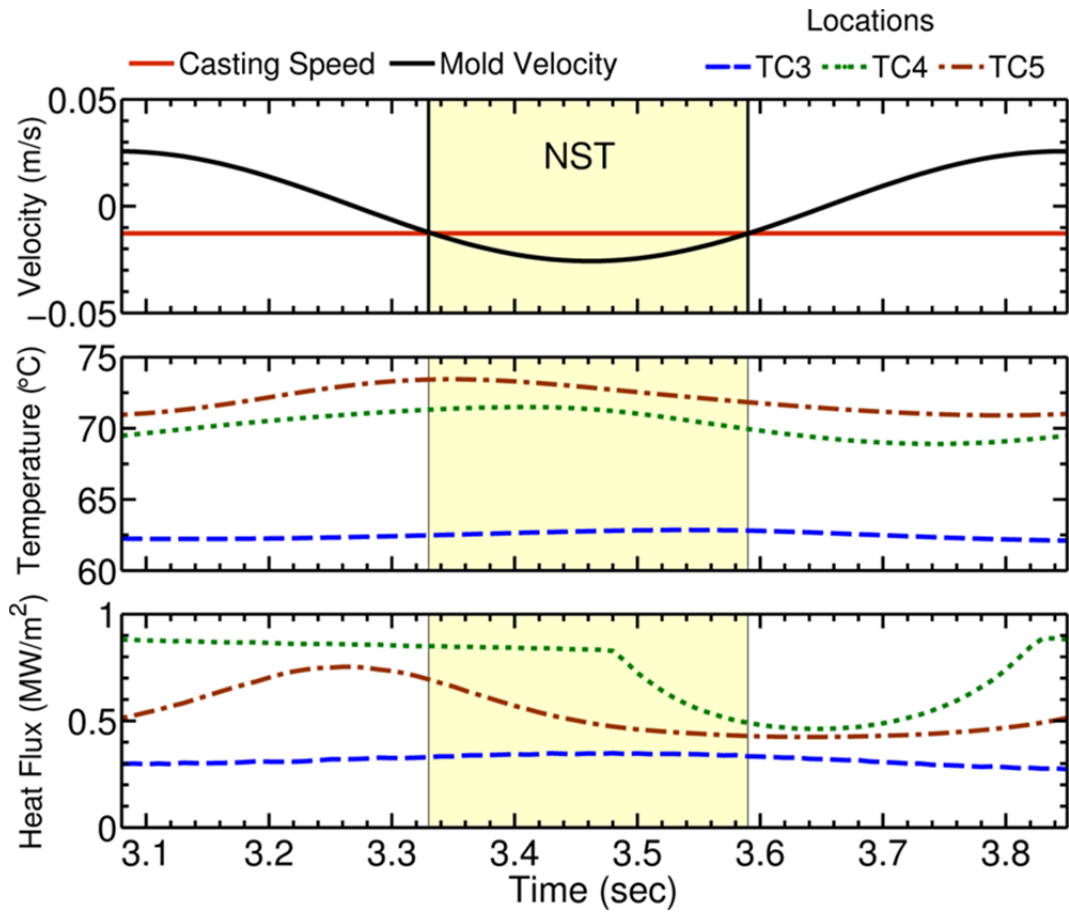


Figure 4.17: Temperature and heat flux predictions at TC3-TC6 (hot) locations using mold reference frame (Badri case).

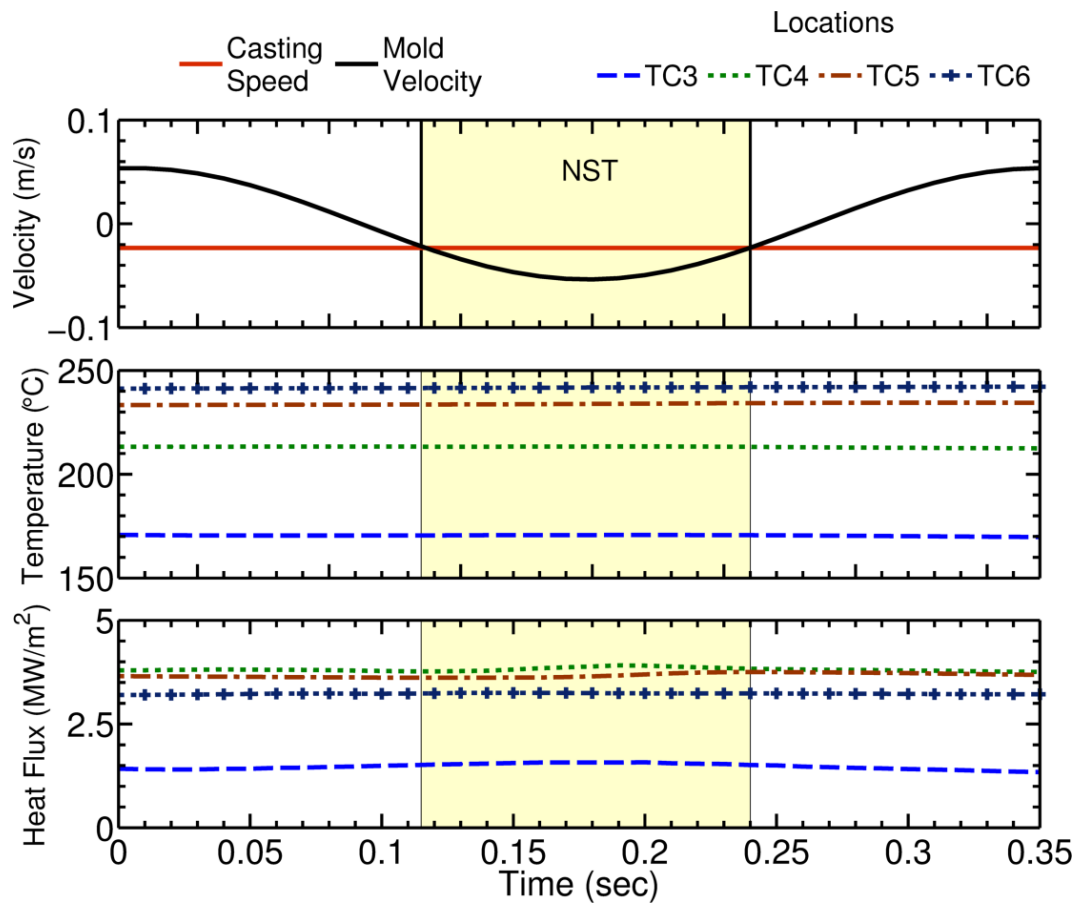


Figure 4.18: Temperature and heat flux predictions at TC2-TC6 (hot) location using mold reference frame (Shin case: 0.77-1.12 s).

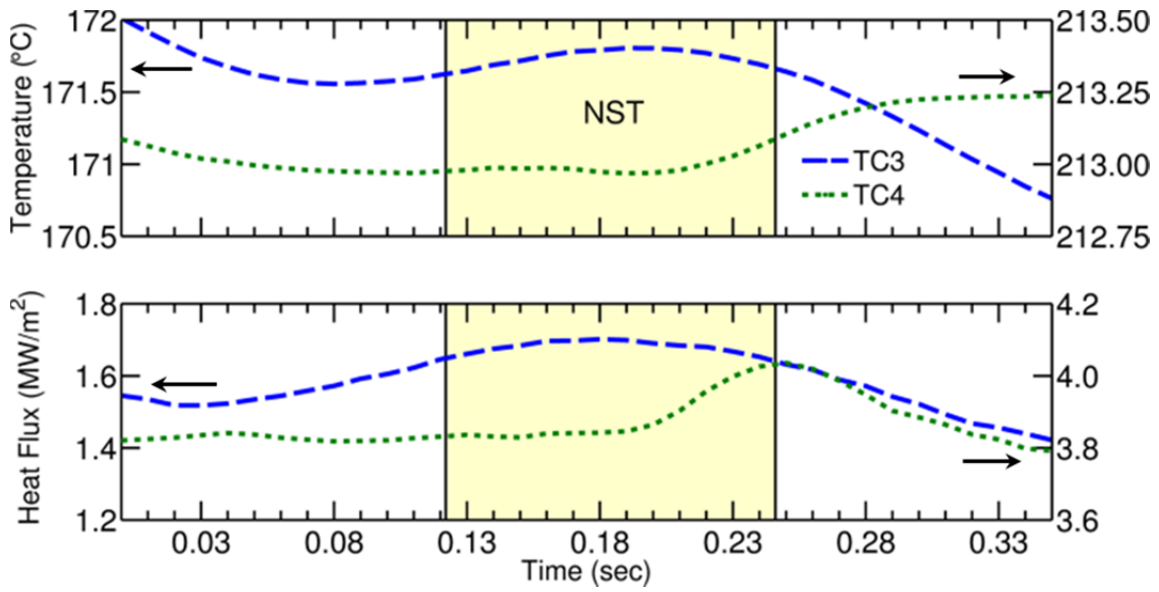


Figure 4.19: Temperature and heat flux predictions at TC3-4 (hot) locations using mold reference frame (Shin case: 0.43-0.77 s).

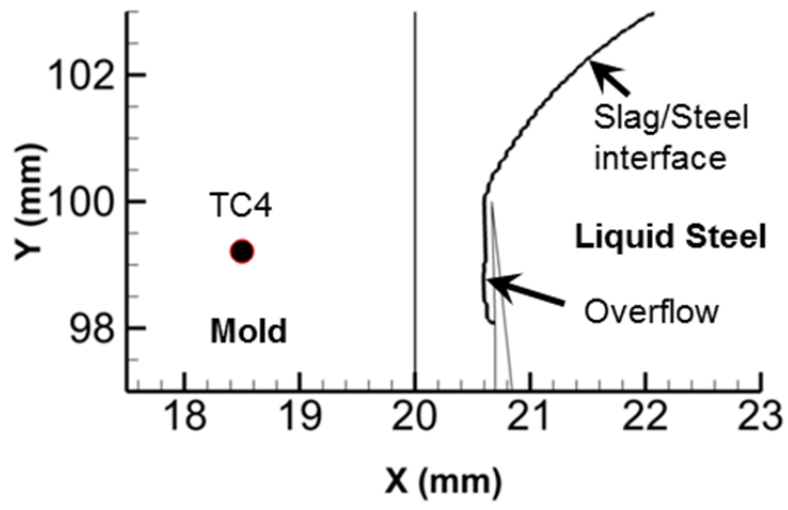


Figure 4.20: Overflow event in Shin Case (0.59 s).

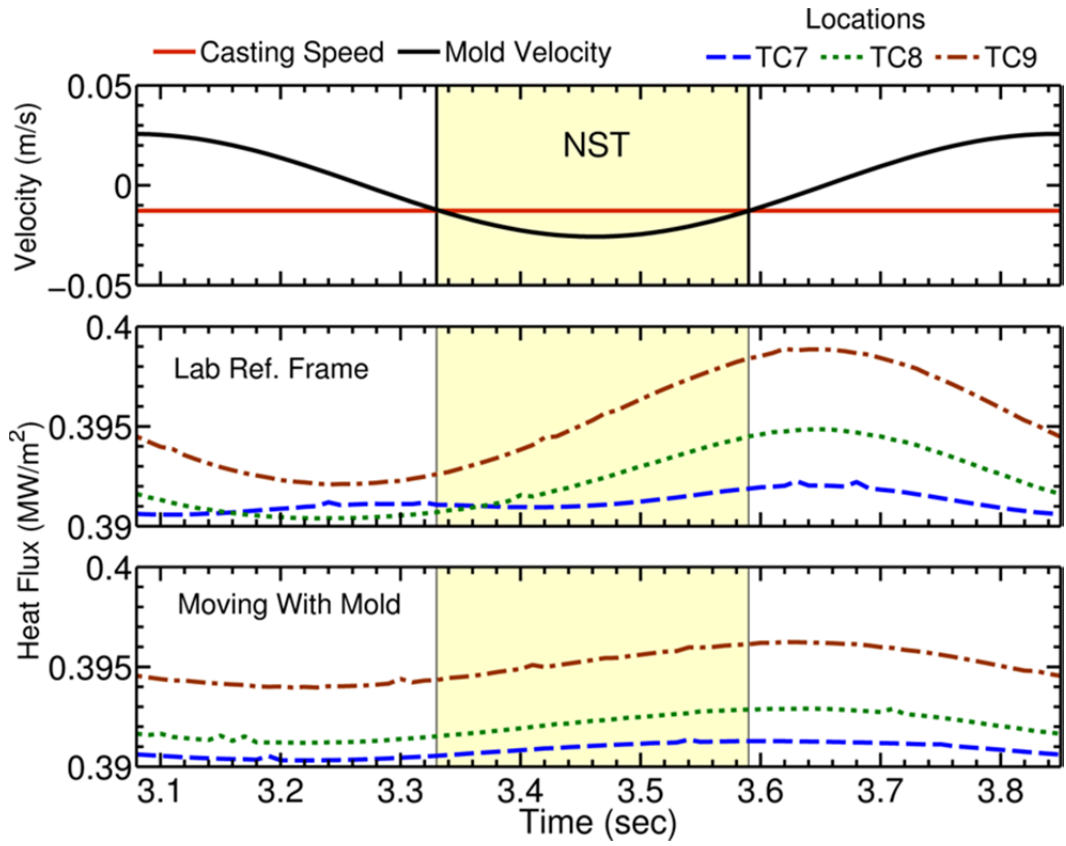


Figure 4.21: Heat flux predictions at the region 45 mm below meniscus (Badri case).

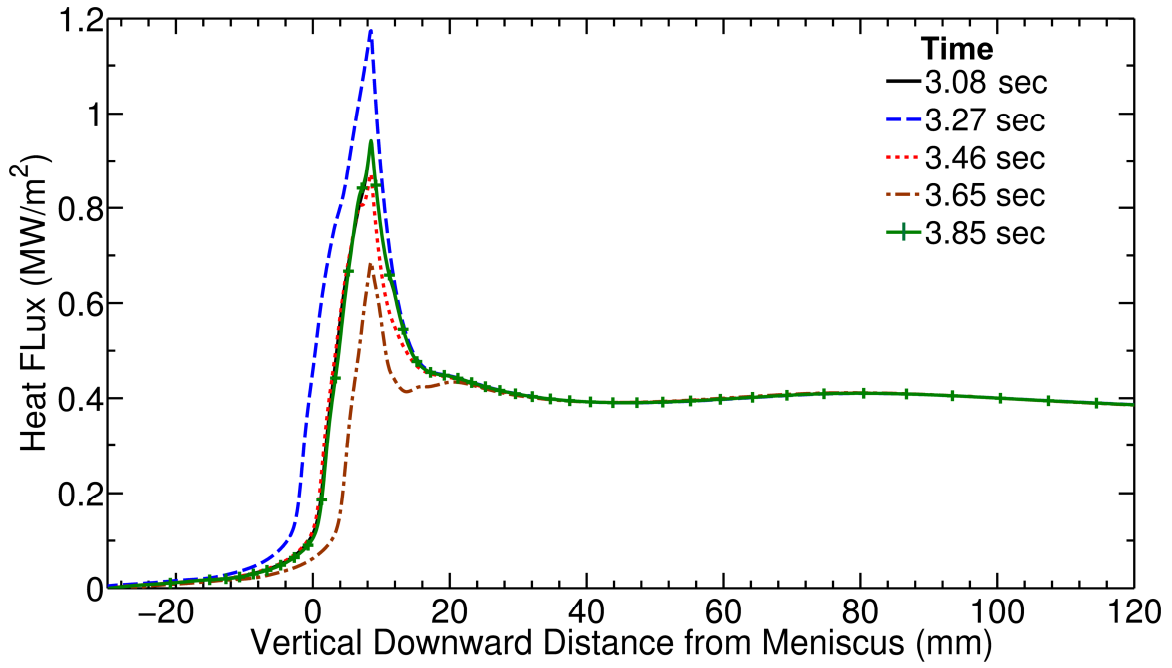


Figure 4.22: Predicted transient heat flux profile over one oscillation (Badri case).

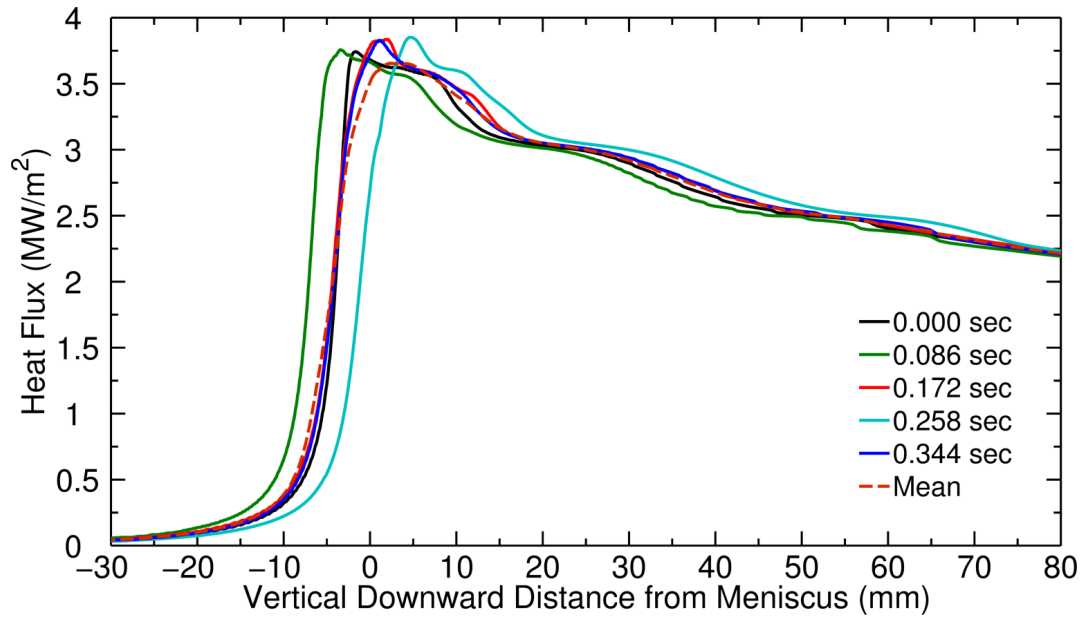


Figure 4.23: Predicted transient heat flux profile over an oscillation cycle (Shin case: 0.43-0.77 s).

CHAPTER 5: PARAMETRIC STUDIES

The validated computational model developed in this work was simplified to increase computational efficiency by dropping the mold and solid slag regions, as done by Ojeda^[58-59]. The simplified model was then applied in a parametric study to predict slag consumption as a function of different casting variables.

5.1 Simplified Model Development:

In a real casting mold, the solidified slag layer fractures periodically^[103] causing effective downward movement at some fraction of the casting speed^[41]. Near the meniscus region modeled in this work, however, it is safe to assume that the solid slag moves with the mold (see Figure 4.7). Thus, the solid slag does not contribute to consumption in the current model. Accordingly, the left domain wall was truncated at the solid/liquid interface, by oscillating with the mold, and setting the boundary temperature to 800°C below the meniscus (from 14 mm above the far-field slag/steel interface to end of domain), to make the viscosity high enough ($\sim 10^4$ Pa·s) to behave as a solid. Above the meniscus (14 mm above the far-field slag/steel interface), heat flux was set to zero. Different low values of heat flux above the meniscus were investigated and found to have no significant effect.

The gap size for the liquid slag thickness was chosen to match the results of the Shin case, which is observed in Figure 4.6 to be ~ 0.6 mm at the solidification temperature of 800°C. The variable cold side shell surface temperature was fixed at $\sim 1521^\circ\text{C}$, which lowered the viscosity and consequently increased mass flow (Appendix B, Figure B.5). To balance this effect, the gap size was reduced to 0.5 mm to match the slag consumption of the Shin case. Most of the domain is modeled with the properties of melting slag. The 10 mm wide region next to the 800°C left wall

was given solidification properties. After a mesh independence study, a mesh of 5,340 cells was chosen for this model.

5.2 Simplified Model Validation:

The simplified model was first applied to 4 different sets of casting conditions (Table 5.1) with available consumption measurements from POSCO trials in 2002 and 2003 from Shin.^[67] Figure 5.1 compares the varying slag consumptions for the 4 cases during a typical oscillation cycle.

The predicted and measured consumptions are compared in Table 5.1, and agree within 11%. This error seems reasonable, considering the uncertainty in measuring bags of powder, and the model assumptions of constant gap size (0.5 mm) and neglect of the oscillation mark shape on consumption.

5.3 Casting Conditions for Parametric Studies:

To study the effects of casting speed, stroke, frequency and modification ratio on slag consumption, 4 sets of simulations were conducted, (16 cases total) for conditions given in Table 5.2. In each set of cases, (C, S, F, and M) one parameter is changed while others are kept constant. Mold slag consumption (kg/min or bags per hour), is quantified in three different ways: 1) a total rate of mass per unit time per unit length of strand perimeter ($\text{g/m}\cdot\text{s}$), 2) mass per oscillation cycle per unit length of strand perimeter ($\text{g/m}\cdot\text{cycle}$), or 3) mass per unit area of strand surface (kg/m^2). The latter correlates best with liquid layer thickness in the gap and lubrication in practice, so is reported here unless specified otherwise. Conversion between the units are given in APPENDIX C.2.

5.4 Results:

5.4.1 Casting Speed (v_c):

The predicted mean slag consumption (kg/m^2) decreases slightly with increasing casting speed, as shown in Table 5.2, Case C1-3 and in Figure 5.2(a). Specifically, an 8.6% increase in casting speed (from 23.3 to 25.3 mm/s) causes the slag consumption rate (kg/min or $\text{g/m}\cdot\text{cycle}$) to increase by only 7.5%, which corresponds to a decrease in slag consumption of 1%. This relationship is well documented in previous measurements,^[19-20, 48, 104] including casters with both sinusoidal and non-sinusoidal oscillation.^[47]

5.4.2 Stroke (s):

Based on Case S1-3 in Table 5.2, Figure 5.2(a) shows that consumption (kg/m^2) increases slightly with increase of stroke. Increasing stroke by 40% increases consumption by only 2%, however, this agrees with previous measurements, such as quantified with the empirical equation of Tsutsumi et al.,^[47]

$$Q_{area} = \frac{k_{\beta}}{T_{cs}\sqrt{\mu}} \frac{s^{0.4}}{v_c} \cos^{-1}\left(-\frac{1000 \times v_c}{2\pi fs}\right) \quad (5.1)$$

where, Q_{area} is slag consumption per unit strand area (kg/m^2), v_c is casting speed (m/min), f is frequency (cpm), s is stroke (mm), μ is viscosity at 1300°C (P), T_{cs} is crystallization temperature ($^{\circ}\text{C}$) and k_{β} is constant. In Eqn. 5.1, stroke appears in two places with opposite effects. The net effect of increasing stroke is a slight increase of all 3 measures of consumption: ($\text{g/m}\cdot\text{s}$, $\text{g/m}\cdot\text{cycle}$, and kg/m^2).

5.4.3 Frequency (f):

Two sets of simulations with two different strokes (F1-4, F2-1-3) were done to study the effect of changing frequency. Frequency has small inconsistent effect on slag consumption (kg/m^2) as

shown in Figure 5.3(a). Increasing frequency by ~62% causes only 1% to 2% variation (both decrease and increase) although it decreases slag consumption per cycle (g/m·cycle) by ~35%, as shown in Figure 5.3(b) for both F1-4 and F2-1-3. This agrees with empirical equations by many researchers^[47, 53, 105-106] as reviewed by Saraswat et al.^[107] that show both increasing and decreasing slag consumption per unit area. The inverse relationship with consumption per cycle (g/m·cycle) agrees with Shin's^[19] equation.

5.4.4 Modification Ratio (α_m):

The effect of non-sinusoidal oscillation was investigated with two casting conditions (M2-3) using 12% and 24% modification ratio (α_m) which is defined after Eqn. 3.20. Increasing α_m to 24% is predicted to increase slag consumption by ~2.4%, as shown in Figure 5.2(b). This trend agrees quantitatively with many previous measurements.^[4, 67] Tsutsumi et al.,^[47] measured over 50% higher consumption and explained this trend is due to the increase in PST that accompanies the increase of α_m . Suzuki et al.^[4] reported that this trend is due to decreasing frictional force. Finally, the relative speed of the mold to the solidified shell is higher during NST with non-sinusoidal oscillation.

5.4.5 Positive Strip Time (PST, t_p):

To combine the effect of all four independent variables (casting speed, frequency, modification ratio and stroke) into one variable a lot researchers^[4, 19, 47, 108-109] suggested using PST (t_p) and found a strong increasing co-relation slag consumption per unit length per cycle with increasing t_p . In this study all 16 simulations are shown in terms of t_p in Figure 5.4 and it shows the similar increasing trend expected based on literature review. Measured values of slag consumption by Shin^[19] for different casting conditions and computed values based on his empirical equation are presented in the same figure. A very good match is observed in terms t_p .

5.4.6 Negative Strip Time (NST, t_n):

Similar to PST, the other popular indicator proposed by researchers is NST (t_n). Some researchers^[8, 110-111] reported that the slag consumption per unit length per cycle increases proportional to NST. Figure 5.5 shows the prediction slag consumption vs NST for Cases C1-M3. Although an increasing trend is observed and both measured and predicted values by Shin^[19] also show the increasing behavior for different casting conditions, it is not as prominent as the relation with t_p .

Further improvement can be done to this model by better modeling the temperature properties of the slag and steel. Instead of leaving the steel shell out of the computational zone, its growth can be modeled using a source based method for solidification phase change developed by Voller^[112] which has already been validated using Stefan problem. Another key improvement can be made by using temperature history to define solidification and melting zone for slag instead of spatially fixing them.

5.5 Figures:

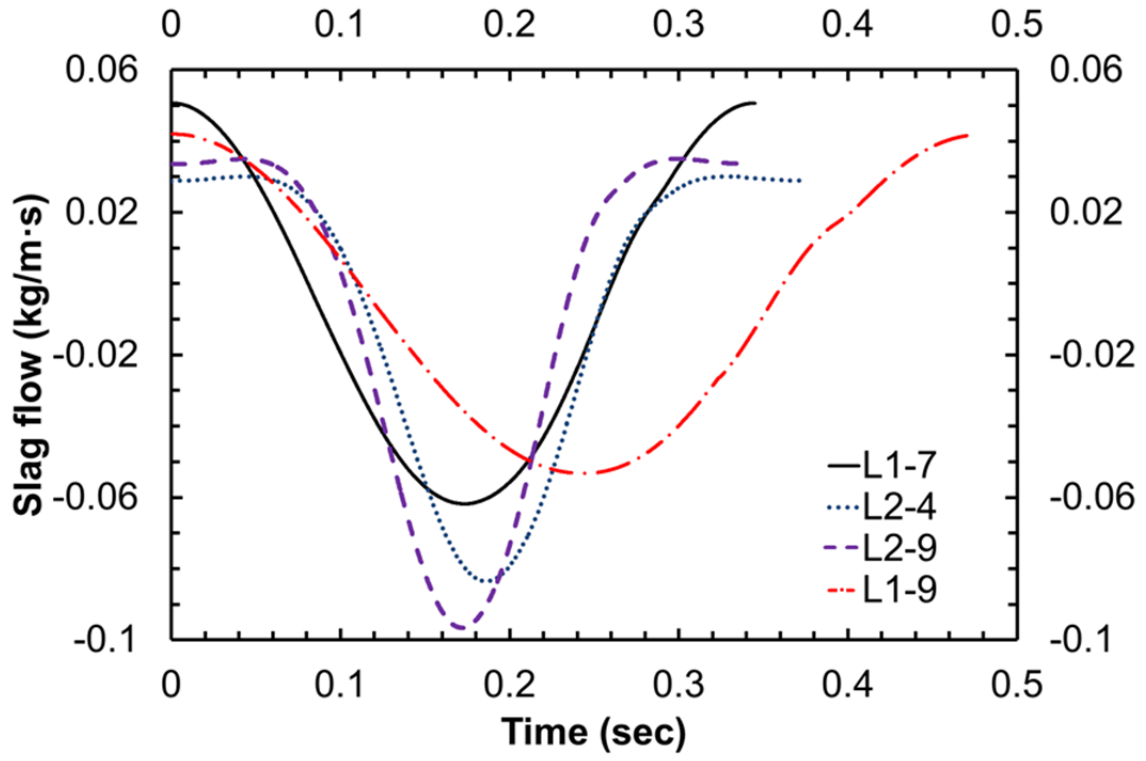


Figure 5.1: Predicated transient slag consumption for slag consumption validation cases.

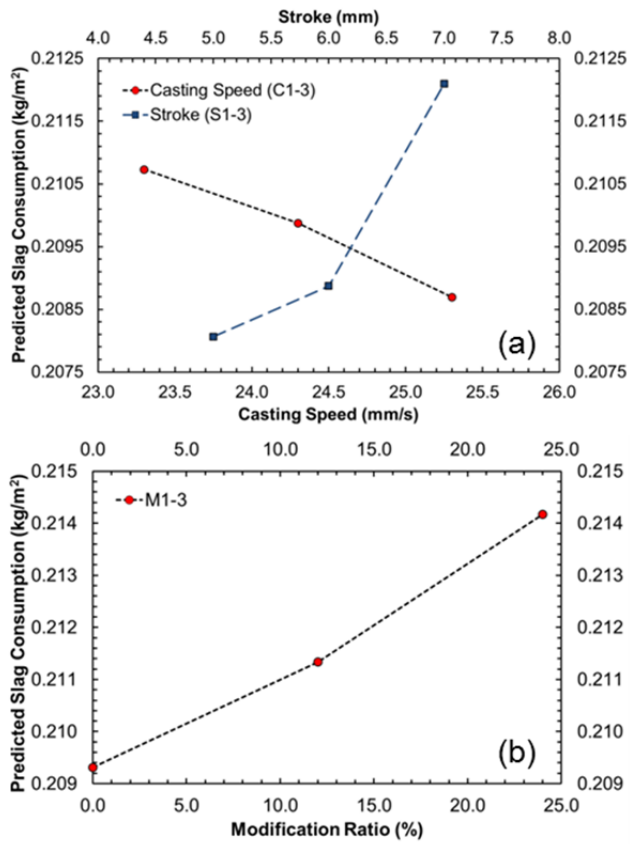


Figure 5.2: Predicted effect of changing casting speed, stroke and modification ratio on slag consumption.

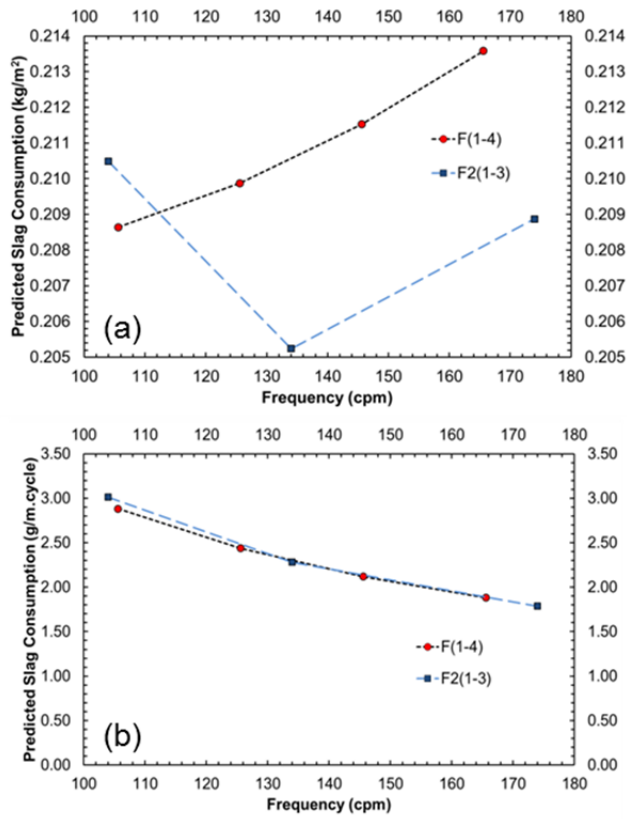


Figure 5.3: Predicted effect of changing frequency on slag consumption.

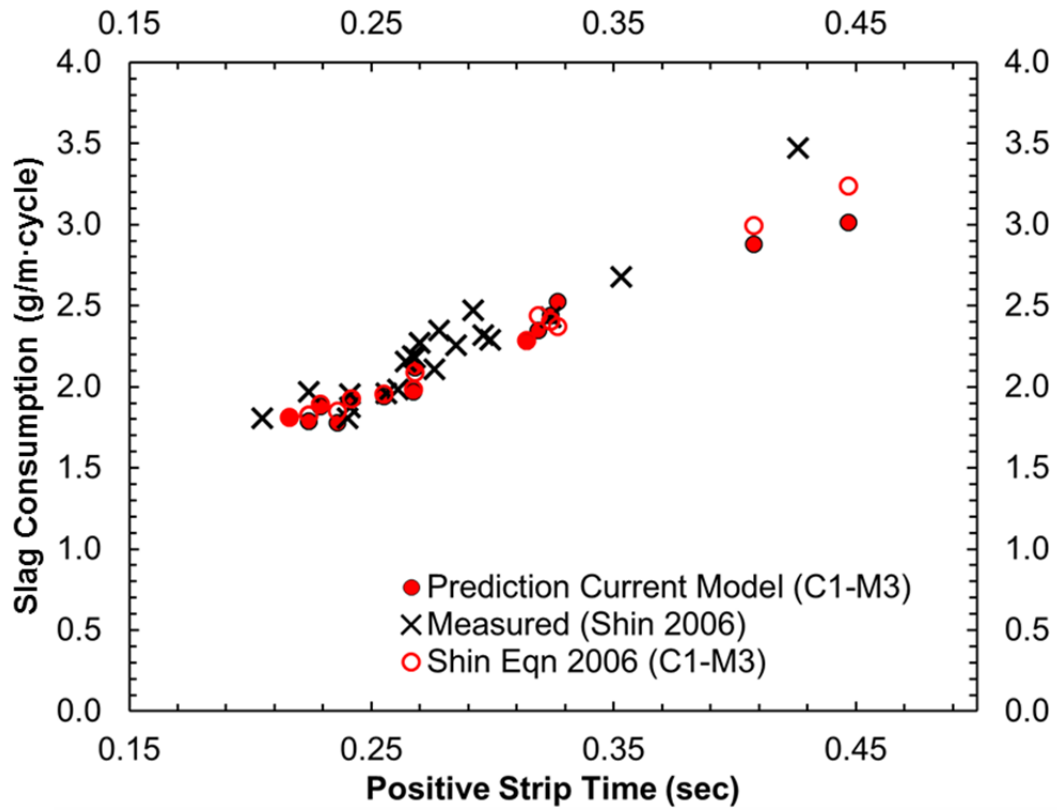


Figure 5.4: Predicted and measured^[76] slag consumption Vs. Positive Strip Time.

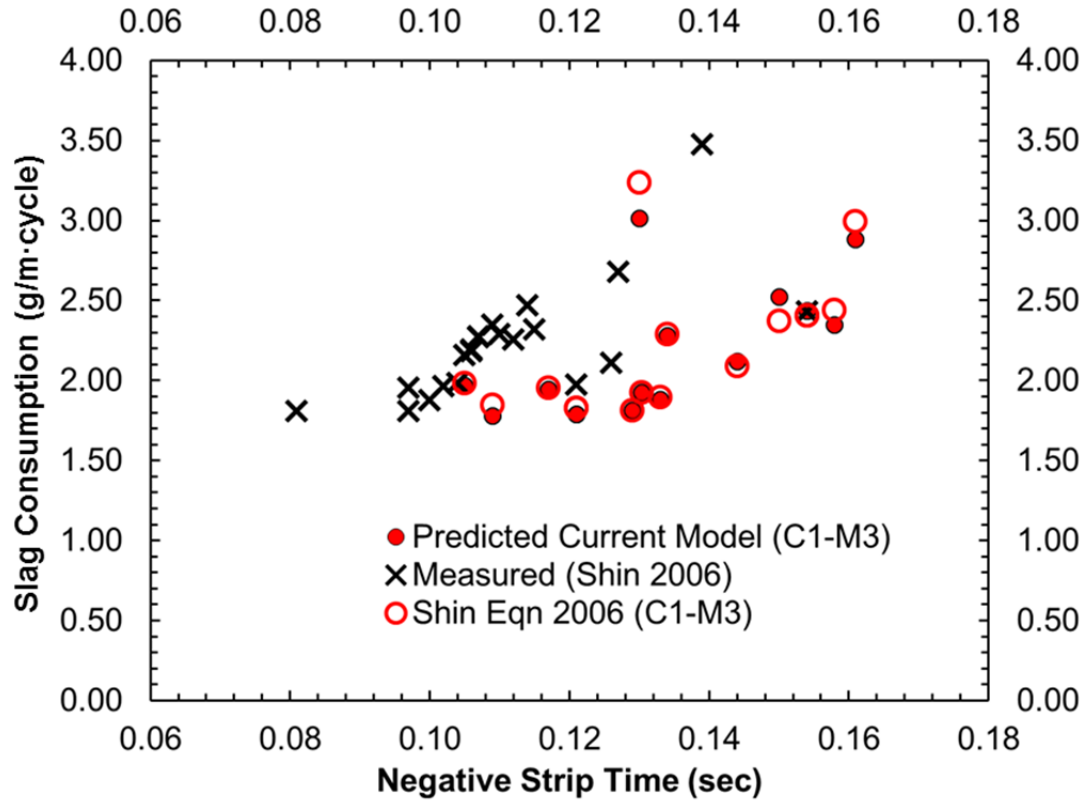


Figure 5.5: Predicted and measured^[76] slag consumption Vs. Negative Strip Time.

5.6 Tables:

Table 5.1: Casting conditions, measured and predicted slag consumption for validation cases.

Case	Slab Width	Casting Speed	Stroke	Frequency	α_m^*	Strip Time		Slag Consumption				Error
						NST	PST	Measured	Predicted			
	mm	m/min	mm	cpm	%	s	s	kg/m ²	g/m·s	kg/m ²	g/m·cycle	%
L1-7	1300	1.490	6.00	174.0	0	0.121	0.224	0.230	5.2001	0.2094	1.7931	-8.96
L1-9	1300	1.466	7.00	125.6	0	0.154	0.324	0.208	5.0992	0.2087	2.4363	0.35
L2-4	1300	1.484	6.47	161.2	24	0.106	0.267	0.238	5.3004	0.2143	1.9727	-9.96
L2-9	1050	1.660	6.77	178.3	24	0.097	0.240	0.194	6.0009	0.2169	2.0191	11.79

* α_m = Modification ratio

Table 5.2: Casting conditions, measured and predicted slag consumption for parametric study cases.

Case	Casting Speed	Stroke	Frequency	α_m^*	Strip Time		Predicted slag consumption		
					Negative	Positive			
	mm/s	mm	cpm	%	s	s	g/m·s	kg/m ²	g/m·cycle
C-1	23.30	7.00	125.6	0	0.158	0.319	4.91	0.211	2.345
C-2	24.30	7.00	125.6	0	0.154	0.324	5.10	0.210	2.437
C-3	25.30	7.00	125.6	0	0.150	0.327	5.28	0.209	2.522
S-1	24.80	5.00	174.0	0	0.109	0.236	5.16	0.208	1.780
S-2	24.80	6.00	174.0	0	0.121	0.224	5.18	0.209	1.786
S-3	24.80	7.00	174.0	0	0.129	0.216	5.26	0.212	1.814
F-1	24.30	7.00	105.6	0	0.161	0.408	5.07	0.209	2.880
F-2	24.30	7.00	125.6	0	0.154	0.324	5.10	0.210	2.437
F-3	24.30	7.00	145.6	0	0.144	0.268	5.14	0.212	2.118
F-4	24.30	7.00	165.6	0	0.133	0.229	5.19	0.214	1.881
F2-1	24.80	6.00	104.0	0	0.130	0.447	5.22	0.211	3.012
F2-2	24.80	6.00	134.0	0	0.134	0.314	5.09	0.205	2.279
F2-3	24.80	6.00	174.0	0	0.121	0.224	5.18	0.209	1.786
M-1	24.70	6.47	161.2	0	0.130	0.242	5.17	0.209	1.924
M-2	24.70	6.47	161.2	12	0.117	0.255	5.22	0.211	1.943
M-3	24.70	6.47	161.2	24	0.105	0.267	5.29	0.214	1.969

* α_m =Modification Ratio

CHAPTER 6: CONCLUSIONS

The current work presents a computational model to predict thermal-flow behavior near the meniscus during an oscillation cycle and slag consumption in continuous steel casting. Both time-averaged and transient predictions match reasonably with lab experiments, plant measurements and literature. The following conclusions can be drawn:

1. The slag/liquid-steel interface follows the mold movement closely. The meniscus moves upward during the up stroke and is pushed downward during the down stroke by the slag rim.
2. Variations in mold temperatures and heat flux near the meniscus are higher than far above or below. The variations decrease for higher frequency mold oscillation.
3. Temperatures evolve differently in Eulerian and Lagrangian reference frames. The real mold thermocouples (Lagrangian) experience less variation in temperature ($\sim 1^\circ\text{C}$ near meniscus for commercial caster) than would mold wall locations fixed in space (Eulerian), because their oscillating movement follows the oscillating interface.
4. Overflow greatly affects the temperature/heat flux distribution during a cycle. With no overflow, in the Lagrangian reference frame, the model predicts oscillating heat flux that increases to a maximum during NST for thermocouples near meniscus and shell tip. But, when overflow occurs, the predicted heat flux increases to a maximum near the end of NST, as observed in both the lab experiment and simulations. The transient behavior during a cycle may differ according to when or if overflow occurs, but the time averages should be similar.
5. Below the meniscus region, heat flux tends to decrease with distance down the mold, so during the downstroke (NST) of each cycle, the heat flux tends to decrease.
6. The oscillating mold wall drags slag downward in the gap between the mold hot face and the steel shell mainly during NST. This slag consumption is assisted by the pressure generated

by the oscillating slag rim that pumps liquid slag into the gap at the meniscus near the end of NST.

7. Transient slag consumption prediction closely follows the oscillation velocity of the mold. Part of the time period, slag flows up into the channel and it moves downward in the rest of it. The net result is a constant downward slag flow rate per oscillation cycle. Predicted mean slag consumption matches measurements with in $\pm 11\%$.
8. Increase of casting speed (8.6%) increases slag consumption rate (kg/min or g/m·cycle) (7.5%) which results in a slight decrease in slag consumption per unit strand area (kg/m²) (1%).
9. Increase of stroke length and modification ratio increases slag consumption slightly.
10. While a consistent relationship is not found between frequency and slag consumption per unit area (kg/m²), a strong inverse trend is found with slag consumption per unit length per cycle (g/m·cycle), decreasing 35% with a ~62% increase in frequency.
11. Slag consumption (g/m·cycle) increases with increasing both PST and NST. The relation with PST is more clear.

REFERENCES

- [1] B. G. Thomas, M. S. Jenkins and R. B. Mahapatra, Investigation of Strand Surface Defects Using Mould Instrumentation and Modelling, *Ironmaking Steelmaking* 2004, vol. 31, pp. 485-494.
- [2] Brian G Thomas, Modeling of Continuous Casting Defects Related to Mold Fluid Flow, *Iron Steel Technol.* 2006, vol. 3, p. 127.
- [3] Kenneth C. Mills and Alistair B. Fox, The Role of Mould Fluxes in Continuous Casting-So Simple yet So Complex, *ISIJ Int.* 2003, vol. 43, pp. 1479-1486.
- [4] Mikio Suzuki, Hideaki Mizukami, Toru Kitagawa, Kiminari Kawakami, Shigetaka Uchida and Yoshimi Komatsu, Development of a New Mold Oscillation Mode for High-Speed Continuous Casting of Steel Slabs, *ISIJ Int.* 1991, vol. 31, pp. 254-261.
- [5] T. Nakano, K. Nagano, N. Masuo, M. Fuji and T. Matsuyama, Model Analysis of Melting Process of Mold Powder for Continuous Casting of Steel, *Nippon Steel Tech. Rep.* 1987, pp. 21-30.
- [6] T Tanaka and K Takatani, Hydrodynamics of Molten Powder in the Vicinity of Meniscus in Continuous Casting, *CAMP-ISIJ* 1989.
- [7] Hong Sha, Ralf Diedrichs and Klaus Schwerdtfeger, Dynamic Behavior of a Liquid/Liquid Interface at an Oscillating Wall, *Metall. Mater. Trans. B* 1996, vol. 27, pp. 305-314.
- [8] C. Perrot, J. N. Pontoire, C. Marchionni, M. -R. Ridolfi and L. F. Sancho, Several Slag Rims and Lubrication Behaviours in Slab Casting, *Metall. Res. Tech.* 2005, vol. 102, pp. 887-896.
- [9] R.B. Mahapatra, J.K. Brimacombe and I.V. Samarasekera, Mold Behavior and Its Influence on Quality in the Continuous Casting of Steel Slabs. ii. Mold Heat Transfer, Mold Flux

Behavior, Formation of Oscillation Marks, Longitudinal Off-Corner Depressions, and Subsurface Cracks, *Metall. Mater. Trans. B* 1991, vol. 22B, pp. 875-888.

[10] E. Takeuchi and J.K. Brimacombe, The Formation of Oscillation Marks in the Continuous Casting of Steel Slabs, *Metall. Mater. Trans. B* 1984, vol. 15B, pp. 493-509.

[11] K.C. Mills, A. Olusanya, R. Brooks, R. Morrell and S. Bagha, Physical Properties of Casting Powders. Iv. Physical Properties Relevant to Fluid and Thermal Flow, *Ironmaking Steelmaking* 1988, vol. 15, pp. 257-264.

[12] R.B. McDavid, Fluid Flow and Heat Transfer Behavior of Top-Surface Flux Layers in Steel Continuous Casting, Thesis, University of Illinois at Urbana-Champaign, 1990

[13] K. C. Mills, T. J. H. Billany, A. S. Normanton, B. Walker and P. Grieveson, Causes of Sticker Breakout During Continuous-Casting, *Ironmaking Steelmaking* 1991, vol. 18, pp. 253-265.

[14] T.J.H. Billany, A.S. Normanton, K.C. Mills and P. Grieveson, Surface Cracking in Continuously Cast Products, *Ironing and Steelmaking* 1991, vol. 18, pp. 403-410.

[15] S. Hiraki, K. Nakajima, T. Murakami and T. Kanazawa, Influence of Mold Heat Fluxes on Longitudinal Surface Cracks During High Speed Continuous Casting of Steel Slab, In *77th Steelmaking Conf.*, ed. ISS/AIME (ISS/AIME, Warrendale, PA: Chicago, IL, USA, 1994), pp. 397-403.

[16] J. Konishi, M. Militzer, J.K. Brimacombe and I.V. Samarasekera, Modeling the Formation of Longitudinal Facial Cracks During Continuous Casting of Hypoperitectic Steel, *Metall. Mater. Trans. B* 2002, vol. 33B, pp. 413-423B.

[17] L Hibbeler and Brian G Thomas, Investigation of Mold Flux Entrainment in Cc Molds Due to Shear Layer Instability, In *AISTech 2010 Steelmaking Conference Proc.*, (2010).

- [18] R. Bommaraju, R. Glennon and M. Frazee, Analysis of the Cause and Prevention of Longitudinal Midface Cracks and Depressions on Continuously Cast Free-Machining Steel Blooms, In *1st Eur. Conf. on Continuous Casting*, (Associazione Italiana di Metallurgia, Milano, Italy: Florence, Italy, 1991), pp. 1.599-1.610.
- [19] Ho-Jung Shin, S. H. Kim, B. G. Thomas, G. G. Lee, J. M. Park and J. Sengupta, Measurement and Prediction of Lubrication, Powder Consumption, and Oscillation Mark Profiles in Ultra-Low Carbon Steel Slabs, *ISIJ Int.* 2006, vol. 46, pp. 1635-1644.
- [20] H. Nakato, T. Sakuraya, T. Nozaki, T. Emi and H. Nishikawa, Physical and Chemical Properties of Casting Powders Affecting the Mold Lubrication During Continuous Casting, In *Steelmaking Proceedings*, (Washington, D.C., USA, 1986), pp. 137-143.
- [21] A. Delhalle, M. Larrecq, J.F. Marioton and P.V. Riboud, Slag Melting and Behaviour at Meniscus Level in a Cc Mold, In *Steelmaking Proceedings*, (Iron and Steel Society, Inc.: Washington, D.C., USA, 1986), pp. 145-152.
- [22] Z. Jander: *Anorg. Allg. Chem.* (1927), p. 163.
- [23] E. Anzai, T. Shigezumi, T. Nakano, T. Ando and M. Ikeda, Hydrodynamic Behavior of Molten Powder in Meniscus Zone of Continuous Casting Mold, *Nippon Steel Tech. Rep.* 1987, pp. 31-40.
- [24] K. Schwerdtfeger and H. Sha, Depth of Oscillation Marks Forming in Continuous Casting of Steel, *Metall. Mater. Trans. B* 2000, vol. 31B, pp. 813-826B.
- [25] K. Okazawa, T. Kajitani, W. Yamada and H. Yamamura, Infiltration Phenomena of Molten Powder in Continuous Casting Derived from Analysis Using Reynolds Equation Part 1: Steady Analysis, *ISIJ Int.* 2006, vol. 46, pp. 226-233.

- [26] K. Okazawa, T. Kajitani, W. Yamada and H. Yamamura, Infiltration Phenomena of Molten Powder in Continuous Casting Derived from Analysis Using Reynolds Equation Part 2: Unsteady Analysis, *ISIJ Int.* 2006, vol. 46, pp. 234-240.
- [27] A. Yamauchi, T. Emi and S. Seetharaman, A Mathematical Model for Prediction of Thickness of Mould Flux Film in Continuous Casting Mould, *ISIJ Int.* 2001, vol. 42, pp. 1084-1093.
- [28] G.J.W. Kor, An Analysis of the Fluid Flow of Liquid Mold Powder in the Space between the Cc Mold and the Steel Shell, In *Continuous Casting of Steel, 2nd Process Technology Conf.*, (ISS/AIME, Warrendale, PA: Chicago, IL., USA, 1981), pp. 124-132.
- [29] D.R. Bland, Flux and the Continuous Casting of Steel, *J. Inst. Math. Its Appl.* 1984, vol. 32, pp. 89-112.
- [30] N. Fowkes and A. Woods, The Flux of Flux in a Continuous Steel Caster, University of Western Australia 1989.
- [31] James M Hill, YongHong Wu and Benchawan Wiwatanapataphee, Analysis of Flux Flow and the Formation of Oscillation Marks in the Continuous Caster, *J. Eng. Math.* 1999, vol. 36, pp. 311-326.
- [32] J.R. King, A.A. Lacey, C.P. Please, P. Wilmott and A. Zoryk, The Formation of Oscillation Marks on Continuously Cast Steel, *Mathematical Engineering in Industry* 1993, vol. 4, pp. 91-106.
- [33] A.W. Cramb and F.J. Mannion, The Measurement of Meniscus Marks at Bethlehem Steel's Burns Harbor Slab Caster, In *Steelmaking Proceedings*, (Detroit, Michigan, USA, 1985), pp. 349-359.

- [34] H Steinruck and Christian Rudischer, Numerical Investigation of the Entrainment of Flux into the Lubrication Gap in Continuous Casting of Steel, In *Fifth World Congress on Computational Mechanics*, (2002).
- [35] Y. Meng and B.G. Thomas, Heat Transfer and Solidification Model of Continuous Slab Casting: Con1d, *Metall. Mater. Trans. B* 2003, vol. 34B, pp. 685-705.
- [36] J Sengupta, BG Thomas and MA Wells, The Use of Water Cooling During the Continuous Casting of Steel and Aluminum Alloys, *Metall. Mater. Trans. A* 2005, vol. 36, pp. 187-204.
- [37] Joydeep Sengupta, Manh-Kha Trinh, David Currey and Brian G Thomas, Utilization of Con1d at Arcelormittal Dofasco's No. 2 Continuous Caster for Crater End Determination, In *Proc. AISTech 2009 Steelmaking Conference Proc*, (2009), pp. 4-7.
- [38] Junya Iwasaki and Brian G Thomas, Thermal - Mechanical Model Calibration with Breakout Shell Measurements in Continuous Steel Slab Casting, *Supplemental Proceedings: Materials Properties, Characterization, and Modeling, Volume 2* 2012, pp. 355-362.
- [39] Begona Santillana, Lance C Hibbeler, Brian G Thomas, Arie Hamoen, Arnoud Kamperman and Willem Van der Knoop, Heat Transfer in Funnel-Mould Casting: Effect of Plate Thickness, *ISIJ Int.* 2008, vol. 48, pp. 1380-1388.
- [40] Y. Meng, C. Li, J. Parkman and B.G. Thomas, Simulation of Shrinkage and Stress in Solidifying Steel Shells of Different Grades, In *TMS annual Meeting 2004--Solidification Processes and Microstructures symposium*, (Charlotte, NC, 2004).
- [41] Y. Meng and B.G. Thomas, Simulation of Microstructure and Behavior of Interfacial Mold Slag Layers in Continuous Casting of Steel, *ISIJ Int.* 2006, vol. 46, pp. 660-669.

- [42] Bryan Petrus, Kai Zheng, X. Zhou, Brian G Thomas and Joseph Bentsman, Real-Time, Model-Based Spray-Cooling Control System for Steel Continuous Casting, *Metall. Mater. Trans. B* 2011, vol. 42, pp. 87-103.
- [43] Lance C Hibbeler, Brian G Thomas, Ronald C Schimmel and Gert Abbel, The Thermal Distortion of a Funnel Mold, *Metall. Mater. Trans. B* 2012, vol. 43, pp. 1156-1172.
- [44] Ya Meng and Brian G Thomas, Heat-Transfer and Solidification Model of Continuous Slab Casting: Con1d, *Metall. Mater. Trans. B* 2003, vol. 34, pp. 685-705.
- [45] B.G. Thomas and Y. Meng: *Con1d Users Manual*. (University of Illinois, 2002).
- [46] S. Ogibayashi, T. Mukai and Y. Mimura, Mold Powder Technology for Continuous Casting of Low-Carbon Aluminium-Killed Steel, *Nippon Steel Tech. Rep.* 1987, pp. 1-10.
- [47] K Tsutsumi, H Murakami, SI Nishioka, M Tada, M Nakada and M Komatsu, Estimation of Mold Powder Consumption in Continuous Casting, *Trans. Iron Steel Inst. Jpn.* 1998, vol. 84, pp. 617-624.
- [48] Mikio Suzuki, Makoto Suzuki and Masayuki Nakada, Perspectives of Research on High-Speed Conventional Slabcontinuous Casting of Carbon Steels, *ISIJ Int.* 2001, vol. 41, pp. 670-682.
- [49] M. Kawamoto, T. Murakami, M. Hanao, H. Kikuchi and T. Watanabe, Mould Powder Consumption of Continuous Casting Operations, *Ironmaking Steelmaking* 2002, vol. 29, pp. 199-202.
- [50] M.M. Wolf, Mold Oscillation Guidelines, In *1991 Steelmaking Conference*, (Washington, D.C., USA, 1991), pp. 51-71.

- [51] M. Bobadilla, J. M. Jolivet, J. Y. Lamant and M. Larrecq, Continuous Casting of Steel: A Close Connection between Solidification Studies and Industrial Process Development, *Mater. Sci. Eng., Proc. Conf.* 1993, vol. 173, pp. 275-285.
- [52] T Darle, A Mouchette, M Roscini, M Nadif and D Salvadori, Hydraulic Oscillation of the Cc Slab Mold at Sollac Florange: First Industrial Results, Future Developments, In *76 th Steelmaking Conf.*, (1993), pp. 209-218.
- [53] O.D. Kwon, J. Choi, I.R. Lee, J.W. Kim, K.H. Moon and Y.K. Shin, Optimization of Mold Oscillation Pattern for the Improvement of Surface Quality and Lubrication in Slab Continuous Casting, In *Steelmaking Conference Proceedings*, (Washington, D.C., USA, 1991), pp. 561-568.
- [54] R. M. McDavid and B. G. Thomas, Flow and Thermal Behavior of the Top Surface Flux/Powder Layers in Continuous Casting Molds, *Metallurgical and Materials Transactions B-Process Metallurgy and Materials Processing Science* 1996, vol. 27, pp. 672-685.
- [55] B Zhao, SP Vanka and BG Thomas, Numerical Study of Flow and Heat Transfer in a Molten Flux Layer, *Int. J. Heat Fluid Flow* 2005, vol. 26, pp. 105-118.
- [56] R. Chaudhary, B. G. Thomas and S. P. Vanka, Effect of Electromagnetic Ruler Braking (Embr) on Transient Turbulent Flow in Continuous Slab Casting Using Large Eddy Simulations, *Metall. Mater. Trans. B* 2012, vol. 43, pp. 532-553.
- [57] R. Liu, B. G. Thomas and J. Sengupta, Simulation of Transient Fluid Flow in Mold Region During Steel Continuous Casting, *IOP Conf. Ser.: Mater. Sci. Eng.* 2012, vol. 33, p. 012015.
- [58] Claudio Ojeda, Joydeep Sengupta, Brian G. Thomas, Jon Barco and Jose Luis Arana, Mathematical Modeling of Thermal-Fluid Flow in the Meniscus Region During an Oscillation

Cycle, In *AISTech 2006 - Iron and Steel Technology Conference, May 1 - 4 2006*, (Association for Iron and Steel Technology, AISTECH: Cleveland, OH, United states, 2006), pp. 1017-1028.

[59] Claudio Ojeda, Brian G. Thomas, Jon Barco and Jose Luis Arana, Model of Thermal-Fluid Flow in the Meniscus Region During an Oscillation Cycle, In *AISTech 2007 - Iron and Steel Technology Conference, May 7 - 10 2007*, (Association for Iron and Steel Technology, AISTECH: Indianapolis, IN, United states, 2007), pp. 269-283.

[60] Joydeep Sengupta, BrianG Thomas, Ho-Jung Shin, Go-Gi Lee and Seon-Hyo Kim, A New Mechanism of Hook Formation During Continuous Casting of Ultra-Low-Carbon Steel Slabs, *Metall. Mater. Trans. A* 2006, vol. 37, pp. 1597-1611.

[61] Pavel E. Ramirez Lopez, Kenneth C. Mills, Peter D. Lee and Begona Santillana, A Unified Mechanism for the Formation of Oscillation Marks, *Metall. Mater. Trans. B* 2012, vol. 43, pp. 109-122.

[62] Pavel E. Ramirez-Lopez, Peter D. Lee and Kenneth C. Mills, Explicit Modelling of Slag Infiltration and Shell Formation During Mould Oscillation in Continuous Casting, *ISIJ Int.* 2010, vol. 50, pp. 425-434.

[63] C. W. Hirt and B. D. Nichols, Volume of Fluid (Vof) Method for the Dynamics of Free Boundaries, *J. Comput. Phys.* 1981, vol. 39, pp. 201-225.

[64] V. R. Voller and C. Prakash, A Fixed Grid Numerical Modelling Methodology for Convection-Diffusion Mushy Region Phase-Change Problems, *Int. J. Heat Mass Transfer* 1987, vol. 30, pp. 1709-1719.

[65] A Badri, TT Natarajan, CC Snyder, KD Powers, FJ Mannion, M Byrne and AW Cramb, A Mold Simulator for Continuous Casting of Steel: Part II. The Formation of Oscillation Marks

During the Continuous Casting of Low Carbon Steel, *Metall. Mater. Trans. B* 2005, vol. 36, pp. 373-383.

[66] A Badri, TT Natarajan, CC Snyder, KD Powers, FJ Mannion and AW Cramb, A Mold Simulator for the Continuous Casting of Steel: Part I. The Development of a Simulator, *Metall. Mater. Trans. B* 2005, vol. 36, pp. 355-371.

[67] Ho-Jung Shin, Seon-Hyo Kim, Brian G. Thomas, Go-Gi Lee, Je-Min Park and Joydeep Sengupta, Measurement and Prediction of Lubrication, Powder Consumption, and Oscillation Mark Profiles in Ultra-Low Carbon Steel Slabs, *ISIJ Int.* 2006, vol. 46, pp. 1635-1644.

[68] J. U. Brackbill, D. B. Kothe and C. Zemach, A Continuum Method for Modeling Surface-Tension, *J. Comput. Phys.* 1992, vol. 100, pp. 335-354.

[69] M. Ishii: *Thermo-Fluid Dynamic Theory of Two-Phase Flow*. (Eyrolles, 1975).

[70] F. R. Menter, 2-Equation Eddy-Viscosity Turbulence Models for Engineering Applications, *AIAA J.* 1994, vol. 32, pp. 1598-1605.

[71] FR Menter, M Kuntz and R Langtry, Ten Years of Industrial Experience with the Sst Turbulence Model, *Turbulence, heat and mass transfer* 2003, vol. 4, pp. 625-632.

[72] (ANSYS, Inc.: Canonsburg, PA, 2013).

[73] Y.M. Won and B.G. Thomas, Simple Model of Microsegregation During Solidification of Steels, *Metall. Mater. Trans. A* 2001, vol. 32A, pp. 1755-1767.

[74] C.A. Sleicher and M.W. Rouse, A Convenient Correlation for Heat Transfer to Constant and Variable Property Fluids in Turbulent Pipe Flow, *Int. J. Heat Mass Transfer* 1975, vol. 18, pp. 677-683.

- [75] Y. Meng, B.G. Thomas, A. A. Polycarpou, A. Prasad and H. Henein, Mold Slag Property Measurements to Characterize Continuous-Casting Mold-Shell Gap Phenomena, *Can. Metall. Q.* 2006, vol. 45, pp. 79-94.
- [76] Ho-Jung Shin, Thesis, Pohang University of Science and Technology, 2006
- [77] PV Riboud, Y Roux, LD Lucas and H Gaye, Improvement of Continuous Casting Powders, *Fachberichte Huttenpraxis Metallweiterverarbeitung* 1981, vol. 19, pp. 859-869.
- [78] K. Koyama, Y. Nagano, K. Nagano and T. Nakano, Design for Chemical and Physical Properties of Continuous Casting Powders, *Nippon Steel Tech. Rep.* 1987, vol. 34, pp. 41-47.
- [79] Takamichi Iida, Hidenori Sakai, Yoshifumi Kita and Katsuhiko Murakami, Equation for Estimating Viscosities of Industrial Mold Fluxes, *High Temp. Mater. Processes (Berlin, Ger.)* 2000, vol. 19, pp. 153-164.
- [80] K.C. Mills and S. Sridhar, Viscosities of Ironmaking and Steelmaking Slags, *Ironmaking Steelmaking* 1999, vol. 26, pp. 262-268.
- [81] M.D. Lanyi and C.J. Rosa, Viscosity of Casting Fluxes Used During Continuous Casting of Steel, *Metall. Mater. Trans. B* 1981, vol. 12B, pp. 287-298.
- [82] D. Larson, Criteria for Selecting Mold Powders to Optimize Continuous Cast Steel Quality, *Ind. Heat.* 1986, vol. 53, pp. 16-17.
- [83] K. Rietema, In *The Dynamics of Fine Powders*, (Elsevier: 1991).
- [84] R. Taylor and K.C. Mills, Physical Properties of Casting Powders Iii: Thermal Conductivities of Casting Powders, *Ironmaking Steelmaking* 1988, vol. 15, pp. 187-194.
- [85] J. K. Mackenzie and R. Shuttleworth, A Phenomenological Theory of Sintering, *Proc. Phys. Soc., London, Sect. B* 1949, vol. 62, p. 833.

- [86] Robert Eriksson and Seshadri Seetharaman, Thermal Diffusivity Measurements of Some Synthetic CaO-Al₂O₃-SiO₂ Slags, *Metall. Mater. Trans. B* 2004, vol. 35, pp. 461-469.
- [87] Hiroki Hasegawa, Hiromichi Ohta, Hiroyuki Shibata and Yoshio Waseda, Recent Development in the Investigation on Thermal Conductivity of Silicate Melts, 2012.
- [88] M. Kishimoto, M. Maeda and Y. Kawai, Thermal Conductivity and Specific Heat of Metallurgical Slags, *JOURNAL OF METALS*. 1984, vol. 36, pp. 93-93.
- [89] AW Cramb and I Jimbo, Interfacial Considerations in Continuous Casting, *Iron Steelmaker* 1989, vol. 16, pp. 43-55.
- [90] Joonho Lee and Kazuki Morita, Evaluation of Surface Tension and Adsorption for Liquid Fe-S Alloys, *ISIJ Int.* 2002, vol. 42, pp. 588-594.
- [91] B. J. Keene, Review of Data for the Surface-Tension of Pure Metals, *Int. Mater. Rev.* 1993, vol. 38, pp. 157-192.
- [92] A. Kasama, A. McLean, W. A. Miller, Z. Morita and M. J. Ward, Surface-Tension of Liquid-Iron and Iron Oxygen Alloys, *Can. Metall. Q.* 1983, vol. 22, pp. 9-17.
- [93] K. C. Mills and Y. C. Su, Review of Surface Tension Data for Metallic Elements and Alloys: Part 1 - Pure Metals, *Int. Mater. Rev.* 2006, vol. 51, pp. 329-351.
- [94] Thomas Young, An Essay on the Cohesion of Fluids, *Philos. Trans. R. Soc. London* 1805, vol. 95, pp. 65-87.
- [95] H Nakato and I Muchi, Mathematical Modeling of the Temperature Field in the Continuous Casting Mold Region Taking into Account the Properties of the Casting Powders, *Tetsu-to-Hagane(Journal of the Iron and Steel Institute of Japan)* 1980, vol. 66, pp. 33-42.
- [96] J.J. Bikerman: *Physical Surfaces*. (Elsevier Science, 2012), pp. 11-12.

- [97] Adam Badri, Initial Solidification Phenomena in Continuous Casting, Thesis, Carnegie Mellon University, 2003
- [98] K. Tsutsumi, H. Murakami, S.I. Nishioka, M. Tada, M. Nakada and M. Komatsu, Estimation of Mold Powder Consumption in Continuous Casting, *Trans. Iron Steel Inst. Jpn.* 1998, vol. 84, pp. 617-624.
- [99] N. Ozisik: *Inverse Heat Transfer: Fundamentals and Applications*. (Taylor & Francis, 2000).
- [100] J.V. Beck, B. Blackwell and C.R.S. Clair: *Inverse Heat Conduction: Ill-Posed Problems*. (Wiley, 1985).
- [101] BG Thomas, D Lui and B Ho, Effect of Transverse Depressions and Oscillation Marks on Heat Transfer in the Continuous Casting Mold, 1997.
- [102] B. G. Thomas, M. A. Wells and D. Li, In *Sensors, Sampling, and Simulation for Process Control*, (John Wiley & Sons, Inc.: 2011), pp. 119-126.
- [103] R.J. O'Malley and J. Neal, An Examination of Mold Flux Film Structures and Mold Gap Behavior Using Mold Thermal Monitoring and Petrographic Analysis at Armco's Mansfield Operations, In *Proc. METEC Congress 99*, (Verein Deutscher Eisenhüttenleute, Dusseldorf, Germany: Dusseldorf, Germany, 1999).
- [104] M. Kawamoto, T. Murakami, M. Hanao, H. Kikuchi and T. Watanabe, Mould Powder Consumption of Continuous Casting Operations, *Ironmaking & Steelmaking* 2002, vol. 29, pp. 199-202.
- [105] Maeda H and Hirose T, In *CAMP-ISIJ*, (1993), p. 280.
- [106] Wolf M., In *Conference on Continuous Casting of Steel in the Developing Countries*, (Beijing, China, 1993), pp. 66-76.

- [107] Rajil Saraswat, AB Fox, KC Mills, PD Lee and B Deo, The Factors Affecting Powder Consumption of Mould Fluxes, *Scand. J. Metall.* 2004, vol. 33, pp. 85-91.
- [108] H. Mizukami, K. Kawakami and T. Kitagawa, Lubrication Phenomena in a Mold and Optimum Mold Oscillation Mode in High-Speed Casting, *Trans. Iron Steel Inst. Jpn.* 1986, vol. 72, pp. 1862-1869.
- [109] Kiminari Kawakami, Toru Kitagawa, Hideaki Mizukami, Hideo Uchibori, Shinobu Miyahara, Mikio Suzuki and Yusuke Shiratani, Fundamental Study and Its Application of Surface Defects of Powder Cast Strands, *Tetsu-to-Hagane* 1981, vol. 67, pp. 1190-1199.
- [110] H Shin, G Lee, W Choi, S Kang, S Kim, J Park and Brian G Thomas, Effect of Mold Oscillation on Powder Consumption and Hook Formation in Ultra Low Carbon Steel Slabs, In *AISTECH-Conference Proceedings*, (Association for Iron & Steel Technology: 2004), p. 1157.
- [111] K. Hamagami, K. Sorimachi, M. Kuga, T. Koshikawa and M. Saigusa, Studies on Quality Improvement in Strand Cast Slabs at Chiba Works, In *Steelmaking Conference*, (1982), pp. 358-364.
- [112] V. R. Voller and C. R. Swaminathan, Eral Source-Based Method for Solidification Phase Change, *Numerical Heat Transfer, Part B: Fundamentals* 1991, vol. 19, pp. 175-189.

APPENDIX A

Table A.1: Input data for Shin and Badri Case for CON1D.

Parameters	Shin Case	Badri Case	Unit
Carbon Content, C	0.003	0.0046	%
Liquidus Temperature, T_{liq}	1533.82	1531.87	°C
Solidus Temperature, T_{sol}	1518.15	1518.7	°C
Fraction Solid for Shell Thickness Location, f_s	0.5	0.3	
Mold Thickness at Top (Including water channel)	40	22.23	mm
Total Mold Length, Z_{mold_total}	900	451	mm
Total Mold Width	1300	100	mm
Initial Cooling Water Temperature, T_{water}	50	38	°C
Water Channel Geometry,			mm
Depth, d_{ch}	20	13.7	
Width, w_{ch}	5	7.9	
Spacing between channels, l_{ch}	19	15.8	
Total Channel Cross Section Area, W/N	7290/900	647.21	mm ²
Cooling Water Velocity, V_{water}	-10.22	-8	m/s
Mold Conductivity, k_{mold}	350	340	W/m·K
Mold Emissivity, ϵ_{mold}	0.5	0.5	°C
Mold Powder Solidification Temperature, T_{fsol}	1101	1101	°C
Mold Powder Conductivity, k_{solid}/k_{liquid}	1.5/1.5	1/0.85	W/m·K
Air Conductivity, k_{air}	0.06	0.06	W/m·K
Slag Layer/Mold Resistance, $r_{contact}$	5.00E-09	5.00E-09	m ² ·K/W
Mold Powder Viscosity at 1300°C, μ_{1300}	5.5	5.5	Poise
Exponent for Temperature dependent Viscosity, n	1.8	1.8	
Slag Density, ρ_{slag}	2600	2600	kg/m ³
Slag Absorption Factor, a	250	250	
Slag Emissivity, ϵ_{slag}	0.9	0.9	
Mold Powder Consumption Rate, Q_{slag}	0.236	1.23	kg/m ²
Empirical solid slag layer speed factor, f_v	0	0.005	
Casting Speed, v_c	0.0232	0.0127	m/s
Pour Temperature, T_{pour}	1565	1532	°C
Slab Geometry, W×N	1300×230	400×100	mm
Nozzle Submergence Depth, d_{nozzle}	161	100	mm
Oscillation Mark Geometry, $d_{mark} \times w_{mark}$	0.25×3	0.81×8.73	mm
Mold Oscillation Frequency, f	2.9	1.3	Hz
Oscillation Stroke, stroke	5.89	6.3	mm
Coating layer, Ni	1-1.4	0.05	mm

Coating layer, Cr	0.1	--	mm
Scale	--	0.02	mm
Air gap	--	0.10-0.21	mm

Table A.2: Steel composition.

1. Shin Case
C(0.003%)-Mn(0.08%)-S(.01%)-P(.015%)-Si(0.005%)-Cr(.01%)-Ni(0.01%)-Cu(0.01%)-Ti(0.05%)-Al(0.04%)
2. Badri Case
C(0.0046%)-Mn(0.46%)-S(.0089%)-P(.011%)-Si(0.01%)-Cr(.035%)-Ni(.015%)-Cu(0.027%)-Ti(0.015%)-Al(0.051%)-N(0.0057%)-Mo(0.004%)-V(0.003%)-Nb(0.0002%)

APPENDIX B

The non-sinusoidal form mold oscillation equation is presented in Section 3.3. Figure B.1(a-b) shows the displacement and velocity curve for a typical casting condition ($f = 2.58$ Hz, $\alpha_m = 0.24$ and $s = 6.37$ mm) from time = 0 to 1.16 s respectively along with sinusoidal form of the equation ($\alpha_m = 0$).

For the current model, the interfacial air gap and slag gap thickness is reported in Figure B.2 and B.3 for Shin and Badri Case respectively. In Shin case (Figure B.2), air gap is not present.

Figure B.4 was constructed using Figure 269 and 273 from Badri Thesis.^[97] This shows that although heat flux increases during NST the temperature does not start to increase with a small time lag, rather it decreases during this time period. Based on the discussion in Section 4.7, a left shift in the temperature curves is expected to match the calculated heat flux curves.

Figure B.5 shows a simplified domain used to study the effect of increasing the temperature of the shell cold face. Here, temperature is increased from 1440 °C to 1521 °C and corresponding vertical velocity profile across the 6 mm gap is reported in Figure 12(b). Higher boundary temperature causes the viscosity to be lower and consequently higher mass flow.

Figure B.6 reports the heat fluxes in the intermediate step of finding approximate heat flux profile for the measured temperature by Badri.^[97] Case A uses the heat flux model where linearly varying heat flux profile is prescribed in CON1D on the mold face. Case B uses the “interface model” where the heat flux is determined by specifying slag properties. Figure B.7 shows the air gap profile used in Case B.

The mold thermocouple temperature predictions from Case B are represented in Figure B.8 considering the movement of the thermocouple bead inside the hole (1.4 mm diameter) and very close match was found with TC3-6. In TC1-2 the temperature is comparatively lower because the interface model in CON1D assumes that the heat flux is zero above meniscus.

Figure B.9 compares the predicted shell thickness and measured shell thickness which has been used as a validation for CON1D simulation. The measured shell thickness is expected to be higher because when the shell is taken out for taking measurements, an extra layer of liquid steel solidifies over the original shell thickness and makes it thicker. So, the actual thickness is expected to be lower than what was reported by Badri^[97] as seen in Figure B.9.

Temperature and heat flux predictions in 9 simulated oscillation cycles from starting for TC3 and TC4 are shown in Figure B.10-11 and Figure B.12-13 respectively for Shin case. TC4 shows the effect of steel overflow and different behavior has been predicted specially at later oscillation cycles because the overflowed steel drop is drawn back by the mold oscillation which does not happen in reality. Since the solidification of the steel overflow has not been considered in the model this unphysical movement of the steel drop causes unexpected variation in later cycles.

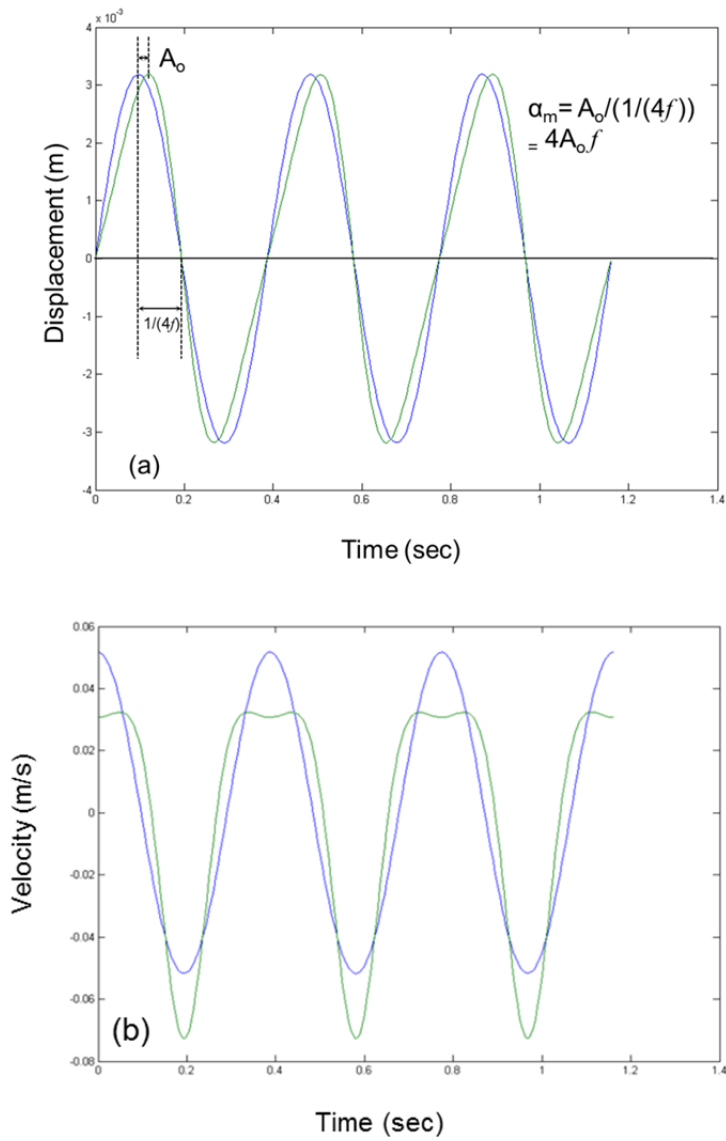


Figure B.1: Typical Sinusoidal and Non-sinusoidal Oscillation
 (a) Displacement Curve (b) Velocity Curve.

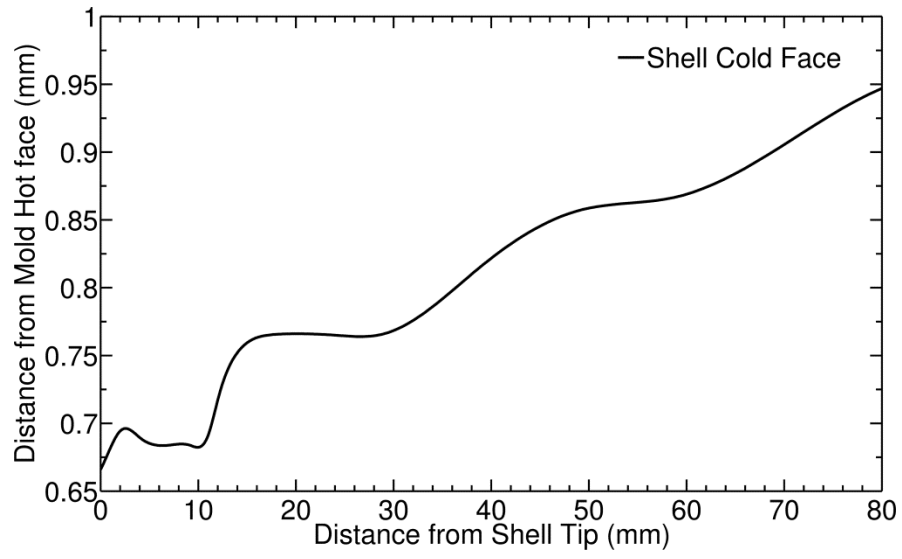


Figure B.2: Shin Case gap Profile in current model.

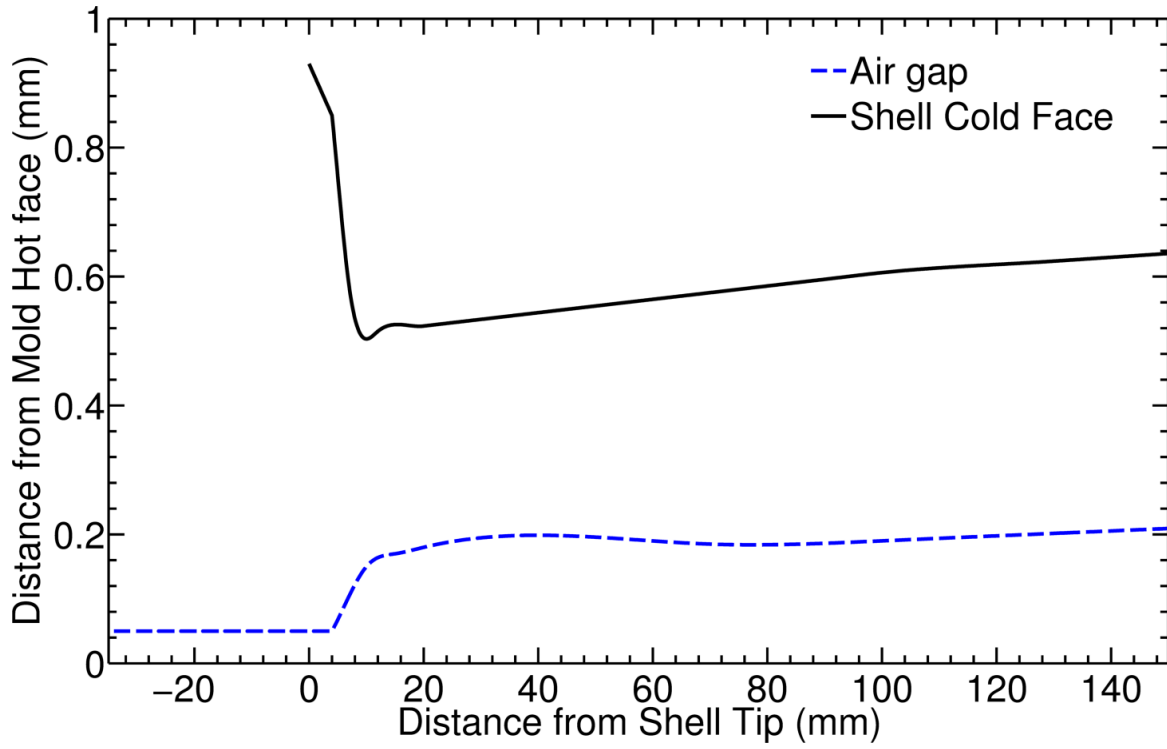


Figure B.3: Badri case gap Profile in current model.

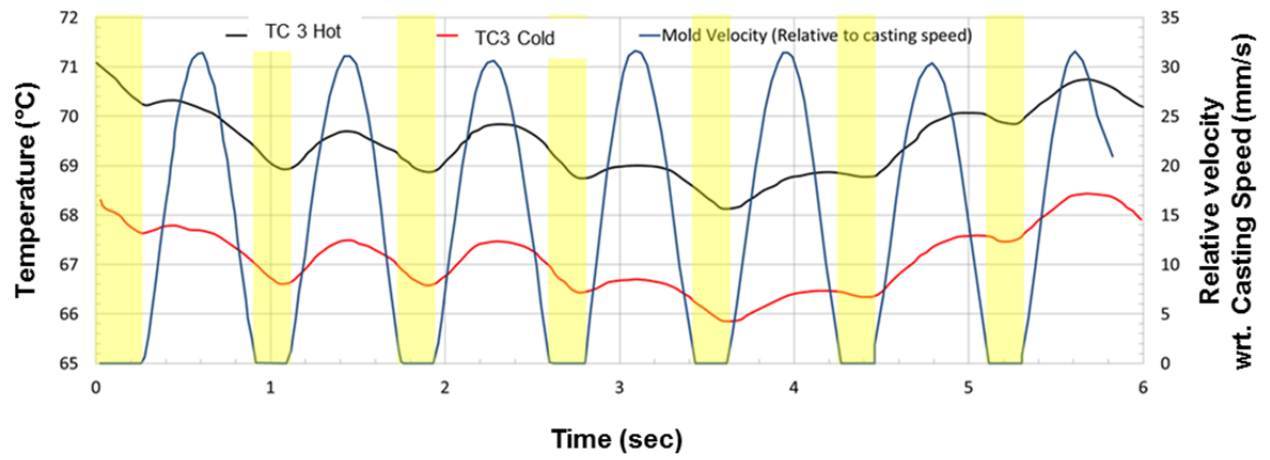


Figure B.4: Badri^[97] measured temperatures for TC3 Hot and Cold.

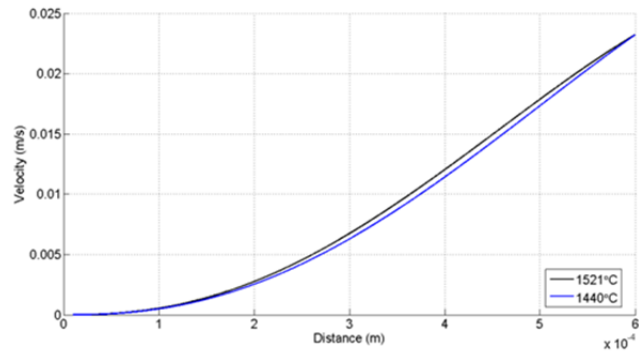
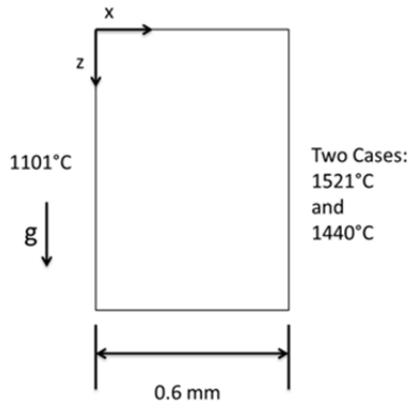


Figure B.5: Effect of increasing temperature on boundary;
 (a) Domain, (b) Vertical velocity profile across the gap.

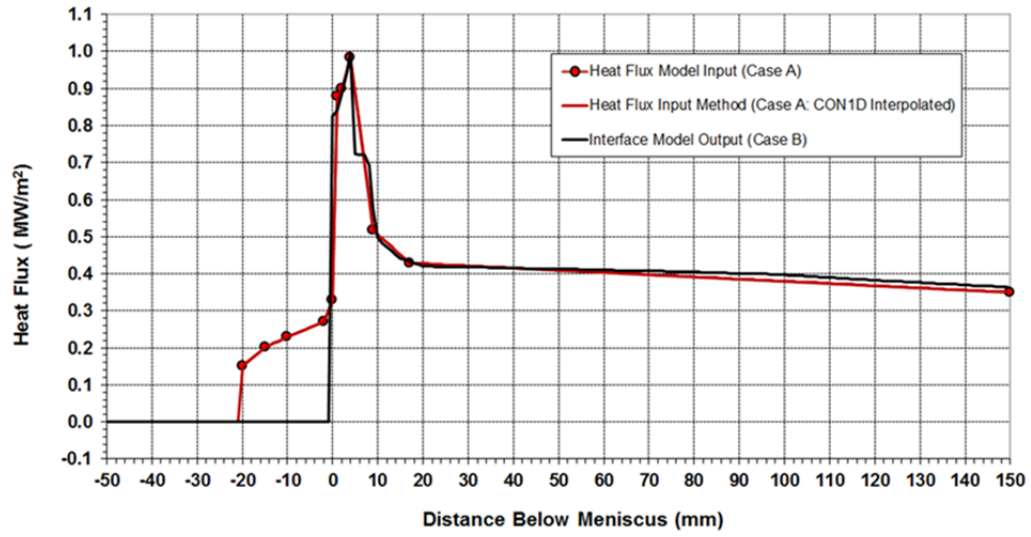


Figure B.6: Heat Flux in CON1D for Badri Case simulations.

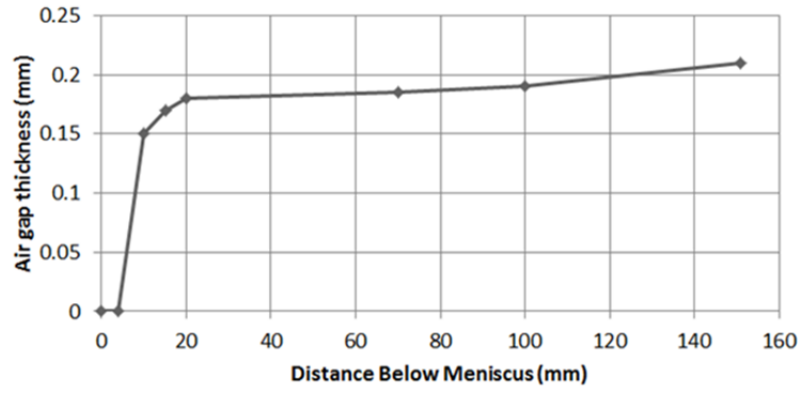


Figure B.7: Air gap thickness for CON1D model (Badri) - Case B.

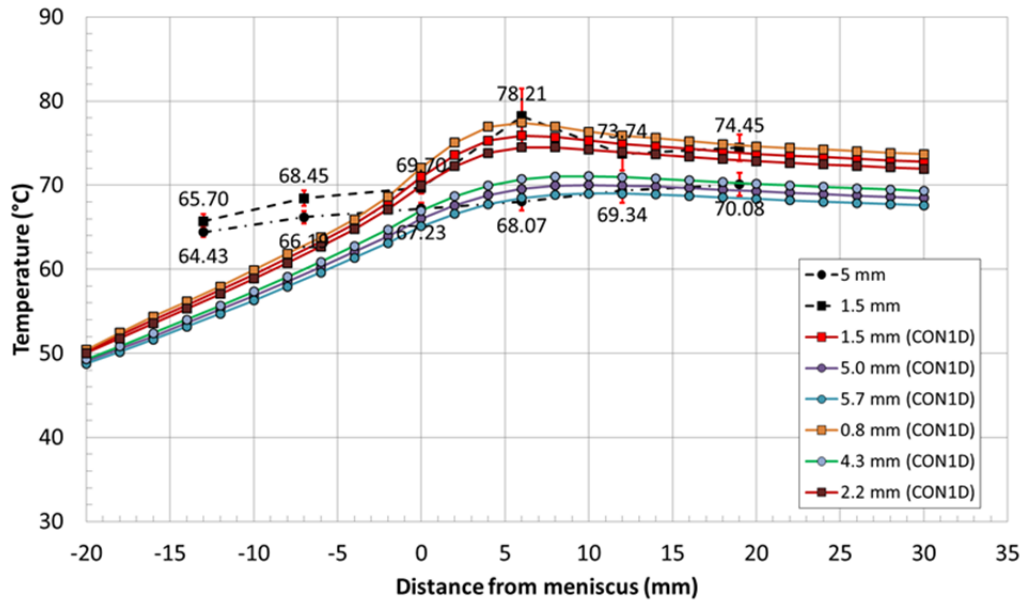


Figure B.8: Thermocouple prediction by CON1D vs averaged measured values by Badri.

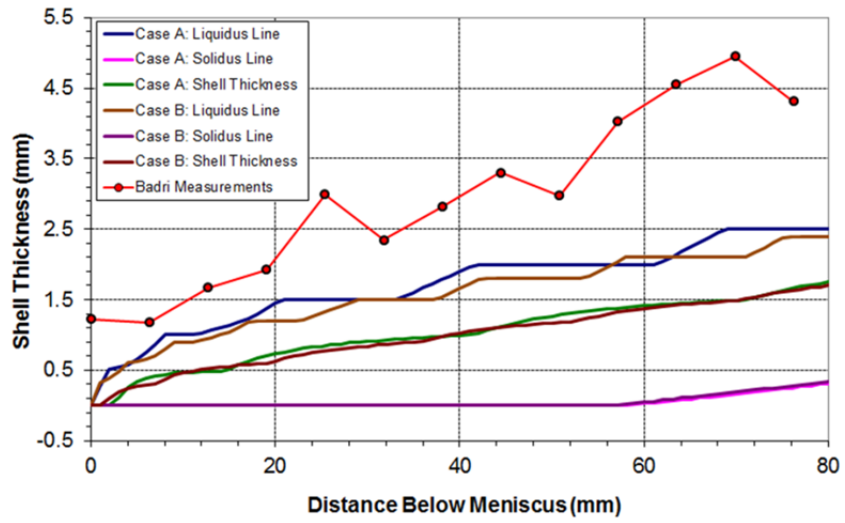


Figure B.9: Shell thickness prediction by CON1D Vs. measured values by Badri.^[97]

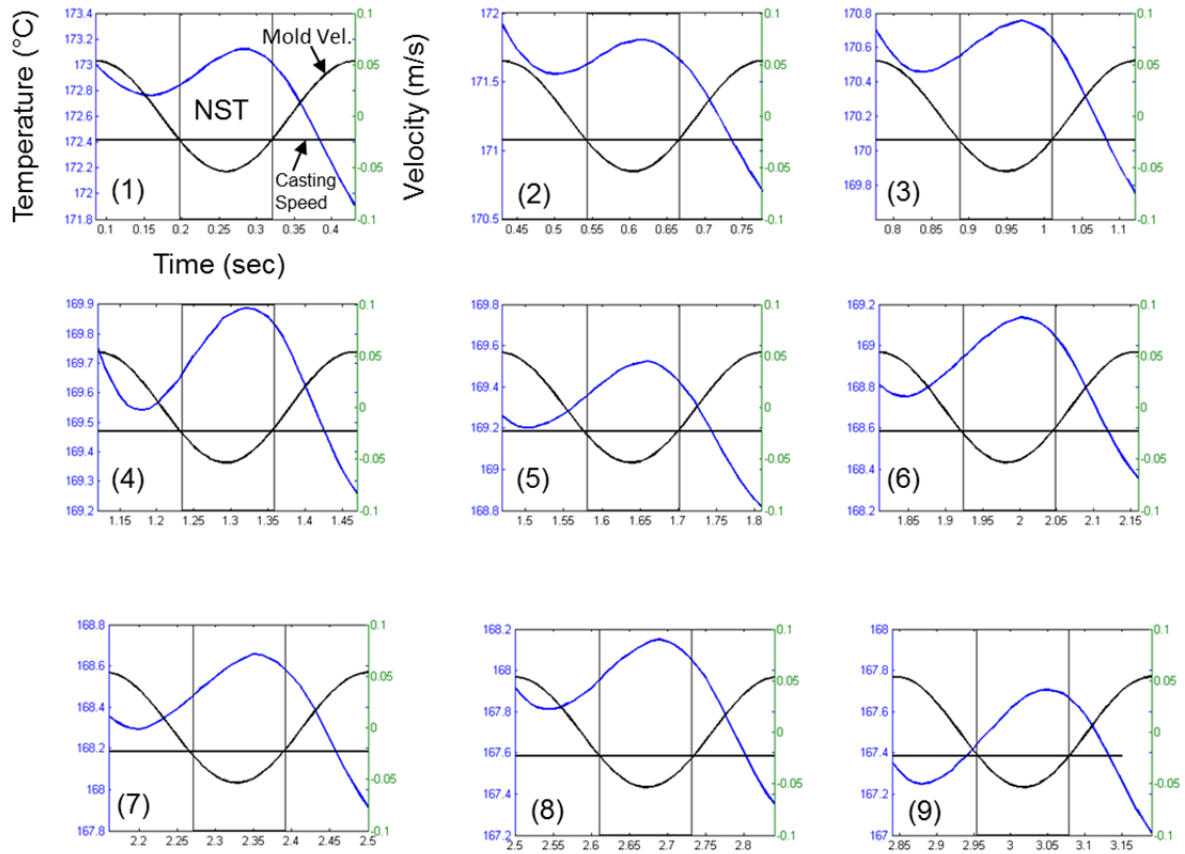


Figure B.10: Temperature predictions over 9 oscillation cycles for TC 3 (Shin Case).

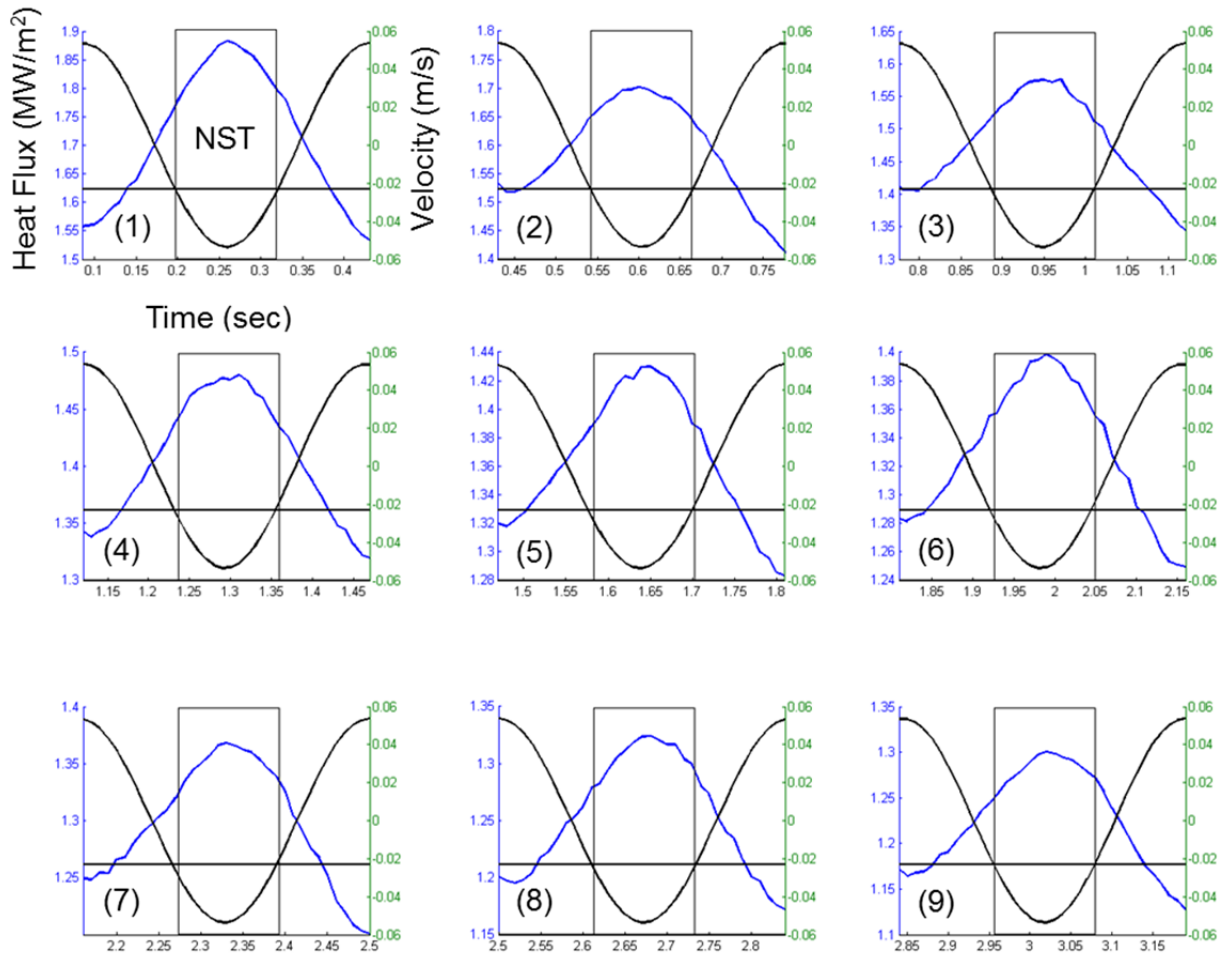


Figure B.11: Surface heat flux predictions over 9 oscillation cycles for TC 3 (Shin Case).

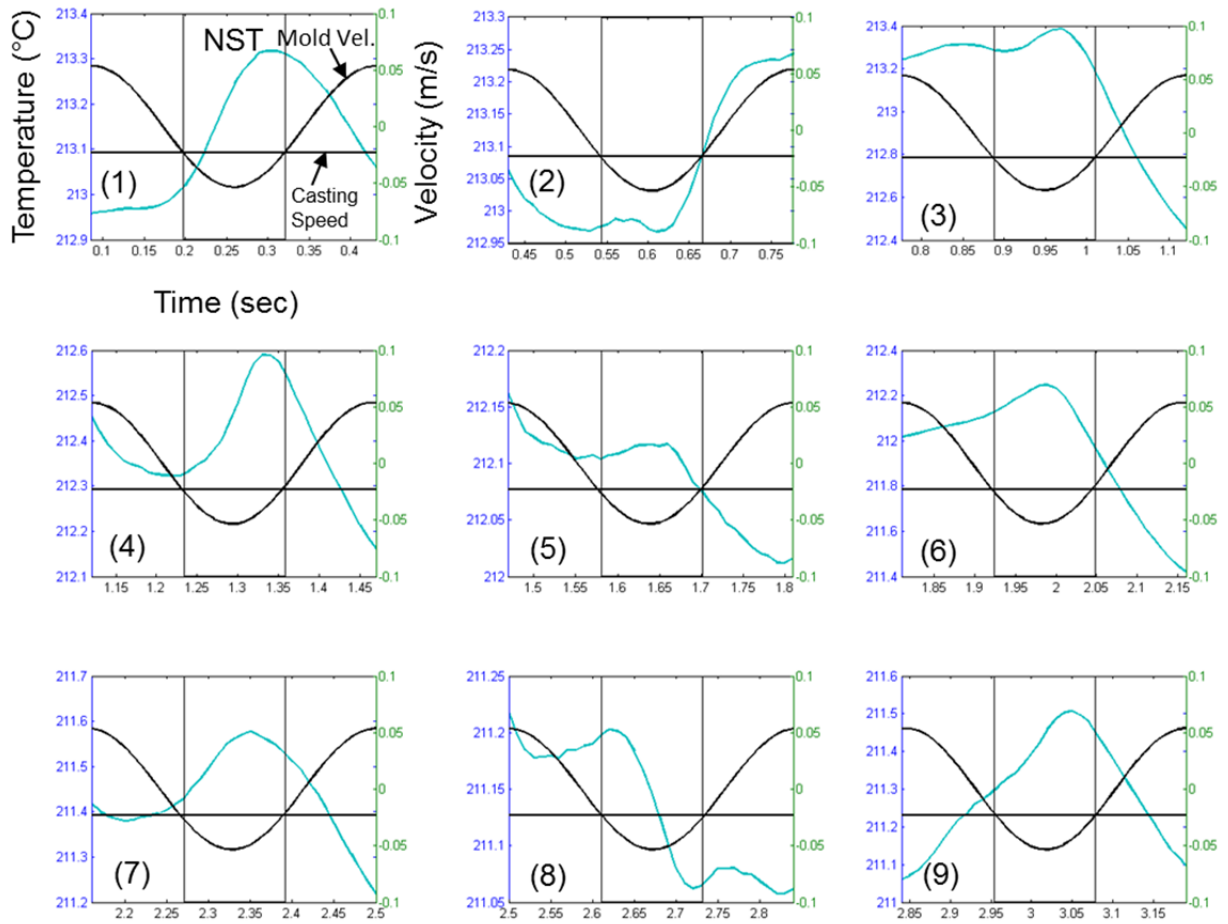


Figure B.12: Temperature predictions over 9 oscillation cycles for TC 4 (Shin Case).

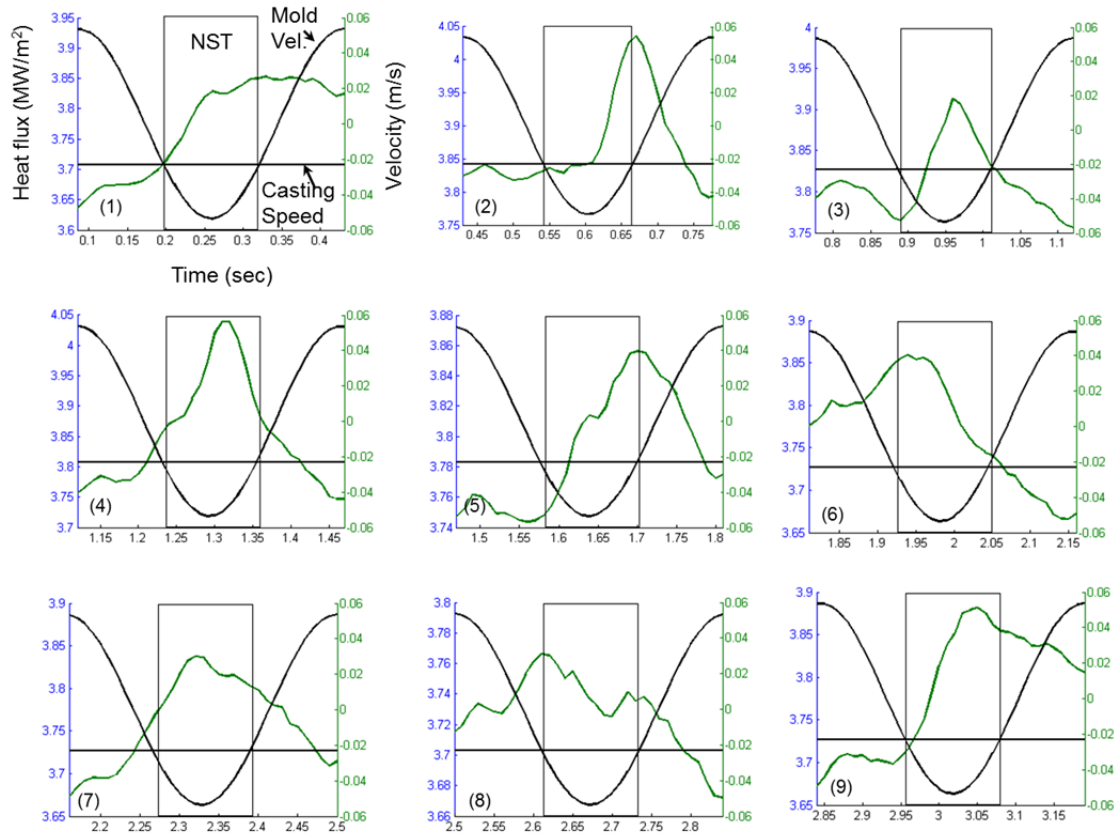


Figure B.13: Surface heat flux predictions over 9 oscillation cycles for TC 4 (Shin Case).

APPENDIX C

C.1 Calculation of Total Slag Consumption in Badri Case:

Figure C.1(a-b) shows the surface profile of ultra-low carbon steel measured by Badri^[66] and the measurements are taken from this figure assuming triangular shaped oscillation marks. Average values of OM width (w_{mark}), depth (d_{mark}) and pitch (L_{pitch}) are measured to be 8.73, 0.81 and 9.77 mm respectively. OM consumption per unit area is calculated based on the following equation to be 0.905 kg/m².

$$Q_{OM} = \frac{1}{2} \frac{\rho_{sl} d_{mark} w_{mark}}{L_{pitch}}$$

Here, the distance from root of one OM to another OM, $L_{pitch} = v_c/f$.

The lubrication consumption was based on Shin's equation^[19] given by –

$$Q_{lub} = 0.507 e^{3.59t_p} \frac{f}{v_c}$$

Which gives 0.325 kg/m², giving a total of 1.23 kg/m² slag consumption for the Badri case.

C.2 Different Measures of Slag Consumption:

Three different units to express slag consumption have been investigated in this work. The slag consumption rate, mass per unit perimeter per unit time, calculated by the 2-D computational model as Q_l (g/m·s) can be converted to consumption per unit strand area, Q_{area} (kg/m²) using the following equation-

$$Q_{area} = Q_l \times \frac{1}{v_c} \times \frac{1}{1000}$$

Where, v_c is casting speed in m/s.

Finally, slag consumption per meter per cycle, Q_c (g/m·cycle) can be calculated from slag consumption per unit strand area using the equation-

$$Q_c = Q_{area} \times \frac{v_c}{f} \times 1000$$

where, v_c is casting speed in m/s, f is frequency in cycle per second.

C.3 Figures:

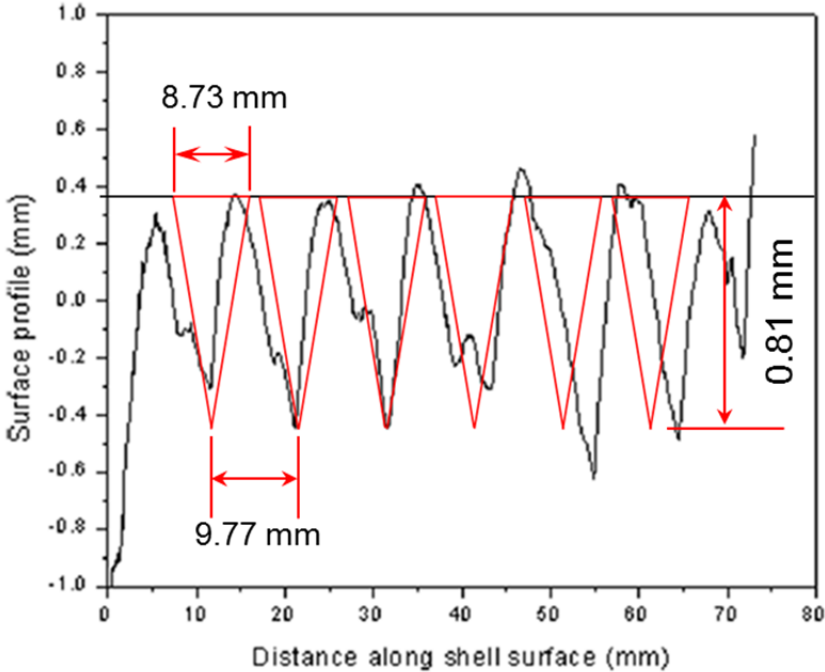


Figure C.1: Surface profile for Ultra low carbon steel measure by Badri.^[66]